# AERODYNAMICS OF A ROTATING WHEEL IN A WHEELHOUSE

## A Numerical Investigation using LES

Veeraraghavan Viswanathan

Technische Universiteit Delft

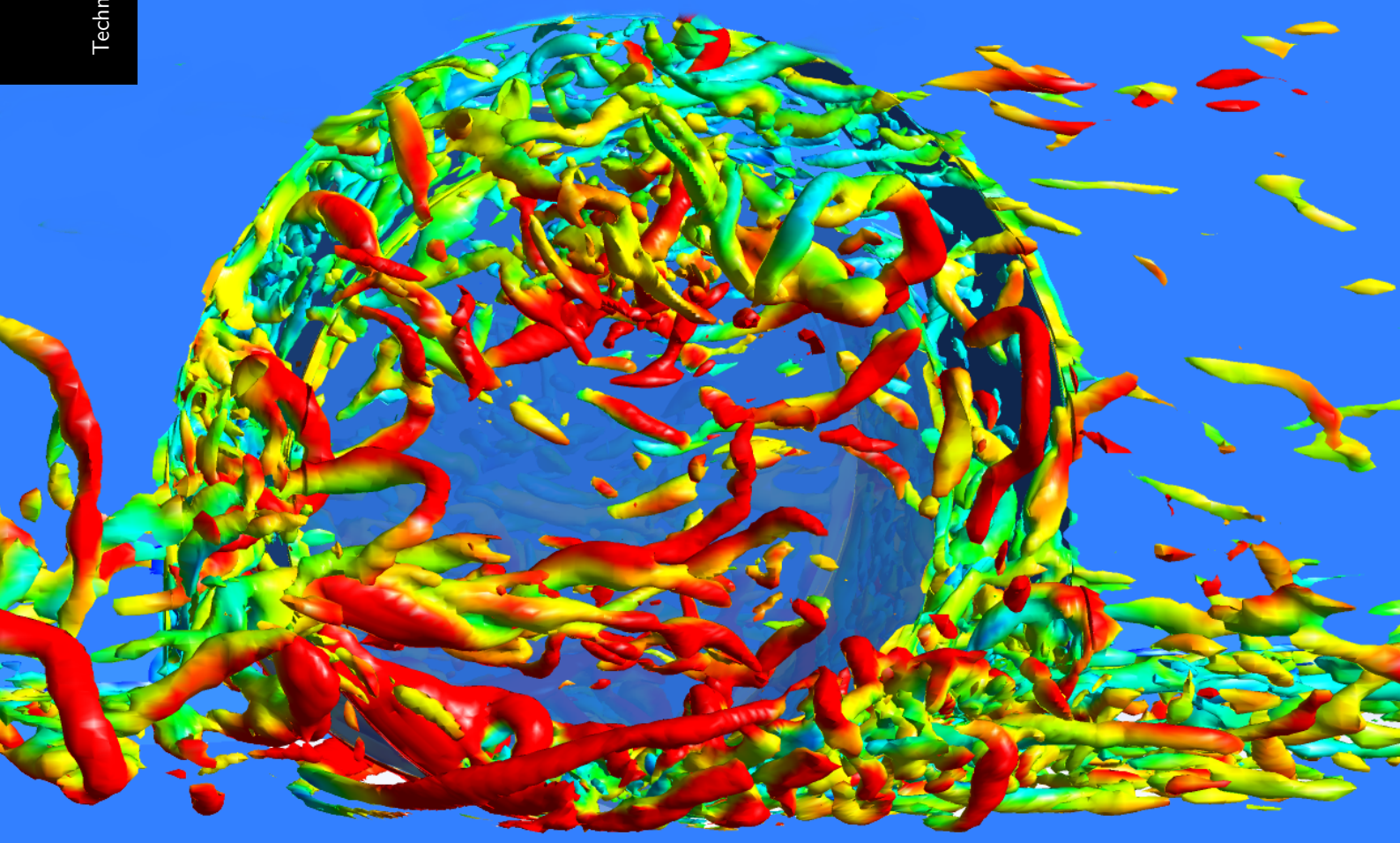

# AERODYNAMICS OF A ROTATING WHEEL IN A WHEELHOUSE

## A NUMERICAL INVESTIGATION USING LES

by

**Veeraraghavan Viswanathan**

in partial fulfillment of the requirements for the degree of

**Master of Science**
in Mechanical Engineering

at the Delft University of Technology,
to be defended on Monday October 23, 2017 at 09:00 AM.

**P & E Report Number : 2856**

| | | |
|---|---|---|
| Supervisors: | Dr. ir. G.E. Elsinga | TU Delft |
| | Dr. ir. M.J.B.M. Pourquie | TU Delft |
| Thesis committee: | Prof. dr. ir. J. Westerweel, | TU Delft |
| | Dr. ir. A.H. van Zuijlen, | TU Delft |



TU Delft Delft University of Technology

# Acknowledgement

To my supervisors, Dr. Elsinga and Dr. Pourquie, thank you for being patient with me and encouraging me along the way. I am really grateful to you both, for giving me the opportunity to pursue a research in my field of interest. I am also thankful to my friends Keerthi, Sai, Vaibhav, Adi, Praveen and to many more, for being supportive during the last 9 months. And of course, to my mother and father, I am always grateful to you both.

# Abstract

The aerodynamic drag force is a crucial factor for passenger cars and trucks, where fuel economy is of utmost importance. While a lot of research has been performed to optimize the design of the upper-body of the vehicle, the flow over a rotating wheel that is enclosed by a wheelhouse is not understood to the same level. Estimates show that the addition of wheel and wheelhouse to a vehicle body, can increase its drag and lift coefficient by as much as 40 %. With the major automobile manufacturers striving to improve the fuel economy of the vehicle, understanding the flow over a rotating wheel in a wheelhouse, offers a new dimension for the improvement of the drag coefficient of the vehicle.

In the present research, the flow over a simplified car body with a wheel and a wheelhouse was studied using Large Eddy Simulation (LES). When performing an LES on a given numerical grid, it can be expected that the contributions from the subgrid viscosity model reduces on decreasing the Reynolds number of the flow. A study focusing on the dependence of the flow field on the Reynolds number were thus performed. Three Reynolds numbers based on the wheel diameter - 9 x $10^3$, 75 x $10^3$, 150 x $10^3$- were chosen for the dependence study. A comparison of the relative pressure distribution and the flow topology between the different Reynolds numbers showed that the flow over a rotating wheel in a wheelhouse was qualitatively independent of the Reynolds numbers considered in this work.

Experimental results from Particle Image Velocimetry (PIV), performed on a similar vehicle model, was used to validate the numerical solution at a Reynolds number of 9 x $10^3$. The behaviour of the flow in the wheelhouse region was investigated and a new description of the flow field inside a wheelhouse, consisting of 11 vortex structures, was presented in this work.

To determine the qualitative dependence between the flow field and the drag coefficient, a comparison of the flow between two geometric configurations, with different wheelhouse radius, was performed at a Reynolds number of 9 x $10^3$. It was found that the configuration with the larger wheelhouse radius had a higher wheelhouse drag coefficient and a lower wheel drag coefficient when compared to the configuration with lower wheelhouse radius. Based on a detailed flow field, four out of the eleven vortices were found to be crucial in determining differences in the drag coefficient of the wheel and wheelhouse. Based on this analysis, an alternate wheelhouse geometry, combining the advantages of the two geometric configurations considered in this work, was proposed, that could potentially lead to a reduction in the drag coefficient of the vehicle.

*Keywords: CFD, LES, Aerodynamics, Wheel, Wheelhouse, Automobile.*

# Contents

# List of Symbols

| Symbol | | Usage |
|---|---|---|
| $Re$ | : | Reynolds Number |
| $C_D$, $C_L$ | : | Drag and Lift Coefficient |
| $C_d$, $C_l$ | : | Sectional Drag and Lift Coefficient |
| $C_d^+$, $C_l^+$ | : | Normalised Sectional Drag and Lift Coefficient |
| $C_p$ | : | Coefficient of Pressure |
| $D, r$ | : | Diameter/radius of the wheel |
| $R_{wh}$ | : | Radius of wheelhouse |
| $Z_w^+$ | : | Relative wheel position |
| $Z_{wh}^+$ | : | Relative wheelhouse position |
| H | : | Height of the vehicle model |
| $U_\infty$ | : | Free stream velocity |
| $y^+$ | : | non-dimensional wall distance |
| u', v' | : | Root mean squared of velocity fluctuations |
| $\overline{U'V'}$ | : | Turbulent shear stress |
| $Q$ | : | Second invariant of velocity gradient |

# List of Abbreviations

| Abbreviation | | Usage |
|---|---|---|
| CFD | : | Computational Fluid Dynamics |
| LES | : | Large Eddy Simulation |
| RANS | : | Reynolds Averaged Navier-Stokes equations |
| URANS | : | Unsteady Reynolds Averaged Navier-Stokes equations |
| PIV | : | Particle Image Velocimetry |
| WALE | : | Wall-Adapting Local Eddy-Viscosity |
| RBL | : | Rotating Boundary Layer |
| RMS | : | Root Mean Squared |

# List of Figures

# List of Tables

# Chapter 1

# Introduction

The aim of the present chapter is to give an overview of the importance of aerodynamics in automotive industry. Based on this overview, the context behind pursuing the present work on wheel aerodynamics will be established following which, the structure of the report will be presented.

## 1.1 Background

Aerodynamics of automobiles have an important role in deciding the drag and lift of the vehicle. Other areas of application include the control of wind noise produced, engine cooling, regulating the spray of water and dirt from the wheels, among others [1]. Figure 1.1 gives details of the entire spectrum of automotive aerodynamics as illustrated in [1]. Reduction of drag coefficient is the main focus of the present research and hence a brief introduction on the impact of aerodynamics on fuel economy will be presented in the following section.

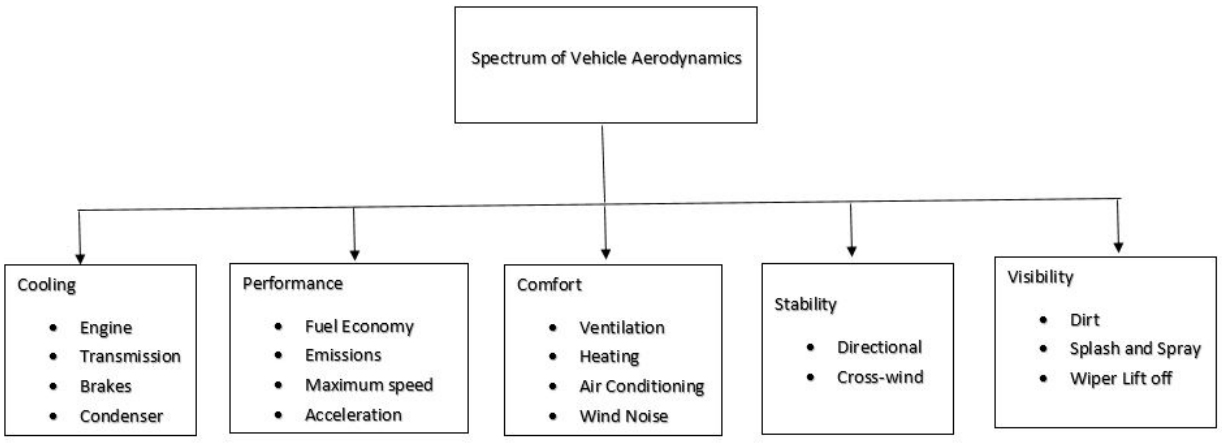


Figure 1.1: The complete spectrum of vehicle aerodynamics. The image was recreated based on illustrations given in book on vehicle aerodynamics [1]

## 1.2 Aerodynamics and efficiency

A typical vehicle that is in motion can experience all or a combination of the following resistances:

- Air resistance (D)
- Rolling Resistance(R)
- Gradient resistance
- Inertial resistance due to mass of vehicle

Naturally, fuel consumption will depend on the power required to overcome the above mentioned resistances. The air resistance or the aerodynamic drag force acting on the vehicle has a quadratic dependence on the velocity as shown in equation 1.1. The rolling resistance was found to have a linear relationship with velocity and the weight of the car (refer figure 1.2). While the air and rolling resistances can be represented as a function of velocity, the same cannot be said about the other two resistances. Gradient resistance, also called the climbing resistance, refers to the extra effort needed to climb an inclined road. The inertial resistance refers to the effort needed to overcome the inertia of the body during acceleration. A more detailed analysis of these parameters can be found in the book on ground vehicle aerodynamics [1]. Thus, considering a car moving on a flat road at a constant velocity (i.e neglect effect of inertia and gradient resistance), the two main ways to reduce the fuel consumption would be to (a) reduce the air resistance or (b) reduce the weight of the car. Since the present research is focused on aerodynamics, the focus would be on reduction of drag force acting on the vehicle. The aerodynamic drag force can be defined as follows:

$$D = \frac{1}{2}\rho U^2 A C_D \tag{1.1}$$

where, $\rho$ is the density of air, U is the velocity of the vehicle, A is the frontal surface area of the vehicle and $C_D$ is the drag coefficient of the vehicle. So how much influence does the drag force have on the fuel economy? This can be estimated by determining the amount of work that needs to be done to overcome the air resistance, for which the drag force needs to be calculated. Using equation 1.1, the value of air resistance for different vehicle speeds can be estimated which is shown in Figure 1.2.

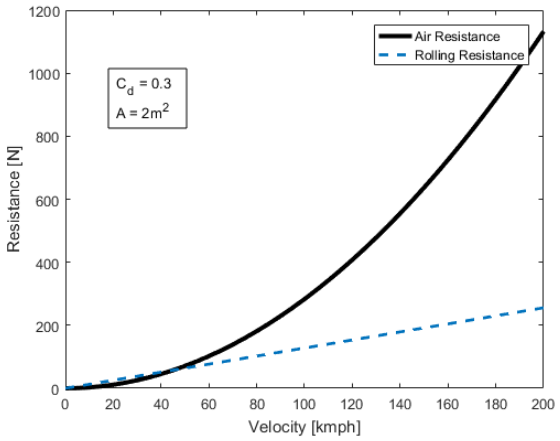


Figure 1.2: The variation of drag force with speed for a typical vehicle with a drag coefficient of 0.3 and frontal area of $2m^2$. The contribution of drag force becomes more evident at higher speeds i.e greater than 80kmph. Over a distance of 1km, the vertical axis can also be interpreted as the work required to overcome air resistance (in kJ).

At higher velocities, it can be seen that the contribution of air resistance starts to dominate over the rolling resistance. The percentage contribution of drag to total vehicle drag is shown in figure 1.3, where it can be seen that at at higher velocities (greater than 80kmph), more than 50 % of the total drag is due to air resistance,. Thus, it can be concluded that at higher speeds, a greater percentage of work is done to overcome drag resistance or in other words a greater amount of fuel is consumed to overcome drag resistance. Having established the importance of air resistance, how can the influence be minimized ?

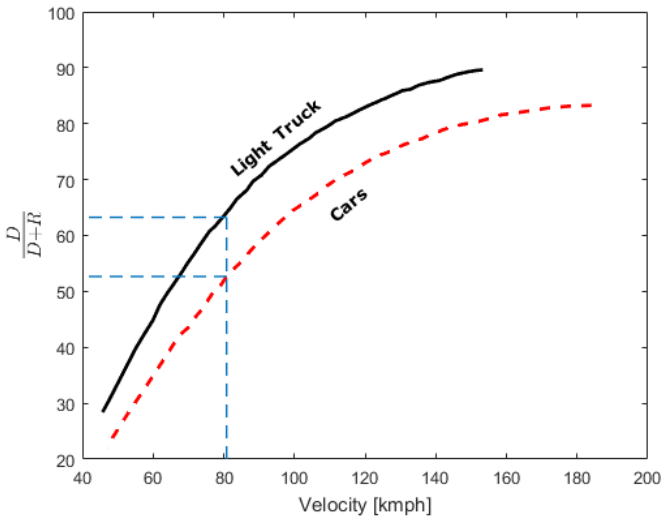


Figure 1.3: The proportion of drag force on the total resistance to movement, also known as Road Load. It can be observed that at speeds greater than 80kmph, which represents typical highway speed, more than 50 % of the total road load is due to air resistance. Image recreated based on plots from [1]

Based on equation 1.1, it can be inferred that the drag force depends on three factors (i) velocity of vehicle (ii) the frontal area of the car and (iii) The drag coefficient. So, for a given velocity, the aerodynamic drag force can be reduced by either reducing the frontal surface area or improving the drag coefficient of the vehicle body. While reduction of frontal area can be seen as an easy method, the amount by which it can be reduced is limited by consumer requirements. Thus, the only option to reduce the drag force is to reduce the drag coefficient of the vehicle. Looking back at equation 1.1, the drag coefficient is a non-dimensional quantity that depends on the shape of the body. Plenty of research has been done on the design of the upper body and can be broadly classified into two parts :

- *Research focusing on the front end:* This includes studies on front spoiler, windshield angle, leading edge radius to name a few (refer Figure 1.4a).
- *Research focusing on the rear end:* Studies on rear slant angles including fast backs, notch and square backs (refer Figure 1.4b).

While the above mentioned changes were focused on altering the design of the upper body, the importance of including the effects of wheel rotation were later realized to be important. It has been determined from experiments that the addition of a wheel and wheelhouse to a simplified car body (like the Ahmed body) can increase the total drag by as much as 40 % [1][2] . While the flow over the upper body has been well studied, the behaviour of flow over a wheel enclosed in a wheelhouse is still not completely understood. Understanding the flow mechanics in this region could therefore lead to significant improvements in fuel efficiency of road vehicles. An ideal situation would be one in which the effect of addition of wheels to a car body is minimal or in other words, a 40 % reduction in drag coefficient.

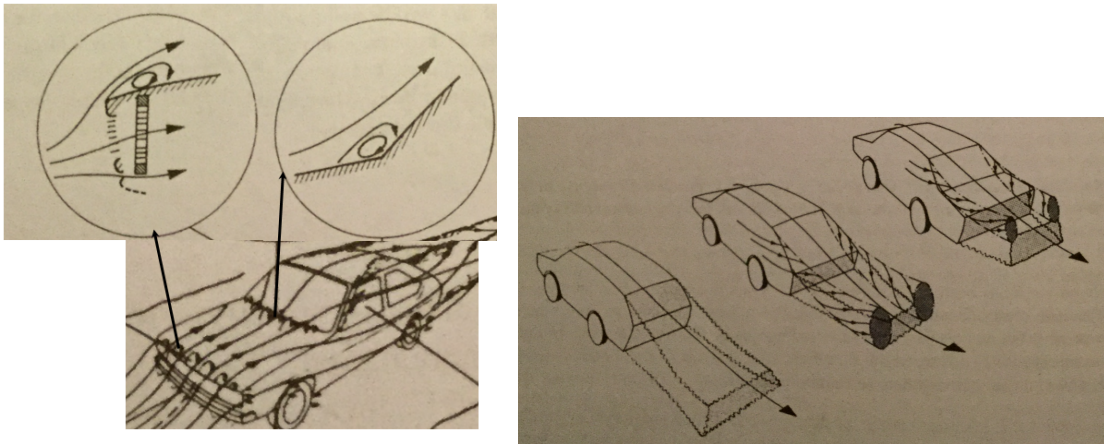

(a) (b)

Figure 1.4: Aerodynamics of upper body that has gained a lot of attention. (a) Shows the importance of aerodynamics in the front end depicting the influence of wing shield angle and the leading edge of the vehicle. (b) The three types of rear ends commonly found in passenger cars - fast back, square back and notch back. Image taken from [1].

## 1.3 Context and Motivation

While the influence of aerodynamics on fuel consumption was discussed in the previous section, the reviews by Zhang et al [3] and Katz [4] also gives insight into aerodynamics in motorsports. Without going into specifics, the majority of attention has been given to external aerodynamics of the upperbody; Be it single/multi element wing in ground effect and underbody diffusers in case of motorsports or the development of fast/notch backs , and profile alterations of car bodies in case of road vehicles. The field of wheel aerodynamics has not received a lot of attention. As the literature review (Chapter 3) will establish, the research on understanding the flow over wheel inside a wheelhouse is still at its infancy. Hence, the present work will focus on deciphering the complicated flow in the wheelhouse cavity

Another motivation for pursuing the current research can be attributed to the Nuon Solar Team (TU Delft). The team found that the torque required to rotate the wheels was more than what was predicted by their simulations. The mismatch could be due to the lack of understanding of the flow over the wheel in the wheelhouse. Thus, the present research was started in collaboration with an experimental work to provide an accurate picture of the flow field in question.

The ability of LES to resolve large scale structures (refer Appendix A) and capture the unsteadiness of the flow was the main reason for choosing this method to solve the problem under consideration. An added benefit of using a well resolved LES is the ability to test the accuracy of RANS and URANS calculations performed on a similar geometry. The computationally cheap RANS models are usually preferred to perform parametric studies and the comparison of these results with the solution from an LES can be crucial to gauge the reliability of such RANS calculations.

The main area of application will be in road vehicles - both passenger and heavy- and the focus would be on reduction of drag coefficient. The aim of the work is to give valuable insight into the behaviour of flow which can ultimately lead to an educated change in design of the wheelhouse and underbody.

## 1.4 Structure of the Report

The structure of the thesis is as follows. Chapter 2 will give a brief description of the flow field present as a result of a rotating wheel inside a wheelhouse. Following this, Chapter 3 will deal with the literature survey pertaining to the present flow problem based on which the research objectives are formulated. Chapter 4 will discuss the numerical model, looking at how the problem was simulated using computational methods. The results of the present research are divided into three parts. The first part, Chapter 5, will present the validation of the numerical simulation by making a qualitative and quantitative comparison of results obtained from the simulation with that of the experiments. Chapters 6 and 7 will provide the answers to the research questions formulated in Chapter 3. Finally, Chapter 8 will complete the thesis by presenting the conclusions and suggesting recommendations for future work.

# Chapter 2

# Wheelhouse Flow Topology

This chapter will give a brief introduction to flow features that are relevant to the present work. The schematic of wheel inside wheelhouse is shown in figure 2.1, depicting the various regions inside the wheelhouse cavity, which will be used in the description of the flow field in the following section.

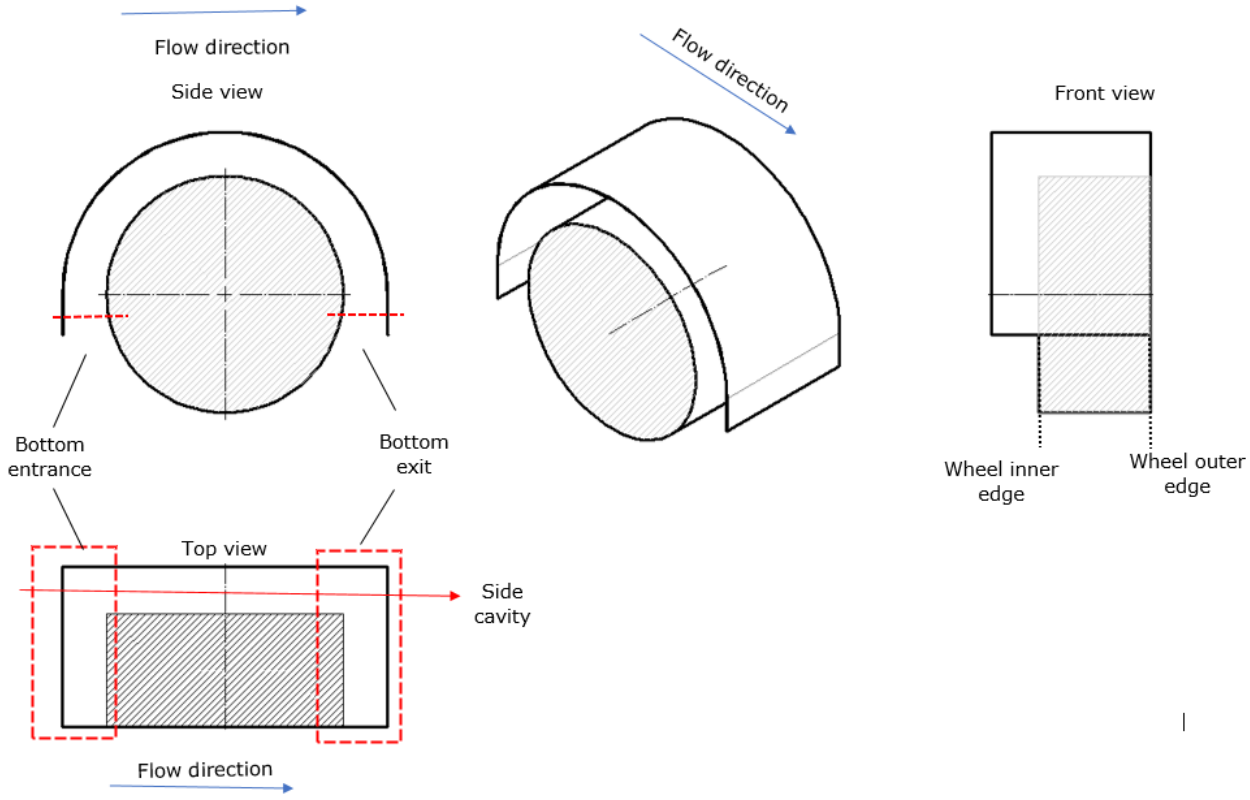


Figure 2.1: Schematic of the wheel-wheelhouse geometry depicting the various regions inside the wheelhouse cavity. The wheelhouse cavity is the region between the wheel and wheelhouse.

## 2.1 Description of Flow field

The flow entering the wheelhouse cavity interacts with the rotating wheel and the stationary wall of the wheelhouse resulting in a complicated system of flow structures. For a typical wheel-wheelhouse configuration found in road cars, the mean flow topology is found to consist of 11 vortices. It has been found from simulations by Regert et al [2], and also verified in the present work, that the majority of the flow entering the wheelhouse cavity does so using

the bottom entrance. From here on, the interaction of flow with the wheel and wheelhouse results in the formation of a system of vortex structures. These vortex structures, identified using techniques that will be discussed in Section 3.3, are described below:

1. The flow entering the wheelhouse cavity from the bottom, experiences a suction at the corner, which results in the flow rolling about the axis parallel to the wheel, forming the H vortex (figure 2.3a).

2. A part of the H vortex flows to the top of the wheelhouse cavity. The low pressure region present on top of the wheel results in the flow exiting the wheelhouse cavity from the top, forming A vortex (Figure 2.2c and 2.3a).

3. Another part of the flow entering the wheelhouse cavity as the H vortex, experiences a suction along the inner edge of the wheel. The low pressure deflects the H vortex, which then travels along the side cavity as the E vortex (Figure 2.2c and 2.3b).

4. The flow travelling along the side cavity recirculates due to the presence of the wheelhouse wall and exits the wheelhouse cavity from the bottom, forming the B vortex (figure 2.3b).

5. The approaching boundary layer along the side of the vehicle, separates from the leading edge of the wheelhouse arch forming the C vortex (refer figure 2.4). A good representation of C vortex is also found in figure 6.8 and figure 6.10 in Chapter 6.

6. The flow separates from the leading edge of the wheel, forming a tip vortex (C1) (Figure 2.2b).

7. The flow exiting the wheelhouse cavity separates at the trailing edge of the wheelhouse arch (refer figure 2.2b and figure 2.3a). This forms the S vortex.

The description of the flow field, explained above, is based on the results of the present simulation. Figure 2.2 presents both the results from the present simulation and the vortex skeleton model proposed by Krajnovic et al [5] (refer figure 2.2a). The sense of rotation of the vortices in general and the behaviour of the B vortex is found to be different in the present work when compared to the previous finding. It should be noted that for all the subsequent discussions, the description of flow field presented in this chapter will be considered.

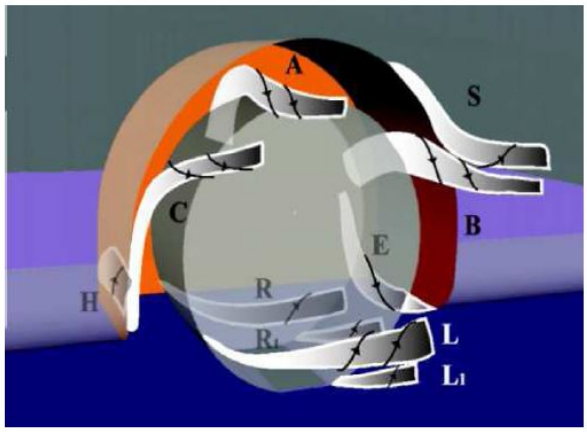


(a)

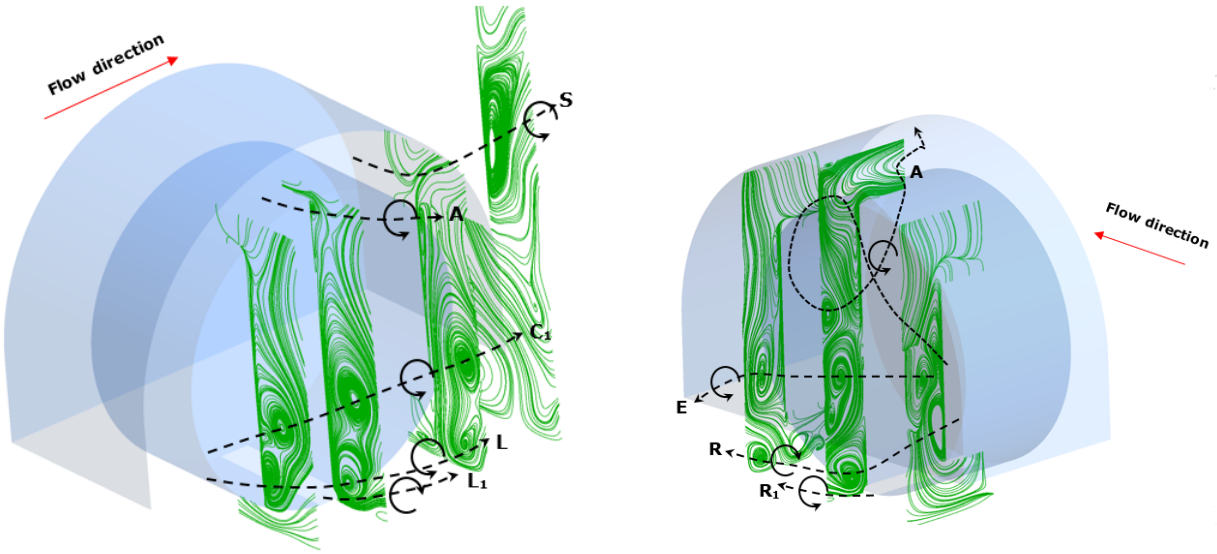


(b) (c)

Figure 2.2: The description of flow field in the region of wheelhouse first presented by Regert and Lajos and later verified by Krajnovic et al [5] is shown in (a). The flow topology visualized using surface streamlines based on the results obtained in the present work is shown in (b) and (c).

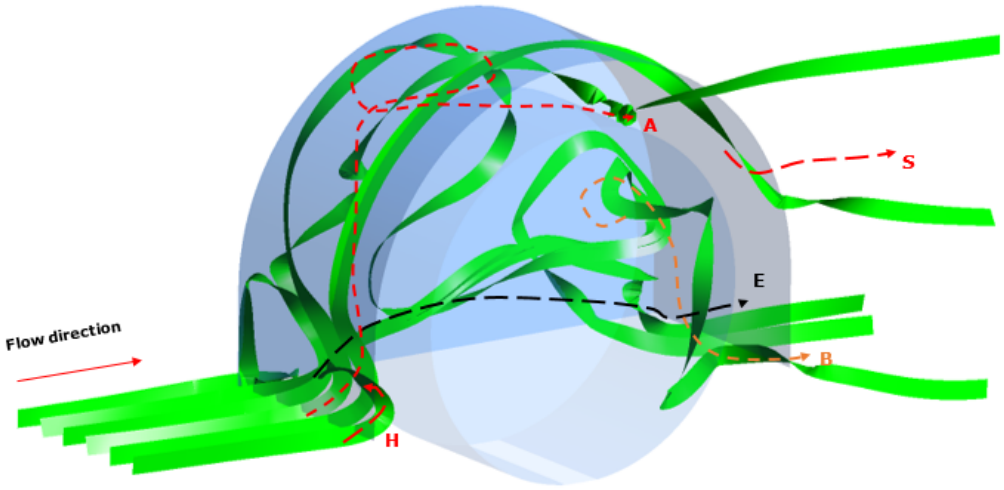


(a)

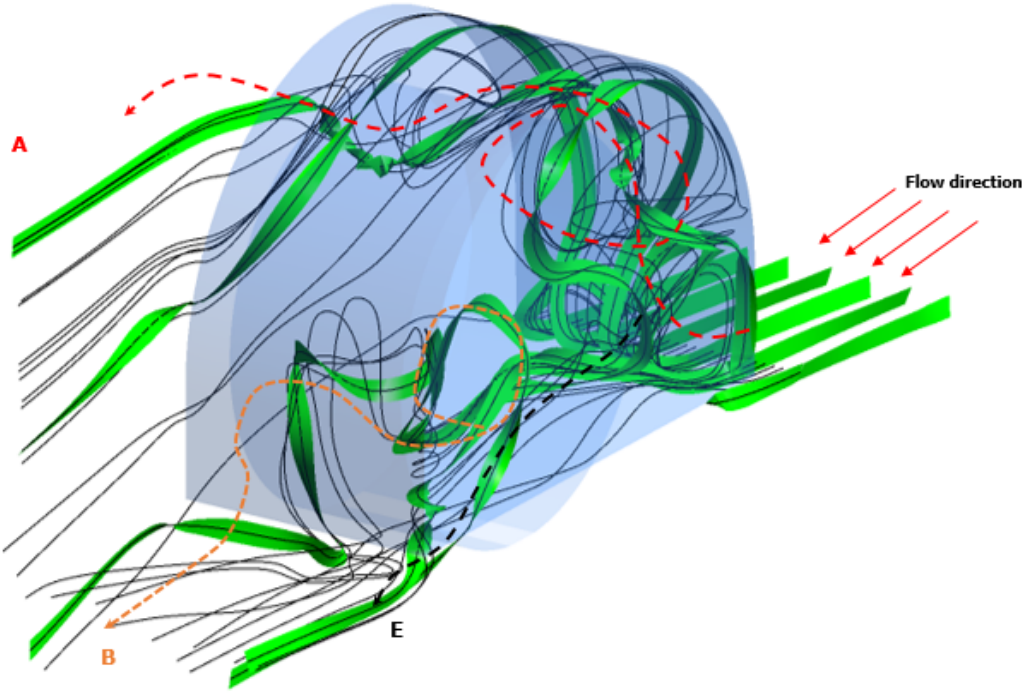


(b)

Figure 2.3: Use of 3d streamlines to visualize the various structures found in the wheelhouse region.(a) Streamlines (in the form of ribbons) are released from a line near the leading edge of the wheelhouse. The streamlines depict the average flow trajectories that results in the formation of the flow structures. The ribbons, which are initially aligned with the free stream, curls with the flow thus aiding in the visualization of these vortical structures. (b) shows the same "streamribbons" as seen from the back of the wheelhouse, superimposed with a denser streamline pattern.

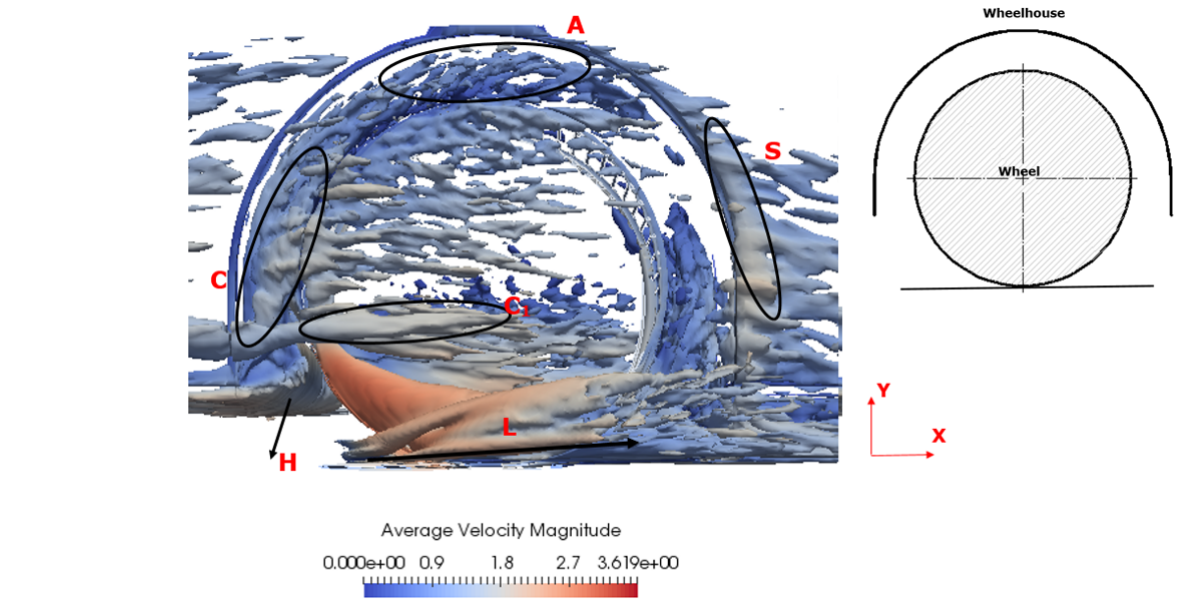


Figure 2.4: The use of second invariant of velocity gradient tensor(Q) to visualize the flow field inside the wheelhouse. The various structures discussed in this chapter is marked by their respective alphabets in the figure. The values of iso-surface shown here, ranges between $Q(D/U_\infty)^2$ = 20 and $Q(D/U_\infty)^2$ = 30, where D and $U_\infty$ represent the diameter of wheel and freestream velocity respectively.

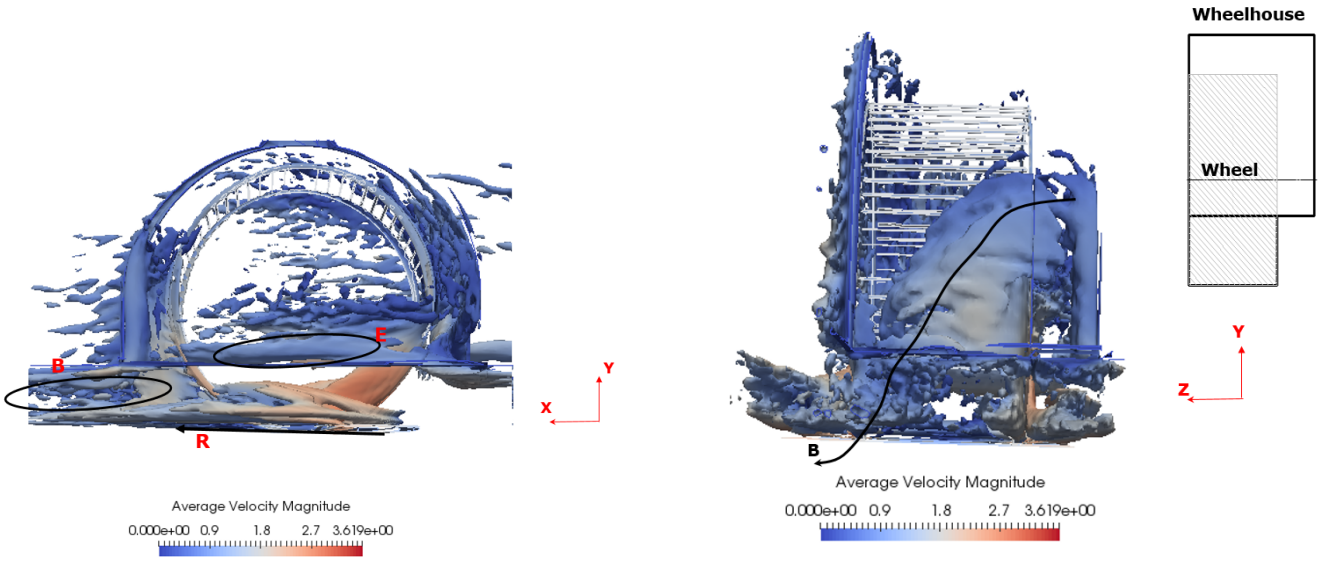


(a) (b)

Figure 2.5: Refer figure 2.4 for caption. (a) Flow is from left to right. (b) Flow out of the plane

## 2.2 The Contact Patch - Jetting Vortices

One of the most important characteristics of wheel aerodynamics, that is apparently present irrespective of the geometry of wheel or the Reynolds number is the pair of vortices emanating from the sides of the wheel at the point of contact with ground [2][5]. These vortices are termed "jetting vortices" and are found to be the most important contributor to the drag of the wheel. Hence, this section gives a brief description of the jetting vortices.

The phenomenon where flow encounters a wheel in ground contact can be grouped under a category of flow called juncture flows. A traditional juncture flow, where in a *stationary* bluff body is placed in contact with a *stationary* ground, results in formation of a horseshoe vortex which is created in the following way: The approaching boundary layer, experiences an adverse pressure gradient due to the presence of the solid blockage. This results in separation of the boundary layer and causes the flow to move around the obstacle. The above separation effect results in the formation of a horseshoe vortex as illustrated in figure 2.6a.

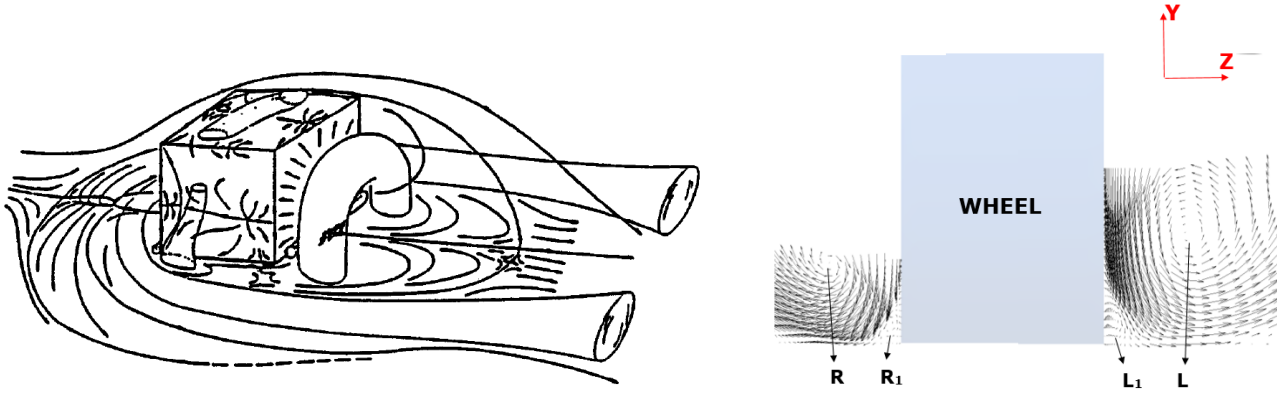


(a) (b)

Figure 2.6: (a) A horseshoe vortex emanating from the boundary layer separation around a cube in ground contact [6]. (b) The pair of jetting vortices emanating from the ground contact of a wheel, visualized at the mid plane of the wheel in the present work(flow is into the plane)

In the case of the wheel in ground contact the following two changes are observed: (a) the bluff body i.e the wheel is rotating. (b) The ground or in this case, the road, is moving. Even though the moving ground will eliminate the formation of a boundary layer, the flow experiences a extreme pressure gradient near the contact patch [1]. The pressure gradient is caused when the flow, which moves at a velocity matching the ground velocity, encounters the solid blockage. Here, the flow is forced laterally by the converging boundaries of wheel and ground, thus curling up and forming the jetting vortex (depicted in streamlines shown in figure 2.2b and 2.2c).

In case of a traditional juncture flow as explained above, the flow stagnates at the point where it comes in contact with the bluff body, i.e $C_p$ =1. But in case of a wheel rotating in ground contact, the converging boundaries of the wheel and road was found to impart additional energy to the flow which leads to a value of $C_p > 1$ at the contact patch[7]. The increased pressure at the contact patch is what makes the jetting vortices, the most important flow structure in a flow over a rotating wheel.

[1] Refers to the region of wheel in contact with the ground

# Chapter 3

# Literature Review

In this chapter, a brief overview of previous research performed on flow over a wheel inside a wheelhouse (or shrouded wheel) is presented. The summary of the previous works is aimed at highlighting the lack of available research focusing on understanding the behaviour of the flow field in question. Equally interesting is the research done on isolated wheel aerodynamics, but a detailed description will not be presented here and an overview is provided in the table at the end of the chapter.

## 3.1 Parameter Studies

The first work that will be discussed, based on which the present geometry was chosen, is the experiment performed by Fabijanic [8]. Some of the older works including that of Cogotti [9], while important will not be discussed in detail here since the work by Fabijanic can be considered as a successor to these works.

Fabijanic performed a series of experiments to find the dependence of lift and drag of the total vehicle on the wheelhouse geometry. The parametric study involved varying the depth and radius of the wheelhouse for a body with constant wheel diameter and ground clearance. The main observations from the experiment are as follows:

- The drag of the body was found to decrease with decrease in the radius of the wheelhouse (figure 3.1a).
- The lift of the body was found to have a non-linear relationship with the wheelhouse depth. A decrease in lift of the body was observed upon increasing the wheelhouse depth until a certain depth following which, further increase in depth resulted in an increase in lift (figure 3.1b).

While a proper theory was lacking to explain the decrease in drag of the body with decreasing wheelhouse radius, it was theorized that the observed decrease in lift could be attributed to the change in strength of the low pressure jet emanating from the wheel contact i.e jetting vortex. Another important inference from the above work was the importance of modelling the ground contact condition accurately. While a linear relationship between force and wheelhouse geometry was previously observed by Cogotti, the work by Fabijanic showed a non-linear relationship as shown in figure 3.1.

Axon[10] was the first person to perform numerical studies on both isolated and shrouded wheel aerodynamics. The work included a comparative study on the effect of turbulence models on the solution of isolated wheel aerodynamics. Pertaining to shrouded wheels, the influence of height of a wheel spoiler on the drag coefficient of the wheel was investigated. The effect of addition of spoiler was found to decrease the pressure on the contact patch of the wheel thus reducing the drag coefficient of the wheel (refer Figure 3.2). This result points to the importance of jetting vortex on the wheel drag.

The work by Schwarczkopf et al [11] used realizable k-$\epsilon$ turbulence modelling on an unstructured grid for solving the flow around an Ahmed body with wheels. The research involved the study of simple add-ons to reduce drag - using baffles, vortex generators and open rims (refer figure 3.3). The results are summarized as follows:

- The use of baffles to straighten the flow in the underbody, which is normally yawed due to the lateral suction created, did reduce the drag of wheel but the total body drag remained almost unchanged due to the self drag of the baffles.
- The reduction of drag coefficient on addition of trapezoidal vanes, which mimics the function of baffles, was found to be low. Due to its lower self drag, the authors claimed that a proper positioning of vanes would results in a better drag reduction.
- A semi open rim was used instead of a solid wheel, which was found to be the most effective in terms of reduction in drag value.

As can be seen from the above conclusions, the study performed gives an idea of the influence of geometry on drag coefficient, but the underlying physics has not been investigated in detail. A similar trend, where the overall influence is given more importance, is observed in the work done by Mavuri et al [12].

Mavuri et al [12] performed a study using RANS to find the effect of wheel and wheelhouse on the drag coefficient of the vehicle. The parametric study involved varying: (i) the geometry of wheel and wheelhouse which included the length, width and the depth (ii) variation in edge profile using both fillets and chamfers (iii) using angled wheelhouse covers (iv) varying the ground clearance and finally (v) use of deflectors and skirts. The individual effects of the above parametric analysis was documented and the main conclusions of the work were:

- Wheel and wheelhouse account for a significant portion of the drag coefficient of the a road car.
- The aerodynamic influence of the front wheel and wheelhouse was dependent on the flow impinging on the wheel surface.
- The aerodynamic influence of the rear wheel and wheelhouse was sensitive to the geometry of the wheelhouse.
- An optimally designed wheelhouse could lead to a significant improvement in the drag coefficient of the vehicle.

The first ever description of the flow field for a rotating wheel inside a wheelhouse was presented by Regert and Lajos [2]. To capture the unsteadiness of the flow, they performed a URANS using the k-$\omega$ SST turbulence model. Apart from describing the mean flow topology (which was discussed in Chapter 2), the work also included a parametric study involving (i) variation of nose length to study the effect of yaw angle of the flow approaching the wheel (ii) the effect of closing the side and bottom cavity of the wheelhouse on the drag and lift coefficients. The results can be briefly summarized as follows:

- The angle of approach of the flow with respect to the streamwise direction was found to decrease when the nose length was higher.
- The change in drag and lift of the wheel on closing the bottom opening was found to be more significant than the closure of the side opening.

In the above simulation, the authors found that the drag coefficient of the wheel reached a constant value after the flow has completely developed. But when the same flow was solved using LES by Krajnovic et al. [5], they found that the drag coefficient of the wheel showed an oscillating behaviour. This points to the level of unsteadiness of the flow and

the need to use a suitable method for solving the flow problem in question that can capture the unsteadiness. The work by Krajnovic et al. [5] marks the first ever LES on the flow over wheel in a wheelhouse. The study was performed on the Fabijanic body using the Smagorinsky model with a Van-driest damping function. The results of the work can be broadly summarized as follows:

- The description of the flow provided by Regert et al. was validated in the study. In addition to validation, new flow structures were identified, that can be attributed to the ability of LES to capture the unsteadiness.
- A basic comparison of the flow on changing a geometric parameter i.e the wheelhouse depth, was performed.

The main conclusion from the work by Krajnovic was that LES is able to accurately describe the flow in question with feasible computational resources.

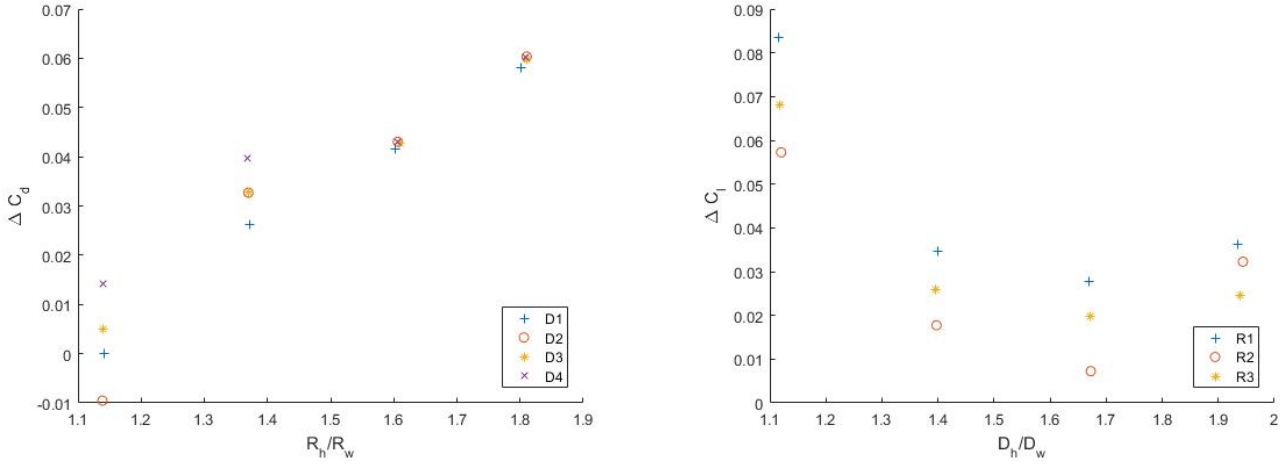


(a) (b)

Figure 3.1: Results from the experiments of Fabijanic that shows the dependence of drag and lift coefficient of the vehicle on the wheelhouse geometry. (a) shows the variation of drag coefficient with radius of wheelhouse ($R_h$) for various wheelhouse depths(D). (b) shows the variation of lift coefficient with the depth of wheelhouse ($D_h$) for varying wheelhouse radii (R). The vertical axis in both plots represent the increase/decrease of the force coefficients with respect to a reference body with no wheel and wheelhouse.

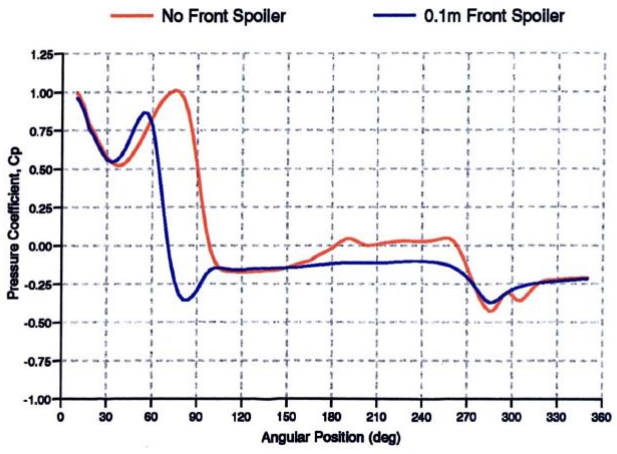


Figure 3.2: Pressure distribution along the centre line of a stationary wheel as determined by Axon [10]. The addition of a wheel spoiler shows a reduction in the pressure at the contact patch which could be the main reason for observed reduced drag of wheel.

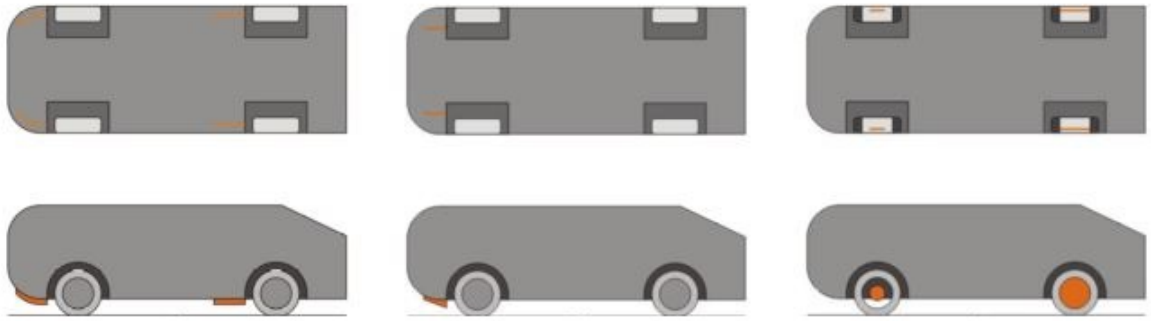

Figure 3.3: The various geometries investigated by Schwarczkop [11] for drag reduction of an Ahmed body with wheels. (from left to right). Figures show the use of baffles, vortex generators and semi open rims to find their respective effects on the drag coefficient of the vehicle.

## 3.2 Studies on effect of ground simulation

An important parameter that is given a lot of importance is the difference observed on the flow field, between stationary and rotating wheel on a stationary or moving ground, beginning from Fackerell and Harvey's [7] original work on isolated wheel aerodynamics. The reason for the popularity of this field of research is the difficulty in experimentally simulating proper ground contact with rotation of wheels.

The study by Axon [10] included the effects of ground plane (moving or stationary) and wheel rotation. From the simulations and experiments, the conclusion was that the rotating wheel with moving ground produced more drag than a stationary wheel on a stationary ground. Reiterating the results of Fabijanic, a mismatch in dependence of force with wheelhouse geometry was observed when compared to the work done by Cogotti [9], and this variation was attributed to the effect of ground simulation.

Waschle [13] performed a detailed CFD and experimental study on a production car (Mercedes-Benz E class) on the effect of wheel rotation. LDV[1] was used to map velocity profiles in different cross-sections which provided data to validate CFD results obtained using the k-$\epsilon$ model solved using Star-CD solver. The MRF[2] method was used to simulate the cross-flow through the wheels. The main findings of this study was the difference in the underbody wake flow between stationary and rotating cases. The rotation of wheels had two effects:

- It produced a narrower wake behind the wheels improving the underbody flow. This improved flow resulted in a reduction of lift of the body.
- The narrower wake led to a smaller separation bubble at the rear of the car which reduced the drag force acting on the vehicle.

The above study by Waschle was performed on a specific mass produced car and hence the results are specific to the mentioned geometry. Soderblom [14], on the other hand, performed a study on the effect of ground simulation on a generic truck body. A comparison of flow field was made, between the case of stationary wheel on a stationary ground and a rotating wheel on moving ground, using LDV. The results revealed a dependence of ground simulation on the outflow through the wheelhouse. The rotation of wheel was found to result in the flow exiting further downstream than in the stationary case, which led to differences in wake structures downstream of the wheel.

[1] Laser Doppler Velocimetry is a contactless measurement technique used for pointwise measurement of velocity

[2] Moving Reference Frame is a technique used in CFD to simulate rotating flows without a moving mesh

## 3.3 Vortex Detection

In chapter 2, the various vortices present in the flow field were discussed. Vortices are characterized by swirling flows with a low pressure core. Given their importance to the present flow field, a combination of different techniques commonly found in literature [15] have been used to detect vortices in this work.

1. *Streamlines*: Closed or spiral streamlines can be used to detect vortices. The figures in chapter 2 are a good example of how streamlines can be used to detect vortices. Figure 2.2b shows the use of 2D streamlines to represent vortices. It should be noted from the figure 2.2b that a closed loop is observed at the core of a 2d vortex, while the 3D streamlines shows a translating structures(figure 2.3a). Thus, successive 2D planes were used to visualize the formation of vortical structures, where the locus of the closed loop core in 2D planes represent the trajectory of the vortex core.

2. *Iso-surface of low pressure*: Vortices are usually characterized by a low pressure core and hence iso-surfaces of constant low pressures can be used to visualize the mean structures. The magnitude of low pressure of the core also gives an idea of the relative strength of the vortices that are visualized. Figure 3.4b shows a results from Krajnovic et al [5], where this method has been implemented to detect vortices for the flow under consideration.

3. *Q-criterion*: The second invariant of the velocity gradient tensor, Q is defined as: $Q = \frac{1}{2}(||\Omega||^2 - ||S||^2)$ and can be used to visualize vortices [16]. The second invariant, Q represents a local balance between strain rate (S) and rotation ($\Omega$) of fluid and hence positive values would represent domination of vorticity over strain rate. Iso-surfaces of positive values of Q can thus be used to visualize vortical structures, though the threshold for the values of Q is arbitrary[17]. Figure 3.4a again shows the results from Krajnovic et al [5], where this method has been implemented

Jeong et al [15] performed a review on the above mentioned techniques and while the accuracy of detection of vortices using these techniques were found to be dependent on the flow, the above mentioned techniques were found to perform well for the flow under consideration.

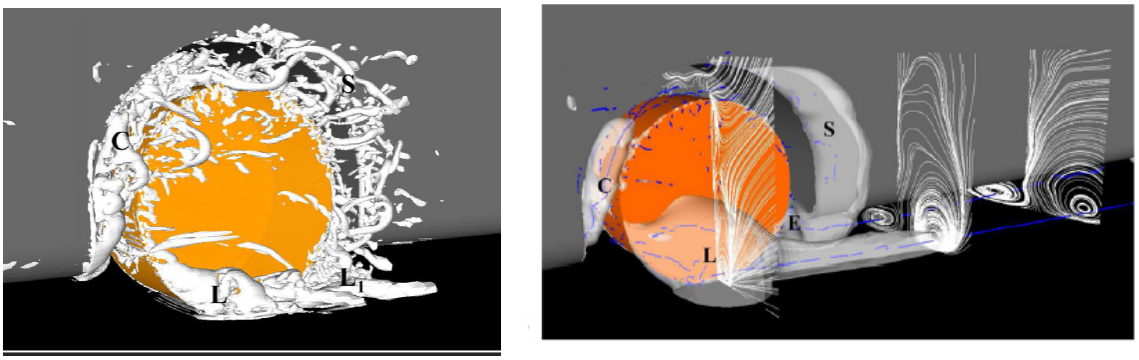


(a) (b)

Figure 3.4: Vortex detection techniques employed for the present flow problem in the simulation by Krajnovic [5] (a) Q criterion (b) (mean) iso surfaces of low pressure. The use of 2D streamlines to identify vortical structures is also shown in (b). The alphabets refer to the structures described in chapter 2

## 3.4 Conclusions and Research Objective

The amount of research that has been performed in this field, namely the wheel rotating inside a wheelhouse, has been surprisingly low. The combined literature on shrouded and isolated wheel aerodynamics, presented in tables 3.1 and 3.2, further signifies the scarcity of research performed in this field. Being a significant part of an automobile, the wheel aerodynamics has not been understood to the same level as the upper body (like the studies on Ahmed body [1]).

The previous sections provided a summary of the works that have been performed in this field, and they can be broadly classified as follows :

1. Studies focusing on the influence of wheel/wheelhouse geometry on the drag and lift coefficients.

2. Studies focusing on the effect of ground simulation on the force coefficients and flow field.

In addition, previous computational studies also included the effect of turbulence closure models on the solution (refer table 3.2). Thus, it can be seen that the research focusing on understanding the flow in the wheelhouse region and how the flow contributes to the forces acting on the body is lacking. This forms the main objective of the present work, in which Large Eddy Simulation (LES) will be used to solve the flow field around a simplified body with a wheel and wheelhouse. The flow field in two different geometric configurations will be compared, with a focus on identifying flow structures that may be responsible for an increase/decrease in drag of the wheel and body.

The two geometric configurations were decided by focusing the research on identification of drag reduction techniques. From previous experiments, a lower wheelhouse radius was found to reduce the total drag of the vehicle [8]. Thus, the radius of wheelhouse is chosen to be main parameter of the present work. The purpose of using a known low drag configuration is to, as mentioned before, make a detailed comparison of the flow field between the two cases.

The accuracy of an LES depends on the proportion of total turbulent energy determined by the sub-grid model. Since the energy at the smallest scales is dependent on the Reynolds number of the flow, it can be expected that, for a given numerical grid, the accuracy of an LES increases as the Reynolds number decreases. Since the main objective of the present work is on identifying, if any, a qualitative correlation between the drag coefficient and the flow field, what can be said about the dependence of the flow field on the Reynolds number ? This question will also be dealt with in the present work.

Thus, based on the above conclusions, the research objectives of the present thesis can be summarized as follows :

1. ***How dependent is the flow on the Reynolds number?***

2. ***How is the flow field affected when the radius of wheelhouse is reduced?***

3. ***Can the presence/absence of a particular flow structure be associated with a change in drag coefficient?***

Table 3.1: Summary of experimental results Isolated and Shrouded wheels.

| AUTHOR | REF. | Re-Number | L/D | WHEEL | TYRE | Ground | Condition | MEASURS. |
|---|---|---|---|---|---|---|---|---|
| Fackerell | [7] | 5.3 x $10^5$ | 0.6 | I | ND | C | RW-MR,SW-SR | IM,WM |
| Axon | [10] | 8.5 x $10^5$ | 0.3 | S | ND | C | RW-MR,SW-SR | DM,PM |
| Skea | [18] | 5.51 x $10^5$ | 0.125,0.5 | I,S | D | C | RW-MR | IM,WM |
| Fabijanic | [8] | 1.5 x $10^5$ | 0.47 | S | ND | C | RW-MR | DM,PM |
| Saddington et al | [19] | 6.8 x $10^5$ | | I | ND | C | RW-MR | WM |
| Van den Berg | [20] | 6.2 x $10^5$ | 0.55 | I | ND | C | RW-MR | DM,WM,PM |
| Waschle | [13] | $10^7$ | | OC | ND | C | RW-MR,SW-SG | WM |
| Issakhanian et al | [21] | 4.9 x $10^5$ | 0.5 | I | D | C | RW-MR | WM |
| Guylas | [22] | 2 x $10^5$ | 0.33 | S | ND | SG | RW-SR | WM |

L/D refers to the Aspect ratio of the wheel; WHEEL refers to either isolated(I),shrouded (S) or On car (OC); Tyre can be either Deformable (D) or non-deformable(ND); Ground contact could either be a Sealed gaps (SG) or contact (C); Condition refers to Stationary wheel(SW), Rotating wheel(RW),Stationary Road(SR), Moving Road (MR). Measurements (MEASURS.) refers to Direct (DM) or indirect (IM) measurement of force, Pressure measurement(PM) on wheel surface or Wake measurements(WM).

Table 3.2: Summary of results for CFD results Isolated and Shrouded wheels.

| AUTHOR | REF. | Re-Number | L/D | WHEEL | TYPE | CELLS | SOLVER | TURB. |
|---|---|---|---|---|---|---|---|---|
| Axon | [10] | 5.3 x $10^5$ | 0.61 | I | struct | 5.4 x $10^5$ | Steady RANS | RNG k-$\epsilon$ |
| Skea et al | [18] | 6.9 x $10^5$ | 0.5 | I,IF | struct | 3.6 x $10^5$ | Steady RANS | RNG k-$\epsilon$ |
| Waschle | [13] | $10^5$ | - | OC | struct | 33.2 x $10^6$ | Steady RANS | Std. k-$\epsilon$ |
| Van den Berg | [20] | 6.2 x $10^5$ | 0.55 | I | struct | $\sim$5 x $10^6$ | Steady RANS | S-A |
| McManus et al | [23] | 5.3 x $10^5$ | 0.46 | I | struct | 2.94 x $10^6$ | Unsteady RANS | S-A and k-$\epsilon$ |
| Paschkewitz | | 1.3 x $10^5$ | 4.5 x$10^6$ | IF | struct | - | Unsteady RANS | SSTk -$\omega$ |
| Regert et al | [2] | 1.52 x $10^5$ | | IF | unstruct | upto 4 x $10^6$ | Unsteady RANS | Comb. |
| Schwarczkopf et al | [11] | 7.65 x $10^5$ | 0.49 | IF | unstruct | 3.3 x $10^6$ | Steady RANS | Realizable k-$\epsilon$ |
| Krajnovic et al | [5] | 1.6 x $10^5$ | 0.47 | IF | structur | 12.5 x $10^6$ | LES | Smagorinsky |
| Axerio-Cilies et al | [24] | 5 x $10^5$ | | I | hybrid | upto 23 x $10^6$ | U/RANS and LES | Comb. |
| Croner et al | [25] | 9.1 x $10^5$ | 0.324 | I | struct | 9 x $10^6$ | Unsteady RANS | k-kl |
| Pirozzoli | [26] | <=1000 | 0.4 | I | struct | - | DNS | – |

Reynolds number is based on the wheel diameter; L/D refers to the Aspect ratio of the wheel; WHEEL refers to either isolated(I),shrouded (S) or On car (OC); TYPE of the mesh refers to either a structured(struct.) or an unstructured (unstruct.) grid; TURB. refers to the turbulence model used with the solver where Comb. refers to a combination of different models.

# Chapter 4

# Numerical Model

In this chapter, the general methodology adopted to study the previously mentioned objectives will be outlined. The chapter begins by presenting the various simplifications and assumptions made in this study, followed by the description of geometry and the meshing strategy used. The chapter ends with the summary of all the tests performed and their definition will be presented.

## 4.1 Assumptions and Simplifications

1. The geometry of wheel is simplified to a solid cylinder in ground contact. This means that the edge profile of the wheel is not modelled and the wheel hub was covered so as to prevent cross flow.
2. The wheel under consideration is non-deformable.
3. The flow is considered to be symmetric with respect to the x-y plane (refer Appendix C).
4. The effects of other geometric features in close proximity to the wheel, like the suspension system and the wheel axle has been neglected.

## 4.2 Dimensions and Definitions

The model considered for the present research is based on the simplified geometry used by Fabijanic [8] in his experiments and will be referred to in this work as the 'Fabijanic body'. In accordance with the assumption #3, the model was split along its mid-plane and only half the body was considered for the numerical domain. The relevant dimensions defining the geometry and the numerical domain are shown in table 4.1 and Figure 4.1. It can be seen that the dimensions of the vehicle model is considerably smaller than an actual car. The reason can be attributed to the restrictions posed by the dimensions of the test section of the wind tunnel where the experiments were performed.

Table 4.1: Absolute and relative dimensions used to define the numerical model. All but the radius of the wheelhouse ($R_{wh}$) are presented in this table.

| | 'Fabijanic Body' | |
|---|---|---|
| Parameter | Absolute Dimensions | Relative Dimensions |
| B | 250 mm | 1.97H |
| F | 750 mm | 5.90H |
| x1 | 200 mm | 1.57H |
| x2 | 3000 mm | 23.6H |
| W | 95 mm | 0.74H |
| H | 127 mm | 1H |
| L1 | 248.2 mm | 1.95H |
| L2 | 342.9 mm | 2.7H |
| r | 38.3 mm | 0.3H |
| D1 | 36.2 mm | 0.285H |
| D2 | 50.5 mm | 0.4H |
| c | 16.8 mm | 0.132H |
| Fr | 25.4 mm | 0.2H |

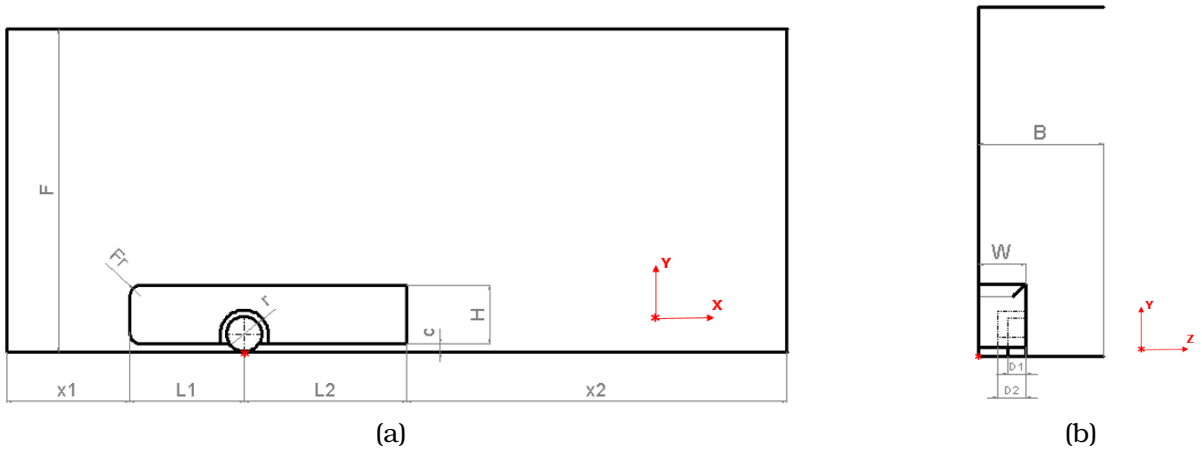


(a) (b)

Figure 4.1: Definition of dimensions. The numerical domain along with the definition of dimensions (a) side view and (b) front view. The red asterisk marks the origin of the coordinate system.

The coordinate system used is presented in the figure 4.1. The positive x-axis is taken as the direction along the flow, positive y-axis is the direction perpendicular to the flow upwards and positive z-axis is the direction perpendicular to flow and to the right of the model when viewed from front. x= 0 coincides with the centre of the wheel, y= 0 coincides with the ground plane and z= 0 coincides with the symmetry plane.

## 4.3 Grid Strategy

The accuracy of the numerical simulation is directly influenced by the quality of the mesh generated for the present geometry. But at the same time, there is the feasibility criterion that needs to be considered: While an extremely fine mesh will tend to an exact solution, it is not computationally economical. To achieve the required level of refinement without affecting the computational feasibility, the geometry was divided into three different regions each with its own mesh module. These modules were then meshed using ICEM CFD and combined using non-conformal interfaces.

### 4.3.1 Volume module - The Wind Tunnel

This module refers to the region that includes the velocity inlet and the far wake of the vehicle. Physically, this module would represent the wind tunnel - the inlet, the walls and the outlet - minus the region which contains the vehicle (refer figure 4.2).

A very coarse mesh is used since it is not necessary to resolve all scales in this region. The average length of an element is 4 mm near the entrance which then increases to 9 mm in the downstream section(values based on the cube root of average volume of an element). The total number of elements in this region is approximately 1.5 million. To justify the importance of using different mesh module with regions of refinements, consider the following: The average element size in the finest region of the domain (section 4.3.3) is 0.04 mm. A uniform mesh size would mean the entire volume needs to be filled with 6 x $10^{10}$ elements!

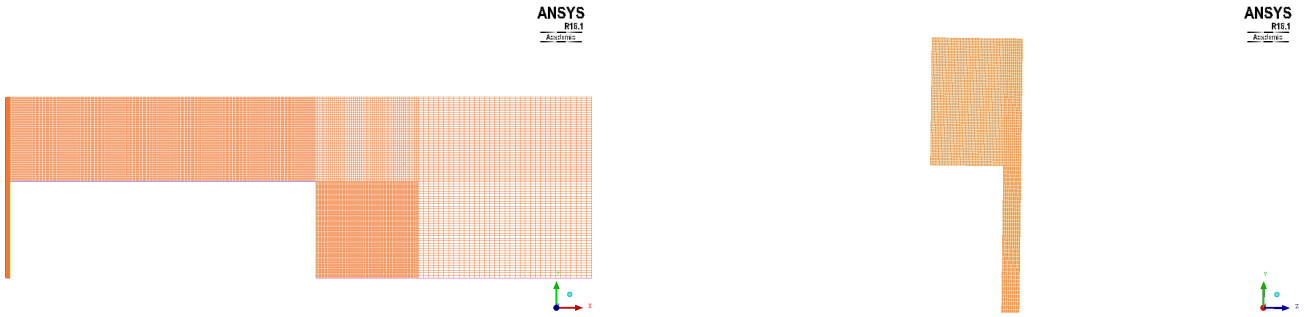


(a) (b)

Figure 4.2: The section of the mesh when viewed from (a) the side and (b) from the front. The rectangular gap is the region which will be filled with the other mesh modules.

### 4.3.2 Vehicle Module - The nose and aft

This module contains the region around the the vehicle minus the section containing the wheel and wheelhouse. An O-grid ensured a structured mesh around the body and edge biasing was used to define the cell thickness in the boundary layer. After a few iterations, the first cell thickness was finalized, which resulted in a $y^{+1}$ of less than 1. The average element size in this region was found to be approximately 1 mm which is 2.5 times higher than the finest region of the computational domain (section 4.3.3). The number of elements in this module came out to be approximately 4.5 million (refer figure 4.3).

[1]Wall $y^{+}$is defined for the simulation with lowest Reynolds number

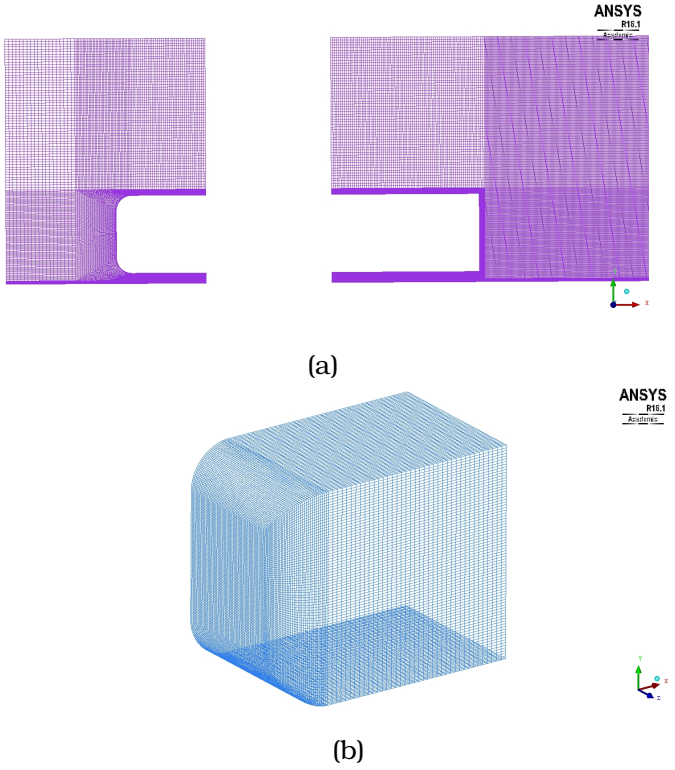


Figure 4.3: The section of the mesh when viewed from (a) the side and (b) close up of the surface mesh on the vehicle body. The thin rectangular region around the vehicle body is the O- grid which aided in controlling the growth of cells from the body.

### 4.3.3 Wheelhouse Module - The finest region

The wheelhouse module includes section of the wheelhouse and the wheel. Being the most significant region of the problem, this forms the region with finest mesh in the computational domain. The size of the mesh was based on the values from the work done by Krajnovic [5]. With 260 points along the circumference of the wheel, 60 points along the span of the wheel and 40 points in the gap between wheel and wheelhouse, a hexahedral grid was generated with approximately 5.1 million elements in this module. The complicated geometry of wheel inside the wheelhouse was addressed by a blocking strategy involving two O-grids which is shown in figure 4.4.

A wheel in contact with the ground creates a problem for the mesh generator due to the single point of contact. To overcome this, a section of the wheel was immersed into the ground (1 % of radius), which negates the problem with a single point of contact (refer figure 4.6). The size of the contact patch indeed has an effect on the solution as shown in [27] and the present value of 1% was based on previous works on wheel aerodynamics [5] [20] .

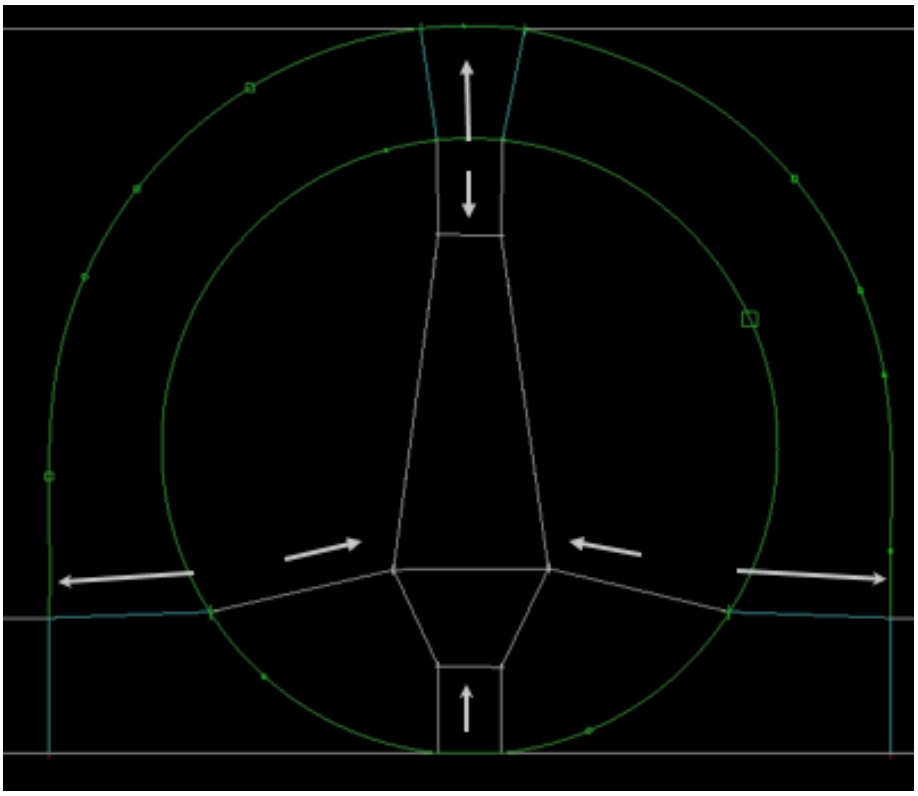

Figure 4.4: The blocking structure used in the wheel and wheelhouse region. An outward O-grid from the surface of the wheel is used to mesh the gap between wheel and wheelhouse . An inward O-grid is used to mesh the side surface of the wheel

After a few iterations, the near wall mesh size was fixed which resulted in a $y^+$ of less than or equal to 1 in this module. The majority of the elements, more than 80 % had an orthogonal quality of greater than or equal to 0.8. Low quality cells were however observed near the wedge (figure 4.6) which could not be avoided. The same can be said for the skewness where the minimum quality was observed in the wedge between the wheel and ground. With respect to aspect ratio, an ideal scenario would be a mesh having values close to one. High aspect ratio cells, however, could not be avoided especially near the boundary layer of the vehicle body where the mesh was coarser than in the wheel house region. But the majority of the cells, over 70 %, was found to have a value of less than 8.

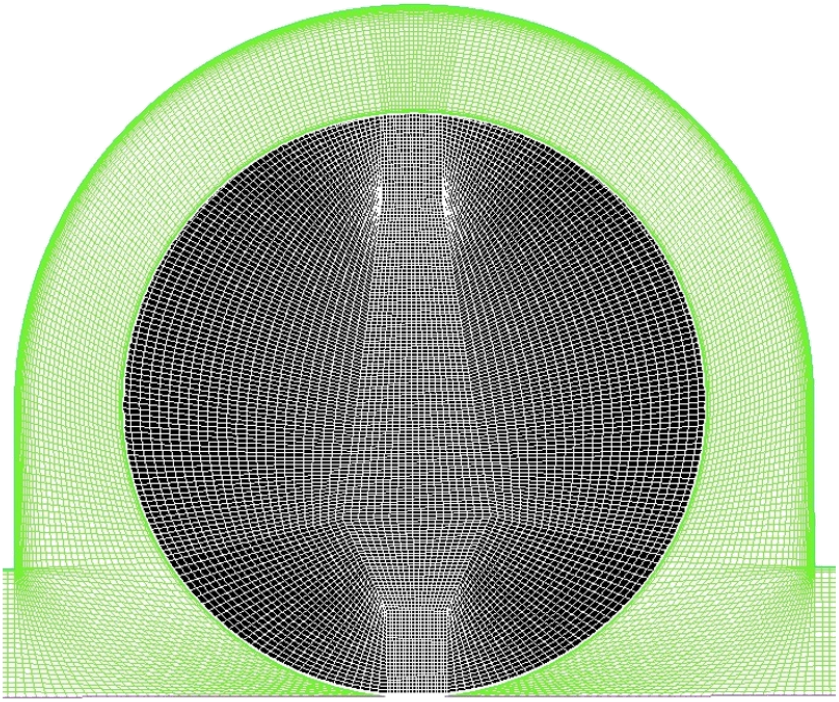

Figure 4.5: The mesh generated on the surface of the wheel (black) and in the gap (green).

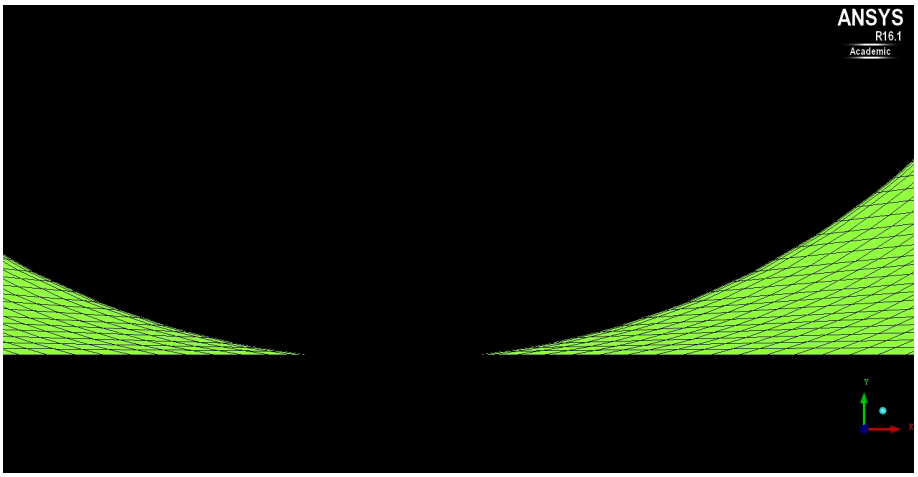


Figure 4.6: Close up of the sectional mesh in the wedge near the ground contact. The cells with poorest orthogonality were found in this region, which could not be avoided using the present blocking strategy

## 4.4 The Final Computational Domain

Once the three mesh modules were generated, the final computational domain can be obtained by combining the modules with non-conformal interfaces. To ensure that the interpolation across the interface is as accurate as possible, the ratio between the number of nodes across the interface, in a given edge, is kept below 6, i.e for every 6 nodes in the fine region there is a single node in the coarse region. The location of these interfaces were kept as far away from the region of interest as possible to avoid any numerical influence on the results. They were approximately at a distance of 1.5H in front of the vehicle, 4H behind the vehicle, 2H above the vehicle and 1.5H to the sides of the vehicle, where H is the height of the vehicle (refer figure 4.7).

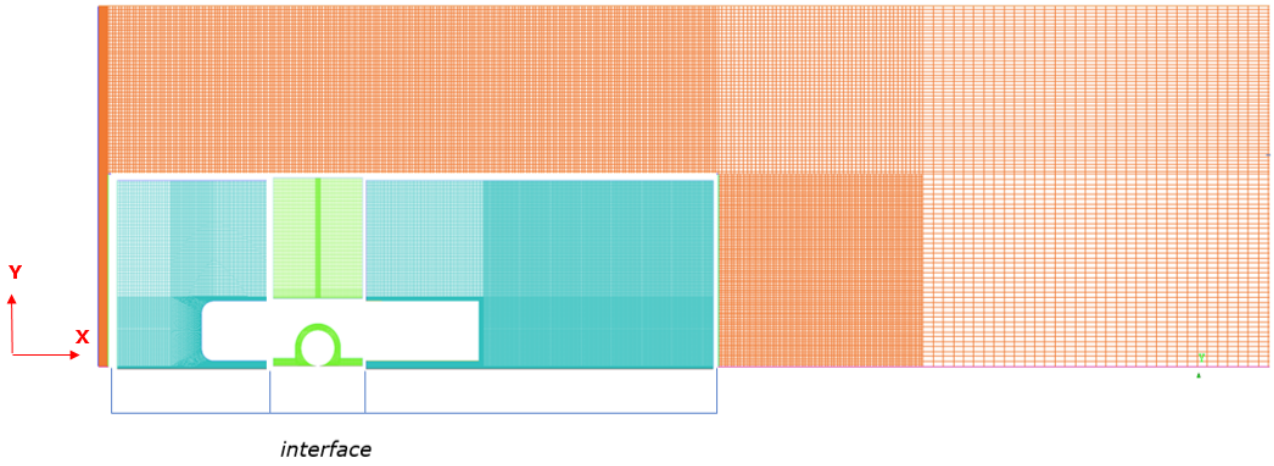


(a)

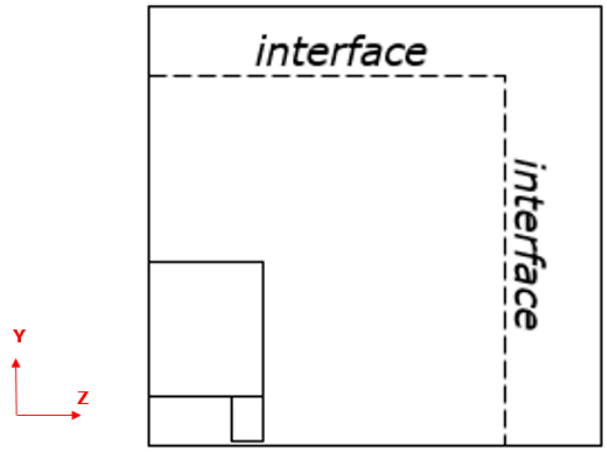


(b)

Figure 4.7: (a) (Side view)The section of the final computational domain where the different modules are assembled together. The green region is the Wheelhouse module, blue is the vehicle module and the red represents the volume module. (b) A schematic of the front view showing the location of the mesh interface.

## 4.5 Case Definitions

The number of simulations needed for the present work is determined by the research objectives. One set of simulations, named *Run 1*, is focused on determining the dependence of Reynolds number on the flow. Three Reynolds numbers based on the wheel diameter - 9 x $10^3$, 75 x $10^3$ and 150 x $10^3$ were chosen for this purpose. *Run 1* was performed on the Fabijanic body with a wheelhouse radius of 52.3 mm. Another set of simulations, named *Run 2*, is focused on comparing the flow field in the wheelhouse cavity, between two different geometric configurations wherein two different wheelhouse radii - 52.3 mm and 43.4 mm- were chosen. The details of *Run 1* and *Run 2* are presented in table 4.2 and 4.3 respectively.

While the above set of simulations were used to answer the research objectives of the present work, an additional simulation was needed to validate the numerical simulation ( the *Validation run*). The geometry used for validation was a modified Fabijanic body used by Ramani[28] in the water tunnel experiments performed at TU Delft. Since the focus of the experiments was velocity measurements using PIV, optical accessibility of the model was paramount. To ensure this, the amount of machining performed on the standard raw materials had to be minimized. Hence, certain modifications were made to the Fabijanic body, especially with the wheel and wheelhouse dimensions, which are presented in table 4.4.

## 4.6 Fluent case setup

Fluent 16.2 was used to solve the Navier-Stokes equations using Large Eddy Simulation. SIMPLE algorithm was used for pressure -velocity coupling. The momentum equations were discretised using central differencing and second order accurate implicit scheme was used for temporal discretisation. The time step size, for each Reynolds number was chosen to ensure that Courant number (refer Appendix A) in the finest region was less than 1.1. The time step size was thus, calculated to be 2 x $10^{-4}$ s and 1 x $10^{-5}$ s for the low Reynolds number ($Re_{1W}$) and high Reynolds number ($Re_{2W}$,$Re_{2S}$,$Re_{3S}$) cases respectively. The number of iterations per time step ranged between 10 and 20, for which the absolute value of the scaled residuals for continuity reaches 3 x $10^{-4}$, while that of the velocity components reaches 1 x $10^{-8}$.

The rotating wheel is simulated by modelling the wheel as a rotating wall. The road, i.e the bottom wall, is given a translating boundary condition with a velocity equal to free stream. The rate of rotation is calculated from the free stream velocity to ensure a no slip condition at the point of contact with the ground. The above mentioned boundary conditions are used for the *Run 1* and *Run 2*. For the validation run, however, the translating wall condition for the road was replaced with a stationary wall condition [2]. This was done because the experiment, against which the current numerical model is validated, was performed with a stationary road.

The preferred choice of subgrid model was the WALE model due to its accuracy in predicting near wall subgrid viscosity (refer Appendix A). But it was found that at higher Reynolds number, the combination of WALE with central differencing produced unphysical spikes in the drag curve. This problem disappeared when using the more diffusive Smagorinsky model (refer Appendix F). Taking this factor into account, a combination of the two sub-grid models was used for the simulations in *Run 1* as shown in the table 4.2.

The solution was run until a non-dimensional time ($tU_\infty/D$) of 200, which corresponds to 200 passes of flow across the wheel diameter. The flow was allowed to develop for a time period corresponding to 50 passes of the flow, after which statistics for the time averaging were collected. Statistical convergence of data was verified by comparing the value of drag coefficient, averaged over different time intervals.

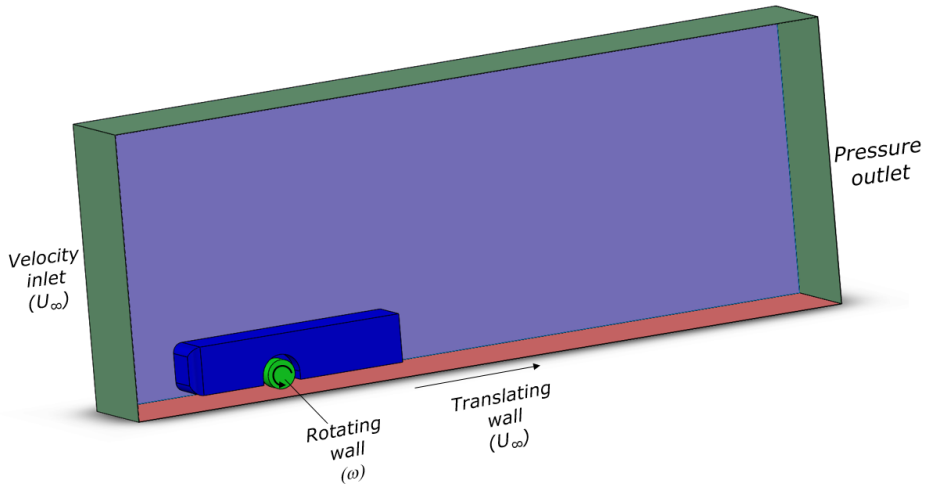


Figure 4.8: The boundary conditions used for the simulations. The vehicle body (blue) was given a no slip boundary condition while the remaining surfaces - side and top surface- were given a slip/symmtery boundary condition.

[2]The stationary wall condition was not applied to the entire road section. Instead only the part of the road in vehicle and wheelhouse mesh modules were set to stationary wall. This is a good representation of the ground plate used in the experiment.

Table 4.2: ***Run 1***

| Geometry : *Fabijanic body* | | | |
|---|---|---|---|
| Case name | Reynolds number (Re) | Sub-grid model | Free Stream Velocity [m/s] |
| $Re_{1W}$ | 9 x $10^3$ | WALE | 1.8 |
| $Re_{2W}$ | 75 x $10^3$ | WALE | 15 |
| $Re_{2S}$ | 75 x $10^3$ | Smagorinsky | 15 |
| $Re_{3S}$ | 150 x $10^3$ | Smagorinsky | 30 |

Table 4.3: ***Run 2***

| Geometry : *Fabijanic body* Re = 9 x $10^3$ | | |
|---|---|---|
| Case name | Wheelhouse radius($R_{wh}$) | Sub-grid model |
| Case1 | 52.3 mm | WALE |
| Case2 | 43.4 mm | WALE |

Table 4.4: ***Validation Run***

| Geometry : *Modified Fabijanic body* Re = 9 x $10^3$ | | |
|---|---|---|
| Wheel radius (r) | Wheelhouse radius ($R_{wh}$) | Sub-grid model |
| 45 mm | 61.5 mm | WALE |

# Chapter 5

# Results Part I - Validation

The results from the *Validation Run* will be discussed in this chapter. The velocity field obtained from Particle Image Velocimetry (PIV) will be used to validate the solution of the present simulation. The contribution of the subgrid viscosity model to the total turbulent stress will also be considered to verify the validity of the simulation.

## 5.1 The Experimental Model

The experiments, against which the simulation will be validated, were performed in the water tunnel facility at the Aero and Hydro Laboratory in TU Delft by Ramani[28]. As mentioned in Chapter 4, a 'Modified Fabijanic' body was used in the experiments in which the radius of the wheel and wheelhouse were chosen, such that the amount of machining needed on the raw material (Plexiglas) was minimized. This ensured that the transparency of the model was not affected which allowed the use of PIV to obtain velocity data inside the wheelhouse. Table 5.1 presents the details of the modified Fabijanic geometry and a detailed explanation on the experimental setup can be found in [28]

Table 5.1: Modification made to the standard Fabijanic body (refer table 4.1) in the experimental model

| | Fabijanic Body | Modified Fabijanic Body |
|---|---|---|
| $R_{wh}$ | $52.3mm$ | $61.5mm$ |
| r | $38.3mm$ | $45mm$ |
| D1 | $36.2mm$ | $40mm$ |
| D2 | $50.5mm$ | $56mm$ |

The radius of the wheel and wheelhouse was changed in the numerical model to match the experimental, while the depth of the wheel and wheelhouse (D1 and D2) were unchanged. This was done to minimize the changes that needed to be made to the blocking strategy used with ICEM CFD. Given that the variation of the above mentioned dimensions between experimental and numerical model is only 10 %, the consequent effect on the flow field is expected to be minimal. Similar to the $Re_{1W}$ case, Large Eddy Simulation with the WALE subgrid viscosity model was used to obtain the numerical solution at a Reynolds number of 9 x $10^3$. The stationary wall boundary condition was used on the road, as mentioned in Chapter 4, to match the experimental conditions.

The comparison between experimental and numerical results will be presented in the next section. The results from the experiment will be referred to as **PIV** and results from the simulation as **LES** in this chapter.

## 5.2 Comparison with PIV Results

To validate the numerical simulation, both a qualitative and a quantitative comparison is made with the experimental results. Contours of mean velocity magnitude obtained from both planar and stereo PIV are used for the qualitative comparison, while a direct comparison between the various quantities along a line is used to make a quantitative comparison.

### 5.2.1 Qualitative Comparison

Three planes were considered for comparing the flow field (refer figure 5.1): (1) A plane coinciding with the centre of the wheel and parallel to the streamwise direction (Plane 1) (2) A plane at a distance of 1.5cm from the side of the wheel and parallel to the streamwise direction (Plane 2) and (3) a plane at a distance of 1.5D behind the wheel (D is the diameter of the wheel) and perpendicular to the streamwise direction (Plane 3). The schematic shown in the figure is based on the half-model used in the experiments. It should be noted that the orientation of the vehicle with respect to the incoming flow was different in the simulation i.e. when viewed from the front, the location of the wheel and wheelhouse is on the right side, with the symmetry plane on the left.

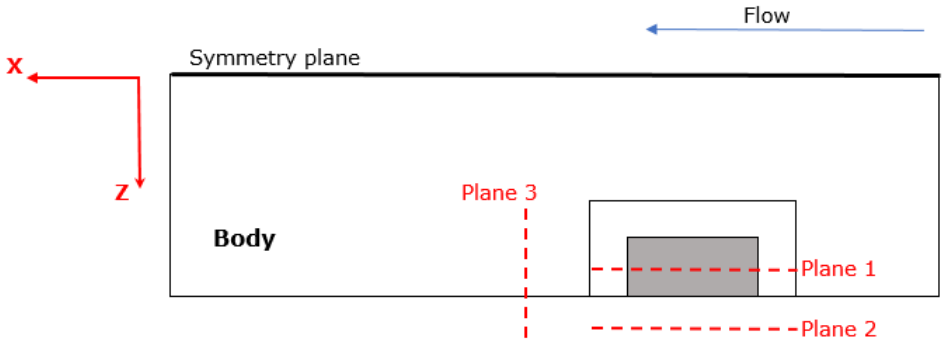


Figure 5.1: Schematic of the vehicle model used in the experiment, when viewed from the top. The location of planes where a qualitative comparison will be made are shown in this schematic. It should be noted that the orientation of the vehicle with respect to the incoming flow is different in the numerical simualtion, as explained in the text.

The velocity magnitude, normalized by the free stream velocity, in the planes under consideration were compared to verify the validity of the numerical solution. The experimental results in Planes 1 and 2 were obtained using planar PIV, while stereo PIV was used for Plane 3. The observations of the qualitative comparison can be summarized as follows:

1. The comparison of the velocity magnitude in Plane 1 shows a good agreement between the results from LES and PIV as shown in figure 5.2. The red box in the figure marks the H vortex, which has been identified using both techniques.

2. The comparison of the velocity magnitude in Plane 2 between LES and PIV is shown in figure 5.3. While the near ground contours show a very good agreement, the magnitude of velocity along the side of the vehicle body (marked by red ellipse in figure 5.3a) is found to be higher in LES than in PIV.

3. The comparison of the velocity magnitude in Plane 3 between LES and PIV is shown in figure 5.4. The vortex in the wake of the wheel which is the L vortex, can be observed in both LES and PIV. The rotation of the L vortex is consistent with the orientation of the vehicle with respect to the incoming flow.

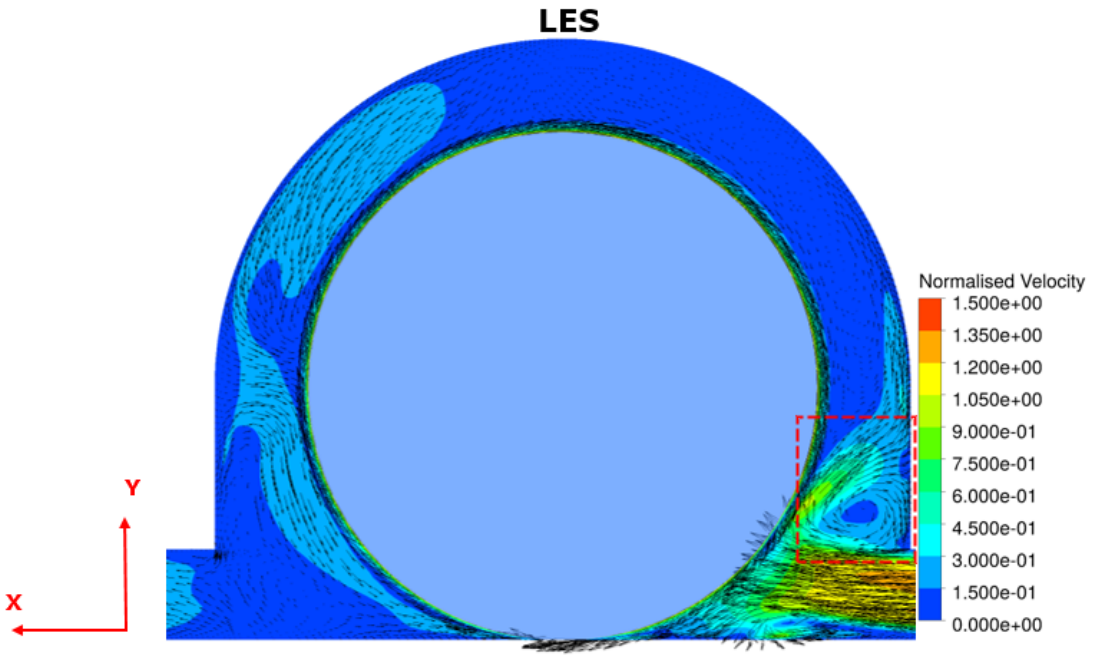


(a)

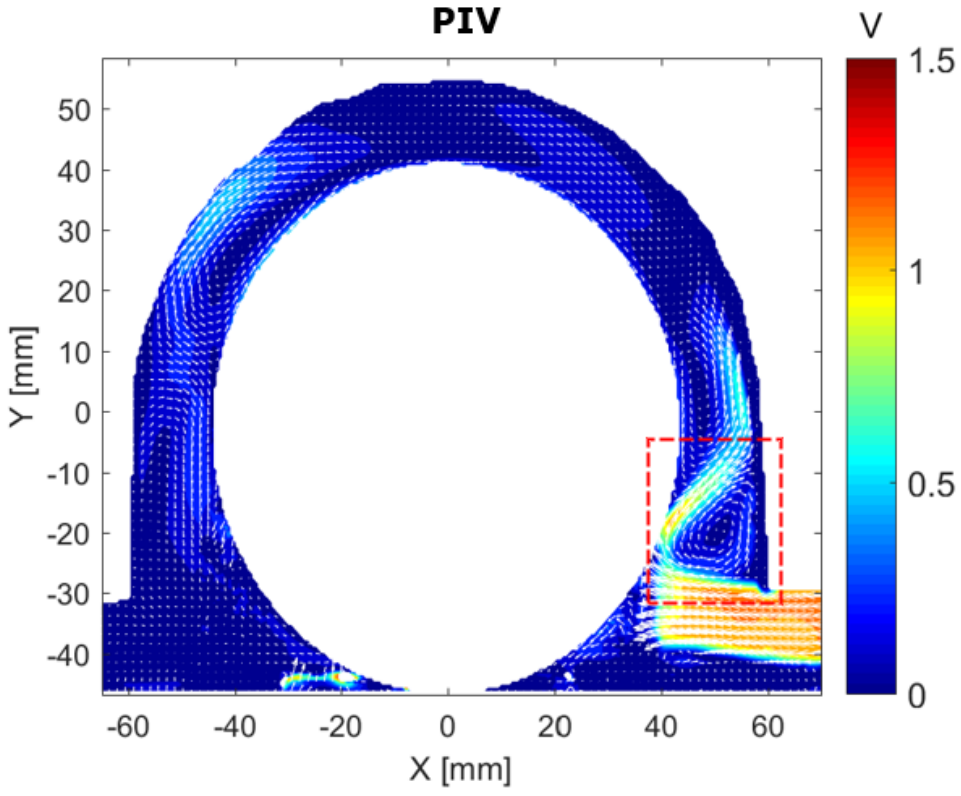


(b)

Figure 5.2: Contours of velocity, normalized by the free stream velocity in Plane 1, along with planar velocity vectors. The presence of H vortex, marked by the red box, can be observed in the results of both LES and PIV. An overall agreement in the magnitude of velocity can also be observed. Flow is from right to left.

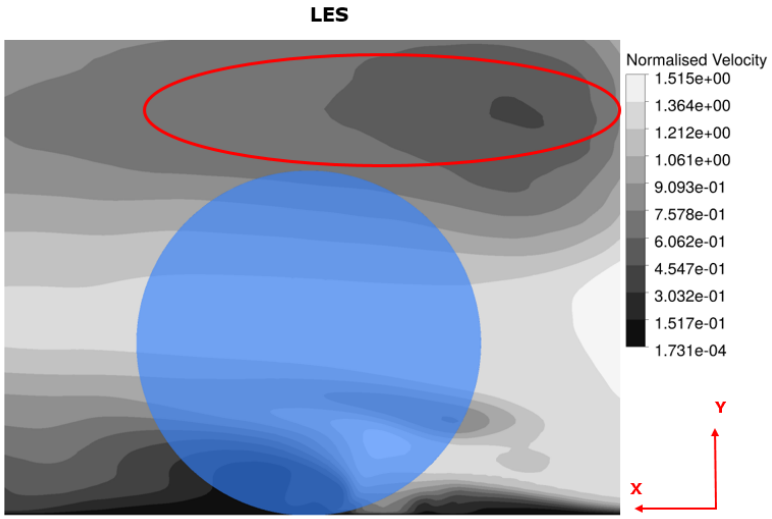


(a)

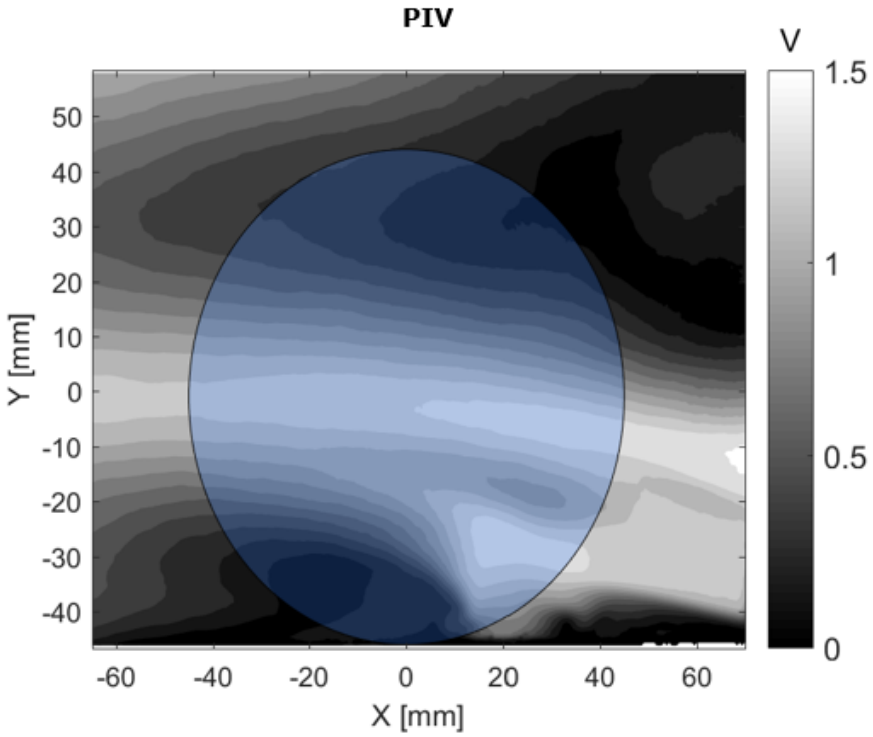


(b)

Figure 5.3: Contours of velocity, normalized by the free stream velocity in Plane 2. The near ground contours of normalized velocity are in good agreement between the results of LES and PIV. The contours, however, show that the velocity on the side of the body (marked by the red ellipse) higher in the results of LES when compared to PIV. Flow is from right to left. It should be noted black contours represent low velocities and white represents high velocities.

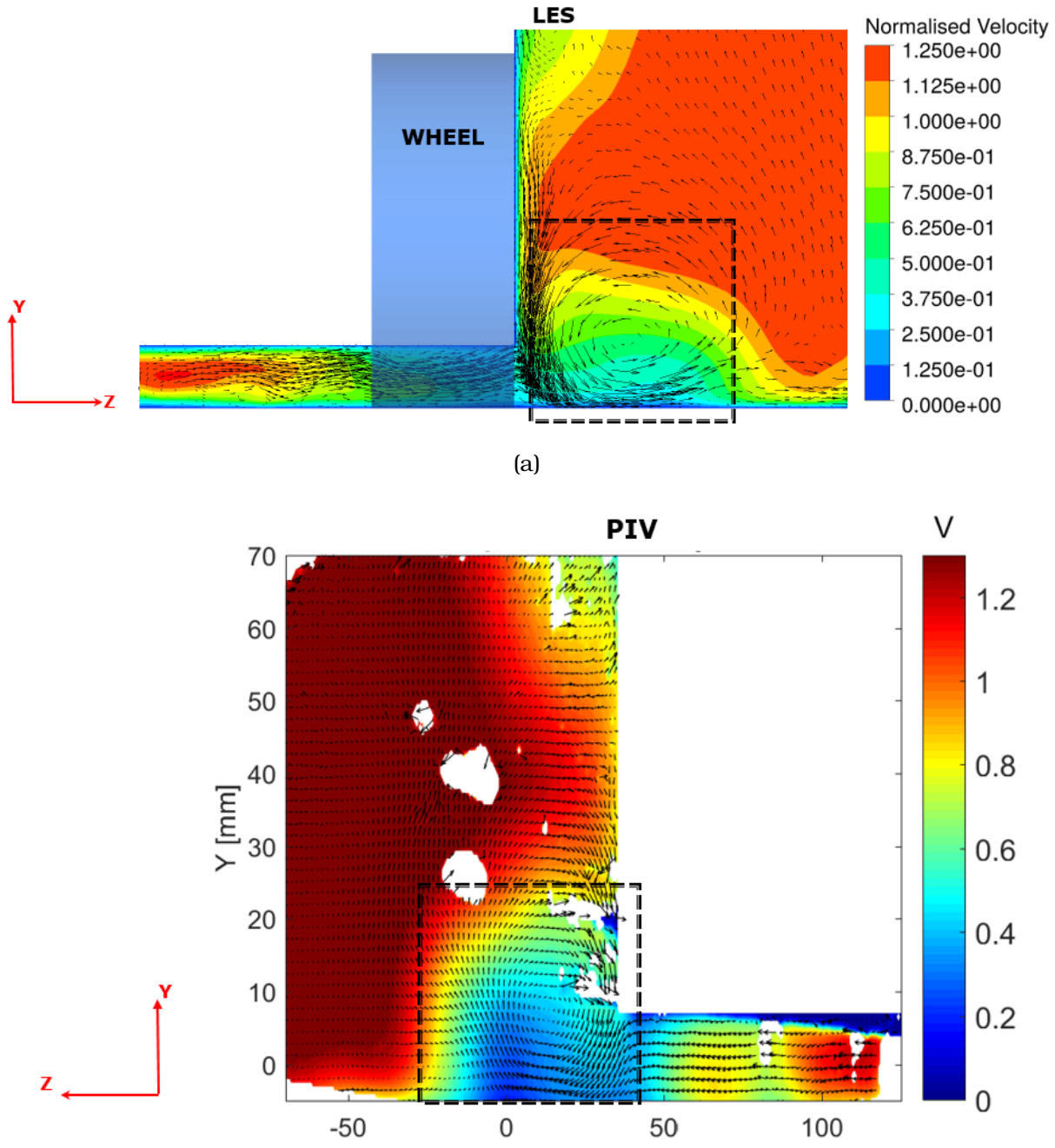


Figure 5.4: Comparison of the contours of normalized velocity magnitude superimposed with planar velocity vectors, between LES and stereo PIV, in plane 3 is shown here. The black box marks the location of the L vortex. The sense of rotation of the L vortex is found to be consistent with the orientation of the vehicle with respect to the incoming flow. Flow is into the plane. It should be noted that the white gaps in (b) represent the region that was masked from calculation, due to reflections observed during the experiment.

### 5.2.2 Quantitative Comparison

The quantitative comparison between LES and PIV is made along a line inside the wheelhouse as shown in the schematic in figure 5.5. The comparison is made between both mean and turbulent quantities. The streamwise component of velocity (U) and the velocity magnitude(**V**) are the mean quantities considered for comparison (refer figure 5.6). The turbulent quantities include the RMS of velocity fluctuations (u' and v') and the turbulent shear stress ($\overline{U'V'}$) (refer figure 5.7).

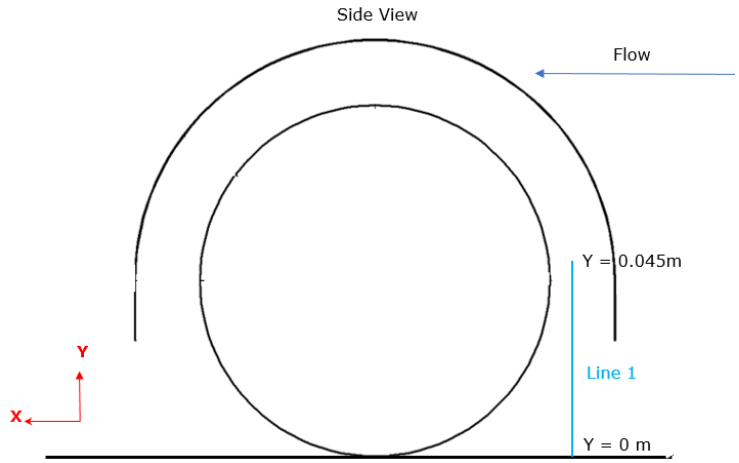


Figure 5.5: Schematic of the wheel inside the wheelhouse, showing the location of line along which the quantitative comparison is made. The line is located along a plane, coinciding with the centre of the wheel.

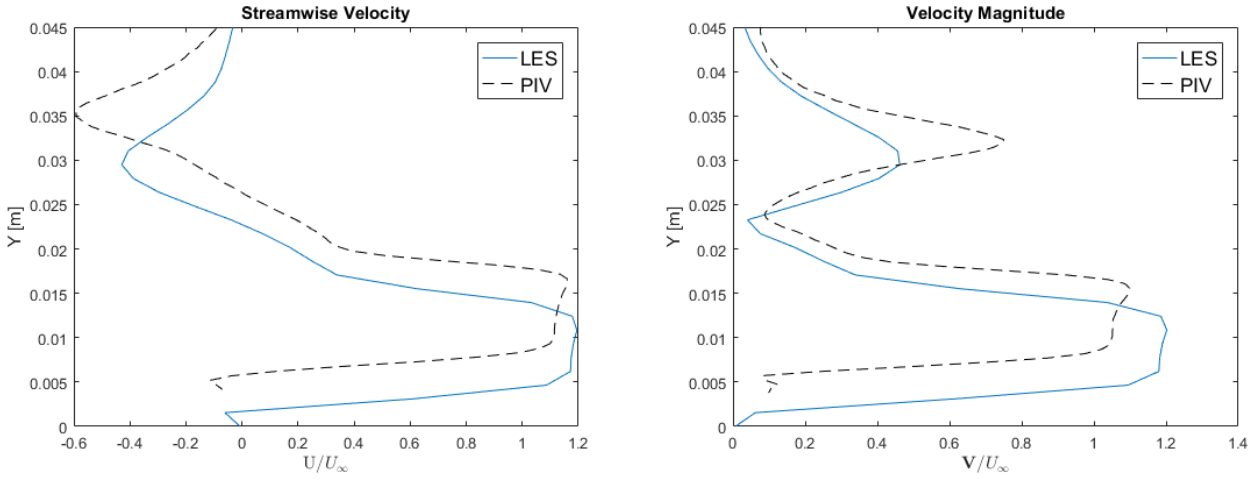


(a) (b)

Figure 5.6: Comparison of the mean quantities between LES and PIV along Line 1 is shown here. (a) Streamwise component of velocity, normalized by free stream velocity. (b) Magnitude of velocity normalized by the free stream velocity. The quality of the PIV data close to the ground (until Y = 0.005m) is compromised by reflections and hence not shown in the plot.

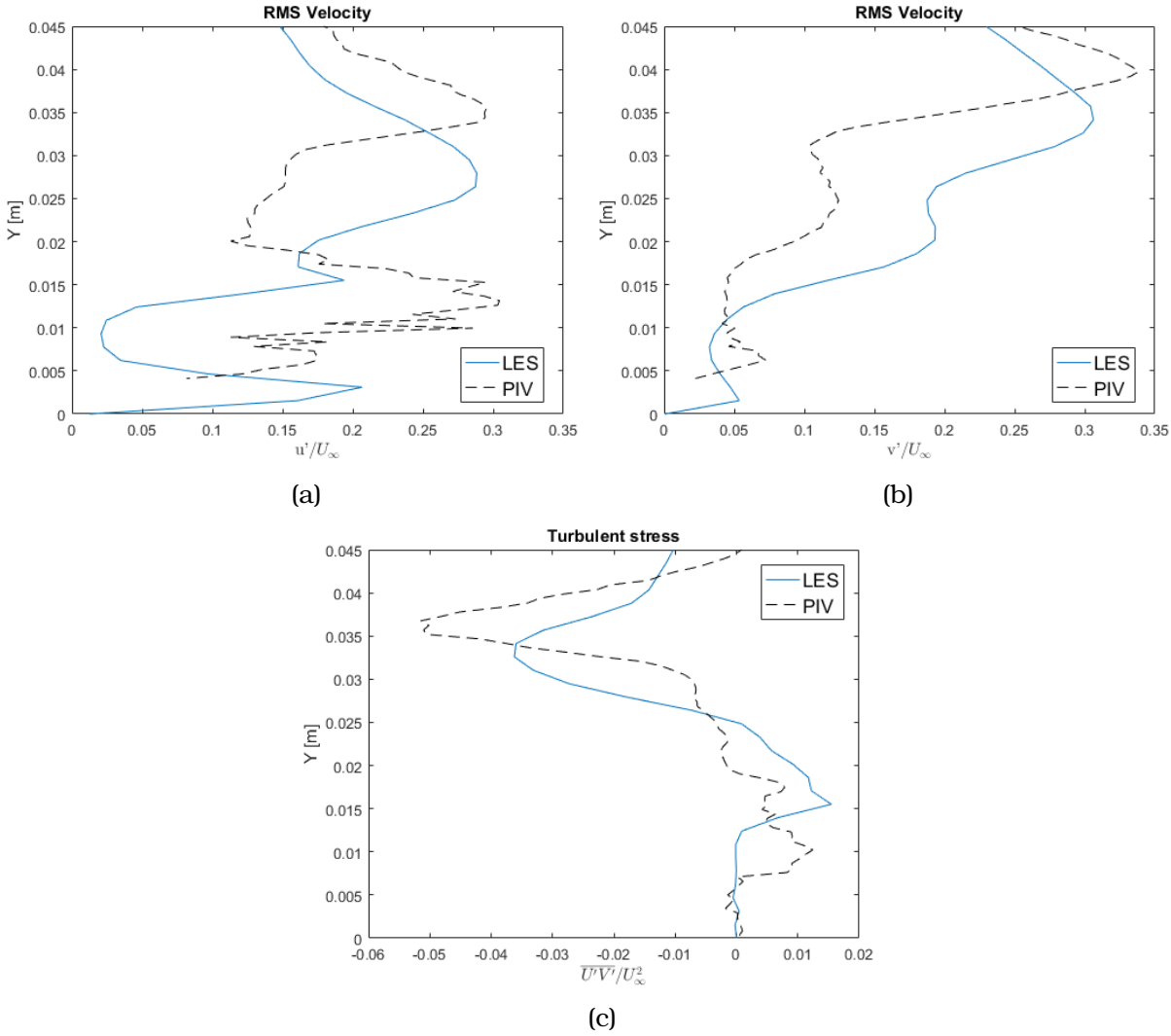


Figure 5.7: Comparison of the turbulent quantities between LES and PIV along Line 1 is shown here. (a)RMS of the fluctuations of velocity (horizontal component) normalized by free stream velocity. (b)RMS of the fluctuations of velocity (vertical component) normalized by free stream velocity. (c) Turbulent shear stress ($\overline{U'V'}$), normalized by the square of free stream velocity. The values close to the road are not plotted for the PIV data as explained in figure 5.6.

The comparison of the mean quantities shows that a good agreement exists between the velocity profiles of LES and PIV. When comparing the turbulent quantities, a good level of agreement in the profiles of v' (velocity fluctuations of vertical component) and turbulent shear stress ($\overline{U'V'}$) is observed (refer figures 5.7b and 5.7c). But the experiment predicts a higher level of streamwise velocity fluctuations, in the gap between the underbody and ground (refer figure 5.7a), when compared to LES.

Looking at the profiles of the mean velocity (figure 5.6), a constant offset between the curves obtained from LES and PIV can be observed, despite the good agreement between the profiles. The reason for this observed offset and the mismatch in the streamwise fluctuations of velocity between LES and PIV are still under investigation.

## 5.3 Conclusions

The level of qualitative and quantitative agreement (in the mean quantities) with the experimental result points to an LES that is sufficiently resolved. In addition, the low contribution of the subgrid stress to the total turbulent shear stress (figure 5.8) in the numerical simulation further increases the confidence of the results obtained in the present work.

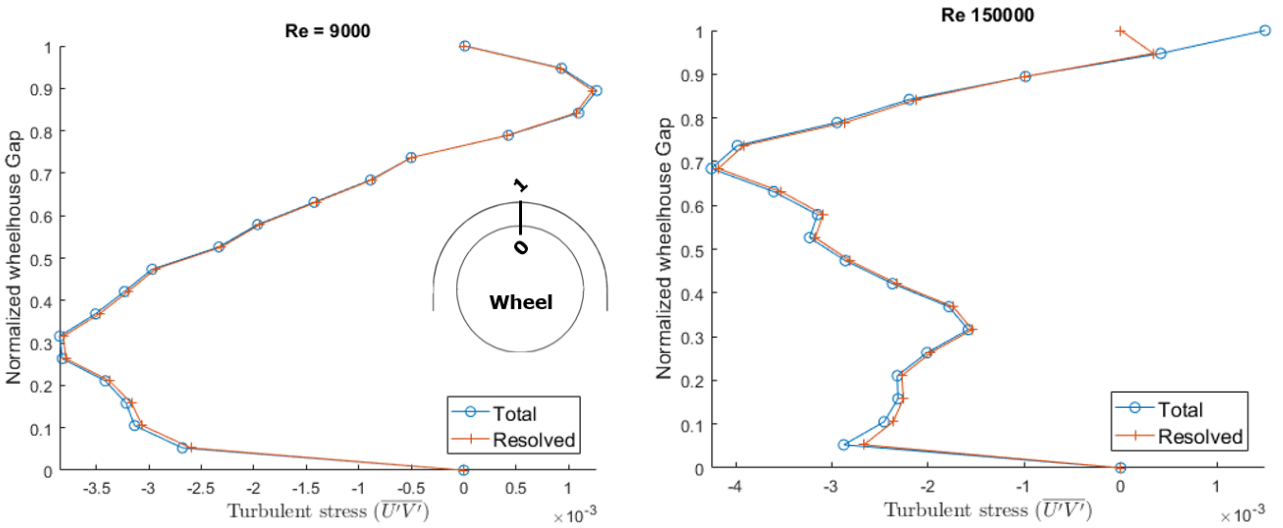


(a) (b)

Figure 5.8: Comparison of the contribution of subgrid model to the total turbulent stress ($\overline{U'V'}$) along a line as indicated in the inset. (a) Results at a Reynolds number of 9 x $10^3$ using the WALE model. (b) Results at a Reynolds number of 150 x $10^3$ using the Smagorinsky model.

# Chapter 6

# Results Part II -Reynolds Number Dependence

The results for varying the Reynolds number (*Run 1* refer table 4.2) to find its influence on the flow field is discussed in this chapter. A comparison of the force coefficients, pressure distribution and the flow field will be used to establish the qualitative independence of flow with respect to the Reynolds numbers considered in this research.

## 6.1 The Force Coefficients ($C_D$ and $C_L$)

The first set of quantities that will be considered for comparison is the force coefficients, namely the drag and lift coefficient, of the wheel. The comparison between the force coefficients for the different cases is shown in figure 6.1. The experimental value [8] obtained at a Reynolds number of 1.5 x $10^5$ is also shown in the figures. Both the drag and lift coefficients are calculated based on the front exposed surface area of the vehicle [1]. The use of frontal surface area for both drag and lift was done to ensure consistency with the values obtained from the experiment.

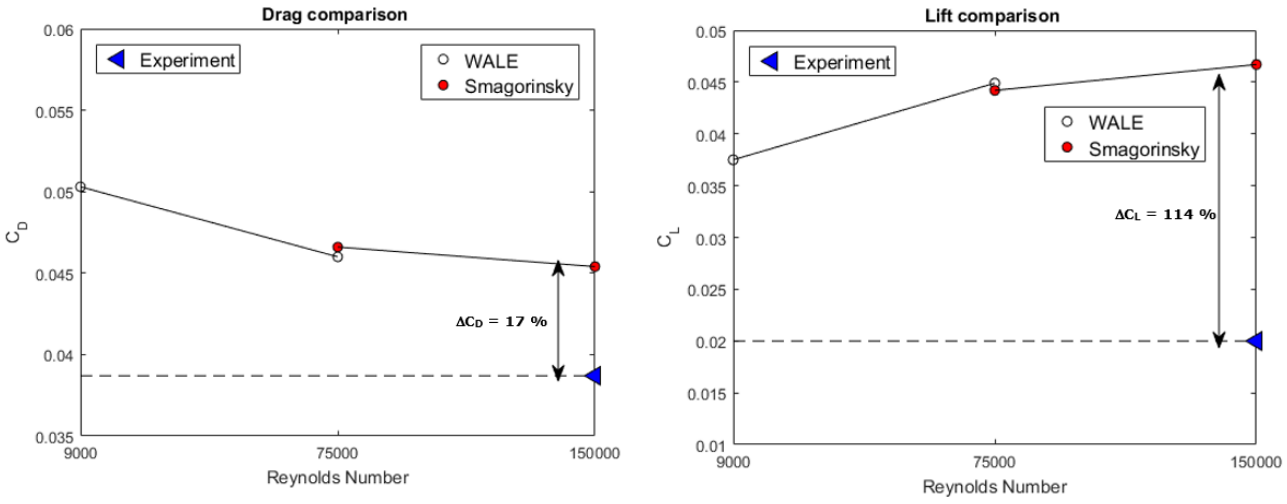


(a) (b)

Figure 6.1: (a) The variation of the (a) Drag coefficient and (b) Lift coefficient of the wheel as a function of Reynolds number. The experimental values obtained at Re = 1.5 x $10^5$ by Fabijanic [8] are used as a reference for comparison.

[1]The frontal surface area that is exposed to the oncoming flow. It is calculated by projecting the vehicle body with the wheel onto the front plane. It should be noted that, though a half-model is used, the surface area of the total vehicle is considered for force coefficients, to ensure a consistent comparison with the experiment. Unless stated otherwise, the force coefficients presented in this thesis are based on the above mentioned reference area.

**Observations on variation of force with Reynolds number**

- The difference between the drag coefficients at the highest and lowest Reynolds number considered is 0.0049 which corresponds to a 9 % variation.
- The difference between the lift coefficients at the highest and lowest Reynolds number considered is 0.0092 which corresponds to a 25 % variation.
- A small but visible dependence of the subgrid model is observed on the values of both drag and lift coefficients at Re = 75000.

**Comparison with the experimental values**

- The drag coefficient of the wheel is higher by 17 % with respect to the experimental value in the present simulation. The difference in value is within the limits of uncertainty in the measurement of force in the experiment.
- The lift coefficient of the wheel is higher by 114 % with respect to the experimental values. A similar increase in lift coefficient was observed in URANS calculations as well ([2] and refer Appendix D). The higher lift coefficient estimated in the numerical simulation could be attributed to one of the following two reasons: (1) The absence of wheel mount effect in the numerical simulation (2) The increase in uncertainty in lift force measurement in the experiment could also be due to an uncertainty in a proper ground contact [2]

The drag coefficient of the wheel is observed to vary very little with Reynolds numbers. While a strong dependence is indeed observed in the lift coefficient, the percentage contribution of the force (both drag and lift) acting on the wheel on the total force was found to be similar for all cases (6 - 9 % for drag coefficient and 12-17 % for lift coefficient). In other words, the relative contribution of wheel to the total drag and lift coefficient of the vehicle is found to be similar across all Reynolds numbers.

## 6.2 Sectional Force Coefficients

**Definition**

*The sectional force coefficient is defined as the force obtained by integrating the coefficient of pressure along a specific section of the wheel/wheelhouse, normalized by a reference length.*

The definition of sections of wheel and wheelhouse is given in figure 6.2. A total of 5 sections for the wheel (refer figure 6.2a) and 6 sections for the wheel house (figure 6.2b) are considered. The coefficient of pressure along the various sections can be integrated to obtain a force coefficient (drag and lift coefficient) as follows :

$$C_d = \frac{w}{A_{\text{ref}}} \int_0^{2\pi} C_p r cos(\theta) d\theta \tag{6.1}$$

$$C_l = \frac{w}{A_{\text{ref}}} \int_0^{2\pi} C_p r sin(\theta) d\theta \tag{6.2}$$

where $r$ is the radius of the wheel/wheelhouse and $w$ is the width of wheel/wheelhouse and $A_{ref}$ is the frontal surface area used to calculate the drag/lift coefficients in the previous section. The choice of the reference length scale ($w/A_{ref}$), ensured a consistent comparison between the sectional force coefficients and the mean force coefficients. Note that the range of integral becomes $0 \rightarrow \pi$ when considering the sectional coefficients of wheelhouse.

[2] Obtained from a private discussion with Fabijanic(author of [8]).

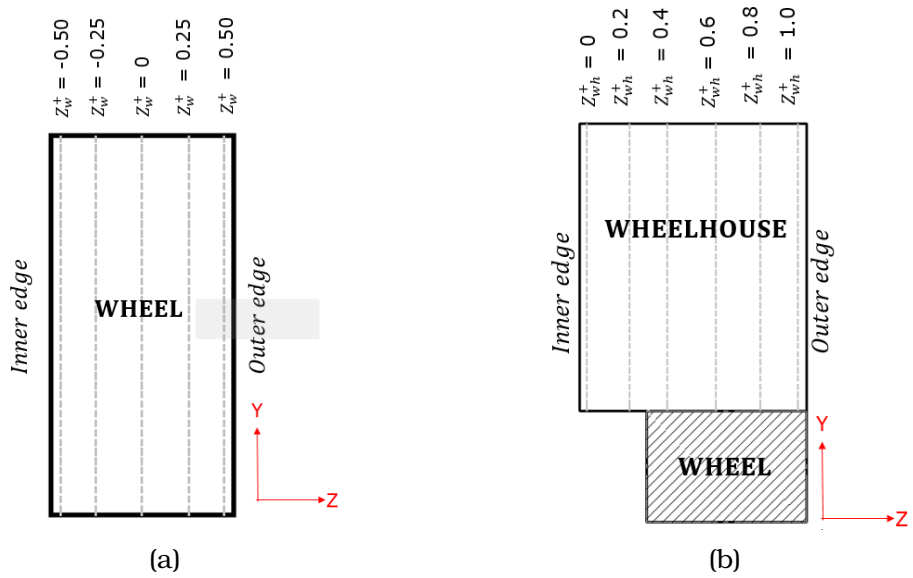


Figure 6.2: The definition of sections for the wheel and wheelhouse. A relative dimension is used to locate a particular position along the wheel or wheelhouse. For the wheel ($Z_w^+$), the locations are calculated based on the relative position with respect to the wheel center, whereas for wheelhouse ($Z_{wh}^+$), they are calculated with respect to the inner edge.

### Sectional coefficients of Wheel

Figure 6.3 shows sectional force coefficients as a function of the spanwise location along the wheel. The spanwise location ($Z_w^+$) has been normalized based on the relative position on the wheel with respect to its mid section. For example, $Z_w^+ = 0$ refers to the mid section of the wheel (refer figure 6.2a). The force coefficients, drag and lift, presented in the plot are normalized based on the mean drag/lift coefficient of wheel for the respective Reynolds numbers ($C_d^+/C_l^+$). This is done to ensure that a qualitative comparison can be made across all the Reynolds numbers.

### Observations

- The maximum contribution to the drag/lift coefficient of the wheel is observed at the mid-section ($Z_w^+$=0) of the wheel, while the contribution decreases towards the outer edges of the wheel ($Z_w^+ = 0.5$ and $Z_w^+ = -0.5$).
- At Re = 9000, the force distribution is found to be more symmetric than that at higher Reynolds numbers.
- The sectional drag coefficient is found to be more dependent on the Reynolds number near the edge of the wheel ($Z_w^+ = 0.5$ and $Z_w^+ = -0.5$).

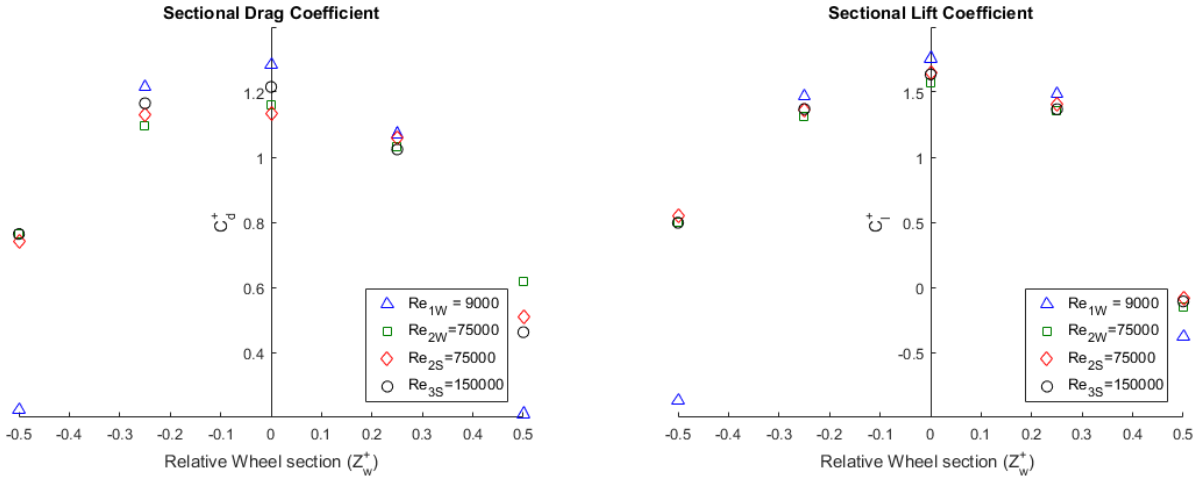


(a) (b)

Figure 6.3: The sectional force coefficients of the wheel, (a) sectional drag coefficient and (b) sectional lift coefficient, are presented for different Reynolds numbers. The coefficients are normalised by the value of mean drag/lift coefficient of the respective Reynolds numbers.

While the mid span shows a very good level of agreement of drag and lift values across the Reynolds numbers, there is a visible amount of spread in values of drag and lift at the outer edges. To explain this, consider the pressure distribution across different sections of the wheel as shown in figure 6.4. Along the center of the wheel, the pressure distribution shows that, for all Reynolds number, the location of separation point (110°) (refer Appendix B), the location of stagnation point (60°) and the base pressure[3] value ($C_p$ = -0.5) are in good agreement with each other (refer figure 6.4a). This is reflected in the sectional force coefficients corresponding to the mid-section ($Z_w^+ = 0$ in figure 6.3).

The pressure distribution along the edges of the wheel shows considerable difference between the $Re_{1W}$ and the other cases. The main difference is the magnitude of pressure at an angle of 60°, which is inline with the stagnation point. It can be seen that at higher Reynolds numbers ($Re_{2W}$,$Re_{2S}$,$Re_{3S}$), the $C_p$ reaches a value close to one, which indicates stagnation conditions (figure 6.4b and 6.4c). The variation in pressure at this location explains the spread in values of drag observed at the edges. Similarly, the difference in value of the base pressure is responsible for the observed variation on lift coefficient.

Even though the magnitude of pressure coefficient and hence the sectional force coefficient along the edges of the wheel shows a considerable difference between the low Reynolds number $Re_{1W}$ and the higher Reynolds numbers($Re_{2W}$,$Re_{2S}$,$Re_{3S}$), a qualitative similarity in the pressure distribution and hence the sectional force coefficient distribution can be observed.

[3]The base pressure coefficient is defined by the constant value of the $C_p$ on the surface of the wheel post separation

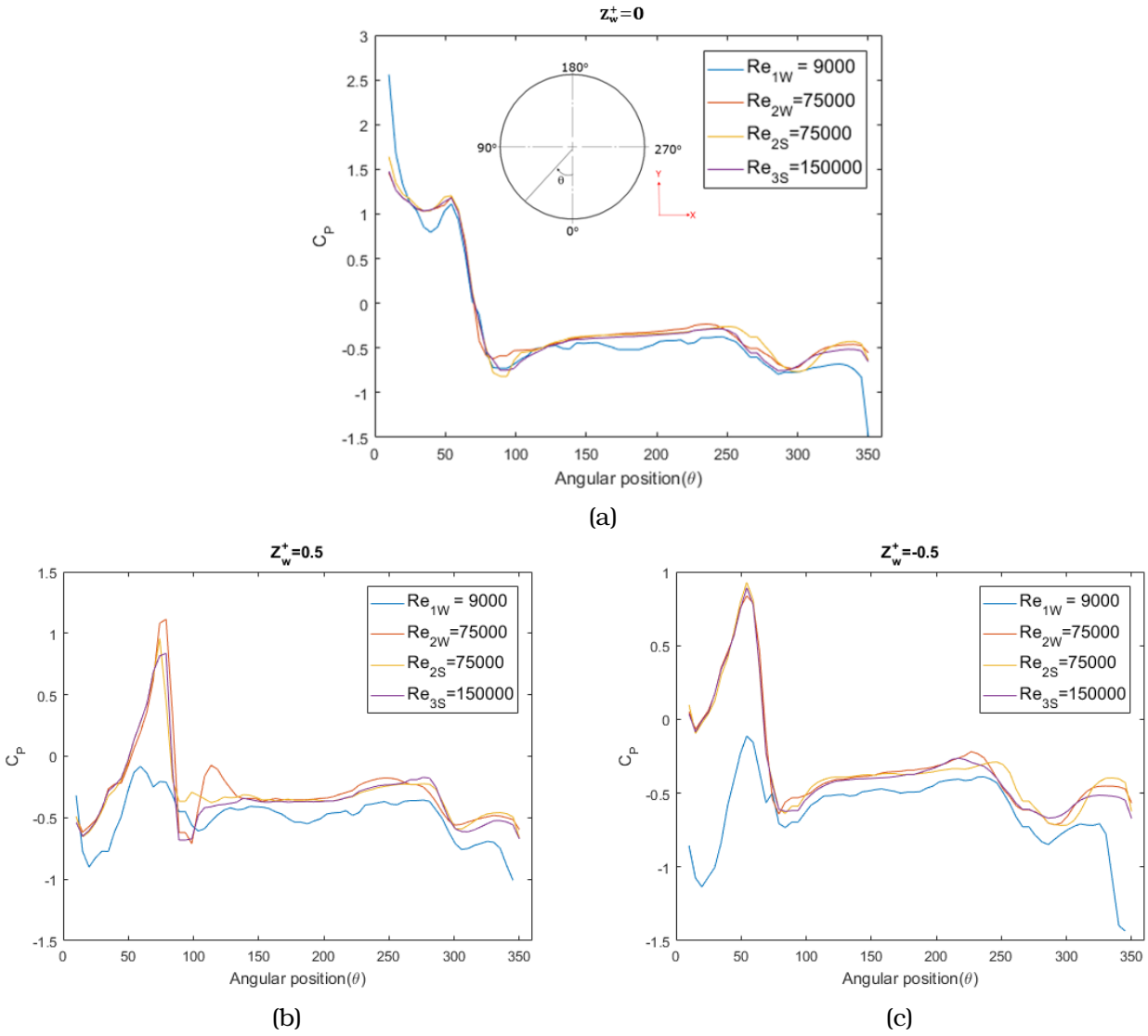


Figure 6.4: The $C_p$ curve along the surface of the wheel for three different sections are shown. (a) Center line (b) outer edge (c) inner edge of the wheel. The definition of angular location is shown in image (a) for clarity.

### Sectional coefficients of Wheelhouse

Figure 6.5 shows the distribution of force coefficient as a function of the spanwise location on the wheelhouse. The spanwise location ($Z^+_{wh}$), in this case, has been normalized based on the relative position on the wheelhouse with respect to the inner edge. For example, $Z^+_{wh} = 0$ refers to the inner edge of the wheelhouse (refer figure 6.2b). The force coefficients are normalized based on the values at the outer edge of the wheel house. The normalized drag/lift coefficients ($C^+_d$ /$C^+_l$) ensures that a qualitative comparison of the relative distribution of the sectional force coefficients (with respect to the values along the outer edge) is made, between different the Reynolds numbers.

### Observations

- The drag coefficient shows positive values in the inner region of the wheelhouse ($Z^+_{wh} = 0$) and decreases on approaching the outer edge. Negative value of drag can be interpreted as a force acting against the direction of incoming flow (i.e. thrust force).
- The outer edge is found to produce the maximum downforce (i.e. negative lift), while the lift increases approaching the inner edge.
- The magnitude of the force coefficients show a considerable dependence on the Reynolds number.

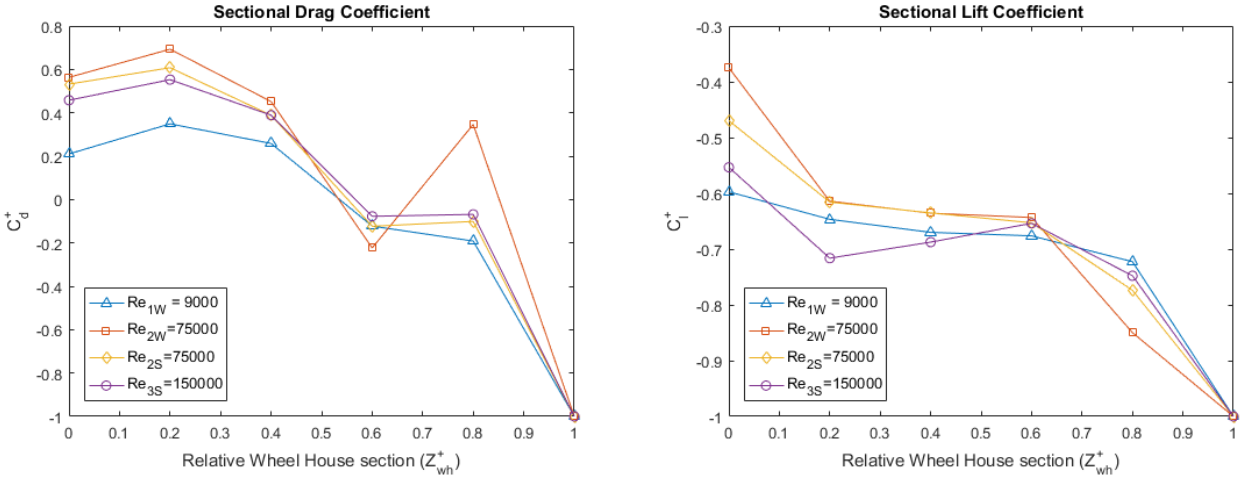


(a) (b)

Figure 6.5: The sectional force coefficients of the wheelhouse, (a) sectional drag coefficient and (b) sectional lift coefficient, are presented for different Reynolds numbers. The coefficients are normalized by the value on the outer edge of the wheelhouse.

The above observed difference in the magnitude of force can be explained by looking at the pressure distribution along different sections. Two sections corresponding to $Z^+_{wh} = 0$ and $Z^+_{wh} = 0.4$ are shown in figure 6.6, which will be used to explain the above observation. The $C_p$ curve is divided into three segments: region I from 0°to 30°; region II from 30°to 160°; region III from 160°to 180°(shown in figure 6.6a).

The general trend that is observed is that high pressures in Region I results in a lower drag coefficient. It can be expected that lower pressures in Region III can also lead to decreased drag coefficient. But in the present case, the difference in values of pressure in Region I is found to be more influential than the differences observed in Region III. Hence, the magnitude of pressure in Region I governs the trend in sectional drag coefficient, observed in figure 6.5a. Similarly, the magnitude of pressure in Region II is reflected in the sectional lift coefficients shown in figure 6.5b.

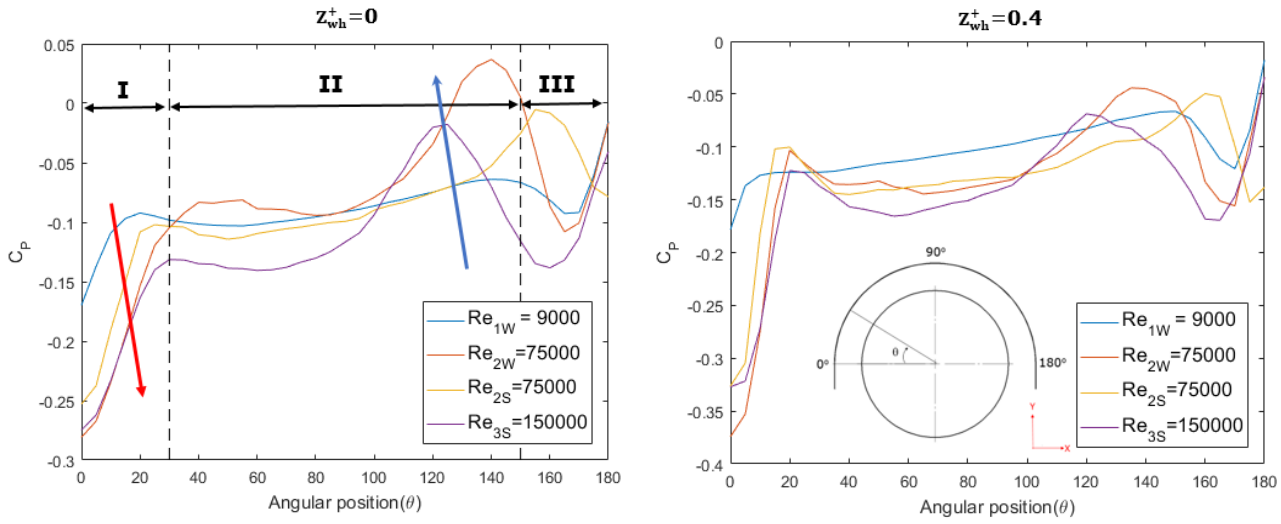


Figure 6.6: The $C_p$ curve along the surface of the wheelhouse for two different sections are shown in (a) $Z^+_{wh} = 0$ and (b) $Z^+_{wh} = 0.4$. The definition of angular location is shown in image (a) for clarity. The red arrow represents the variation of drag coefficient (figure 6.5a) and blue arrow represents variation of lift coefficient (figure 6.5b) at $Z^+_{wh} = 0$

The conclusive reason for the dependence of the pressure coefficient, along the wheelhouse sections, on the Reynolds number could not be identified. While it is true that the magnitude of the pressure coefficient and hence the sectional force coefficient, showed a considerable dependence on the Reynolds number, a qualitative similarity in the distribution is observed. Take, for instance, the sectional drag coefficient distribution shown in figure 6.5a. For all the Reynolds numbers, it can be observed that: (1) a maximum thrust (negative drag coefficient) is observed along the outer edge. (2) an increase in value of the sectional drag coefficient is observed moving towards the inner edge of the wheelhouse (until $Z^+_{wh} = 0.2$)[4] (3) a drop in value of sectional drag coefficient at the inner edge of the wheelhouse ($Z^+_{wh} = 0$).

Such a similarity could be observed in the distribution of sectional lift coefficient as well, with the maximum downforce (negative lift) produced along the outer edge ($Z^+_{wh} = 1$) and maximum lift produced along the inner edge of the wheelhouse ($Z^+_{wh} = 0$). Thus, while a difference in magnitude of the pressure coefficient along the wheelhouse was observed, the relative distribution of the same was found to be similar across all the Reynolds numbers. The qualitative similarity in pressure distribution could point to a similarity in flow field across all the Reynolds numbers which will be discussed in the following section.

[4]The anomalous behaviour of $Re_{2W}$ could be attributed to the effect of sub-grid model

## 6.3 Flow Topology Comparison

In the previous section, a comparison of force and pressure distribution across all Reynolds numbers was made. To further corroborate the qualitative similarity observed in the previous section and conclusively state that the flow at low Reynolds number is similar to one at realistic road conditions (high Reynolds number), a comparison of the flow topology is presented in this section. Presence of the major structures presented in Chapter 2, irrespective of the Reynolds number will point to the qualitative independence of flow on the Reynolds number.

The figures 6.7, 6.8, 6.9 and 6.10 shows the comparison of the flow topology for the various cases considered in the present work. The general behaviour of the flow is best represented by 3D stream-ribbons shown in figure 6.8 and figure 6.9. The streamribbons were generated by choosing an ideal seeding line that best represents the major features of the flow field. All the flow features discussed in Chapter 2 can be observed across all the Reynolds numbers. It should be noted that the C vortex is not clearly visible in the $Re_{1W}$ case using streamlines. But the presence of C was verified using other means of visualization - iso-surface of mean pressure coefficient (refer figure 6.9). The following observations, based on the comparison of flow topology, can be made:

- The behaviour of A vortex shows a low level of dependence on the Reynolds number. The trajectory A vortex in cases $Re_{1W}$ and $Re_{3S}$ is found to reverse locally before exiting the wheelhouse cavity, the same cannot be observed in the other two cases (refer dashed lines in figure 6.9). The flow reversal mentioned above is marked as $A'$ in the figure 6.7a.

- The exit location of B vortex is found to be different in the present work. Previously the B vortex was found to exit the wheelhouse cavity from the side [2] [5], whereas in the present work, the stream ribbons shows that the flow exits from the bottom (refer figure 6.8).

- The E vortex, which was previously described in [5] as a tip vortex, is found to be an extension of the H vortex. This was determined by looking at the sense of rotation of the E vortex which was found to be the same as that of the H vortex (refer figure 2.2b in Chapter 2). This rotational direction is opposite to the one that would be expected of a tip vortex.

Figure 6.9 shows the visualization of the above mentioned structures using iso surface of low pressure. The iso-surfaces are colored by the velocity magnitude, normalized by the free stream velocity in the respective cases. The similarity in the values of the normalised velocity shows that the flow features scale with the free stream velocity without a drastic change in their behaviour. The above sentence can be interpreted as follows : Any change in behaviour of flow at a low Reynolds number due to a change in, say geometry, could potentially be observed at a high Reynolds number as well.

## 6.4 Conclusion

Part II of the results section was focused on investigating the effect of changing the Reynolds number on flow over wheel in a wheelhouse. To summarize the observations so far :

1. The centre line pressure distribution on the wheel surface showed a good level of agreement across all the Reynolds numbers.
2. In the edges of the wheel, a difference in the magnitude of pressure could be observed between the Reynolds numbers. Nevertheless, a good qualitative agreement in the distribution of pressure on the wheel surface across all the Reynolds numbers was observed.
3. The pressure distribution on the surface of the wheelhouse showed a dependence on the Reynolds number. However, the normalized sectional force coefficients showed similar behaviour across all the the Reynolds numbers.
4. The description of the flow field in the wheelhouse region was found to be similar across all the Reynolds number. All the major structures discussed in Chapter 2 was found to be present, irrespective of the Reynolds number.

Thus, while a quantitative dependence of the pressure distribution on the Reynolds number was observed, the variation of pressure on the surface of the wheel and wheelhouse showed a qualitative similarity. Combining this with the similarity in flow topology, it can be concluded, for the Reynolds numbers considered, that the flow over a rotating wheel in a simplified wheelhouse is qualitatively independent of the Reynolds number.

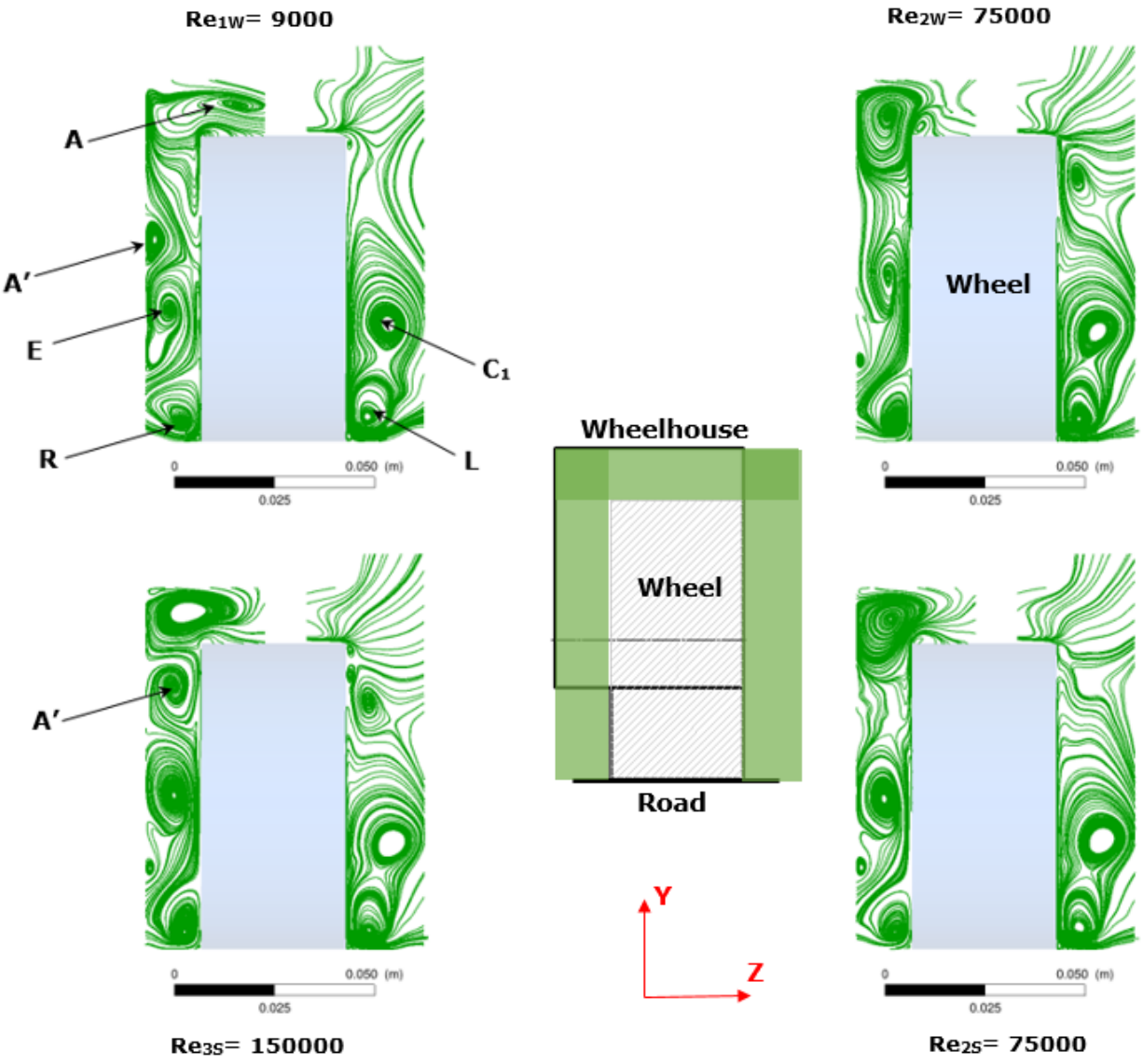


(a)

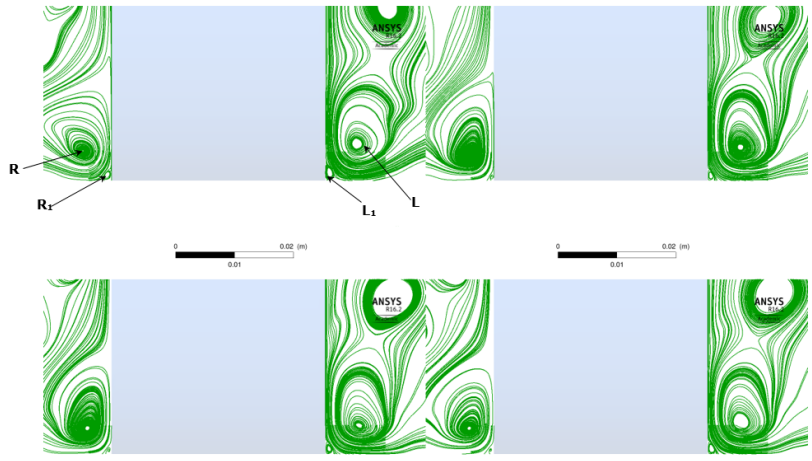


(b)

Figure 6.7: Comparison of the time-averaged streamlines projected on a the plane coinciding with the centre of the wheel, and normal to the flow direction (Front View ).(b) A close up of the jetting vortices near the road, to visualize the counter rotating vortex pair that was first identified by Krajnovic [5].

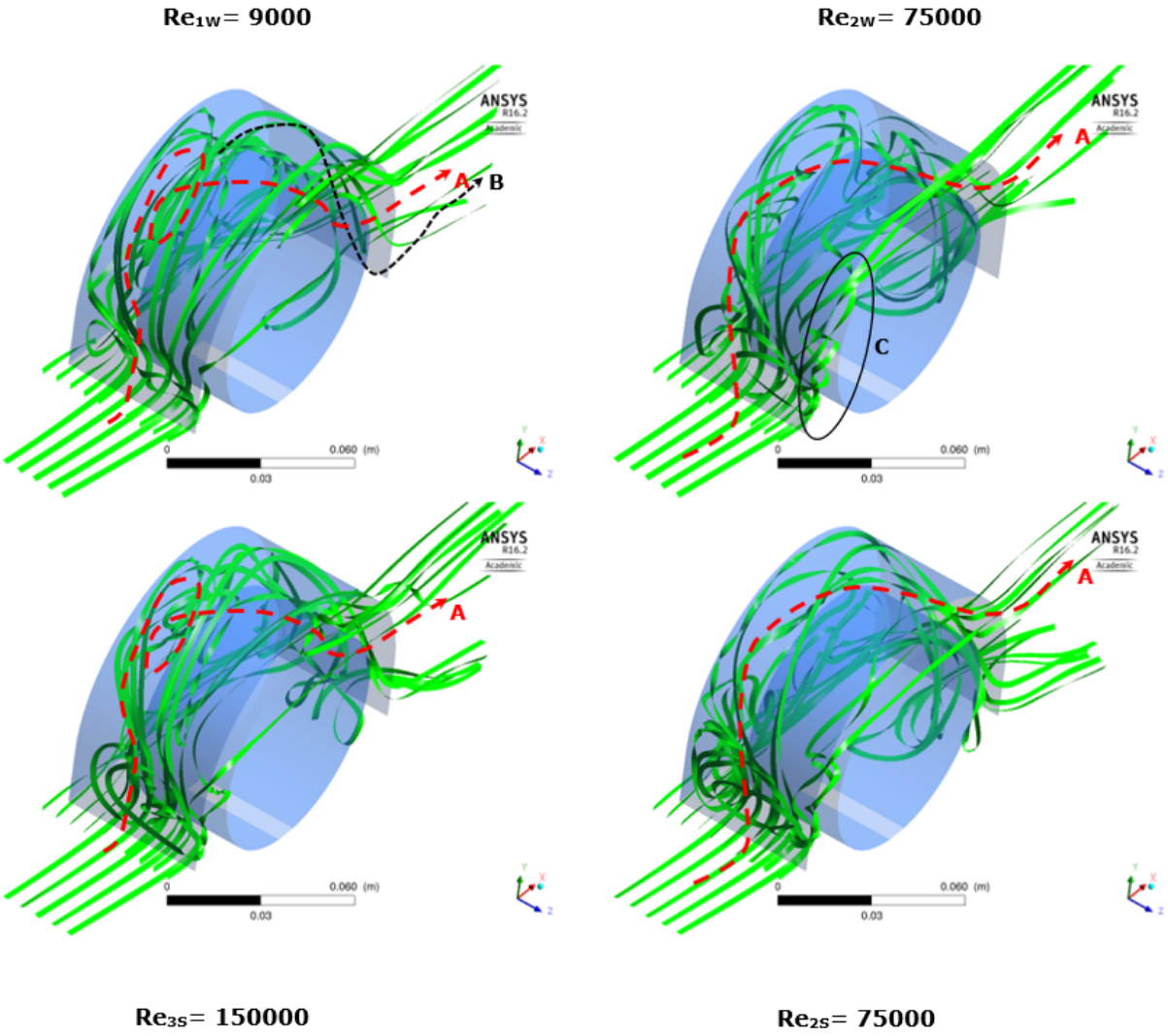


Figure 6.8: Comparison of flow inside the wheelhouse cavity for the cases under consideration using time-averaged streamlines (in form of ribbons). The use of twisted ribbons aids in the visualizations of the vortical structures found inside the wheelhouse cavity. The dashed lines are used to indicate the trajectories of the vortex structures discussed in the text. View from outside the wheelhouse. Flow is from left to right.

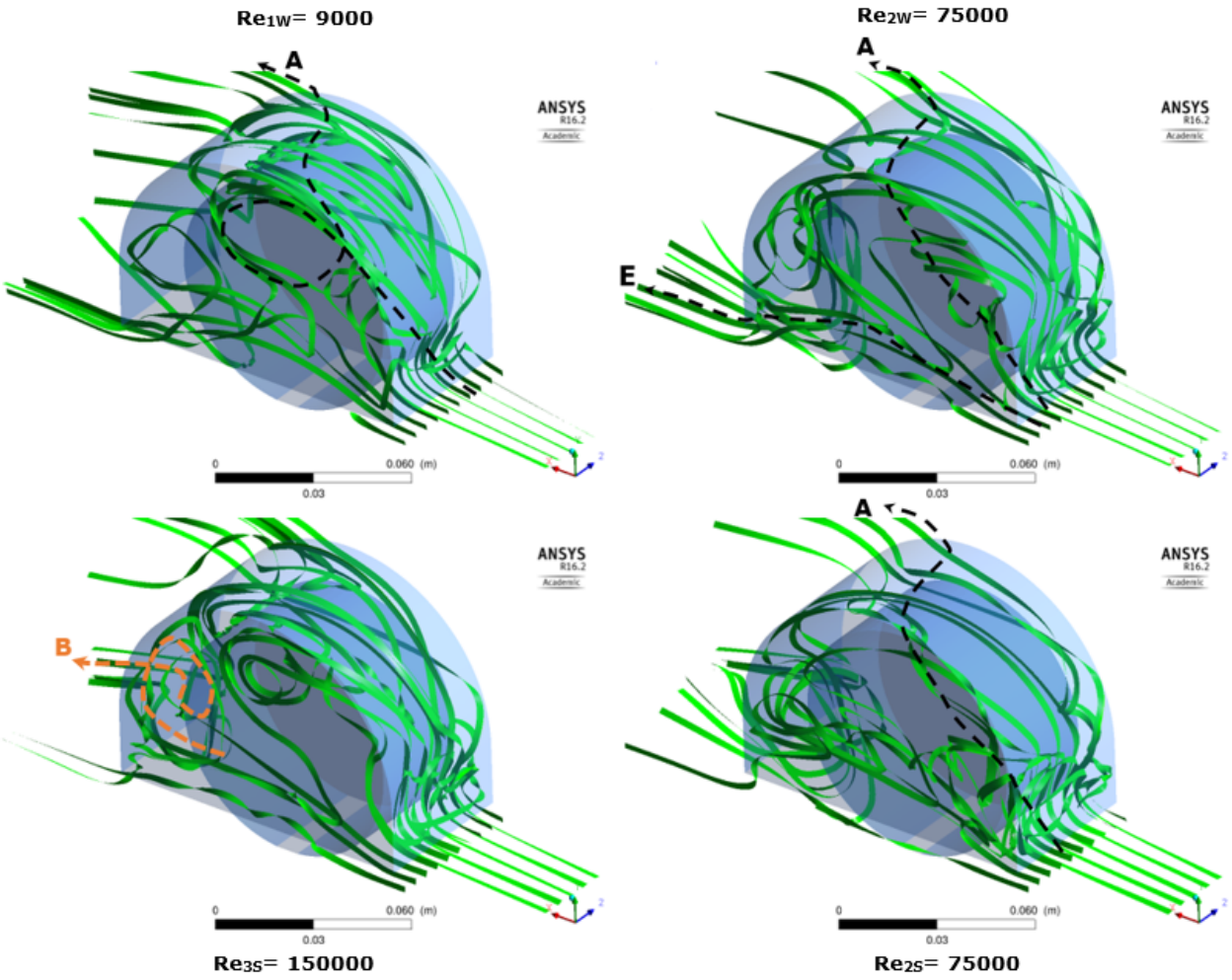


Figure 6.9: Refer caption of figure 6.8. View from inside the wheelhouse. Flow is from right to left.

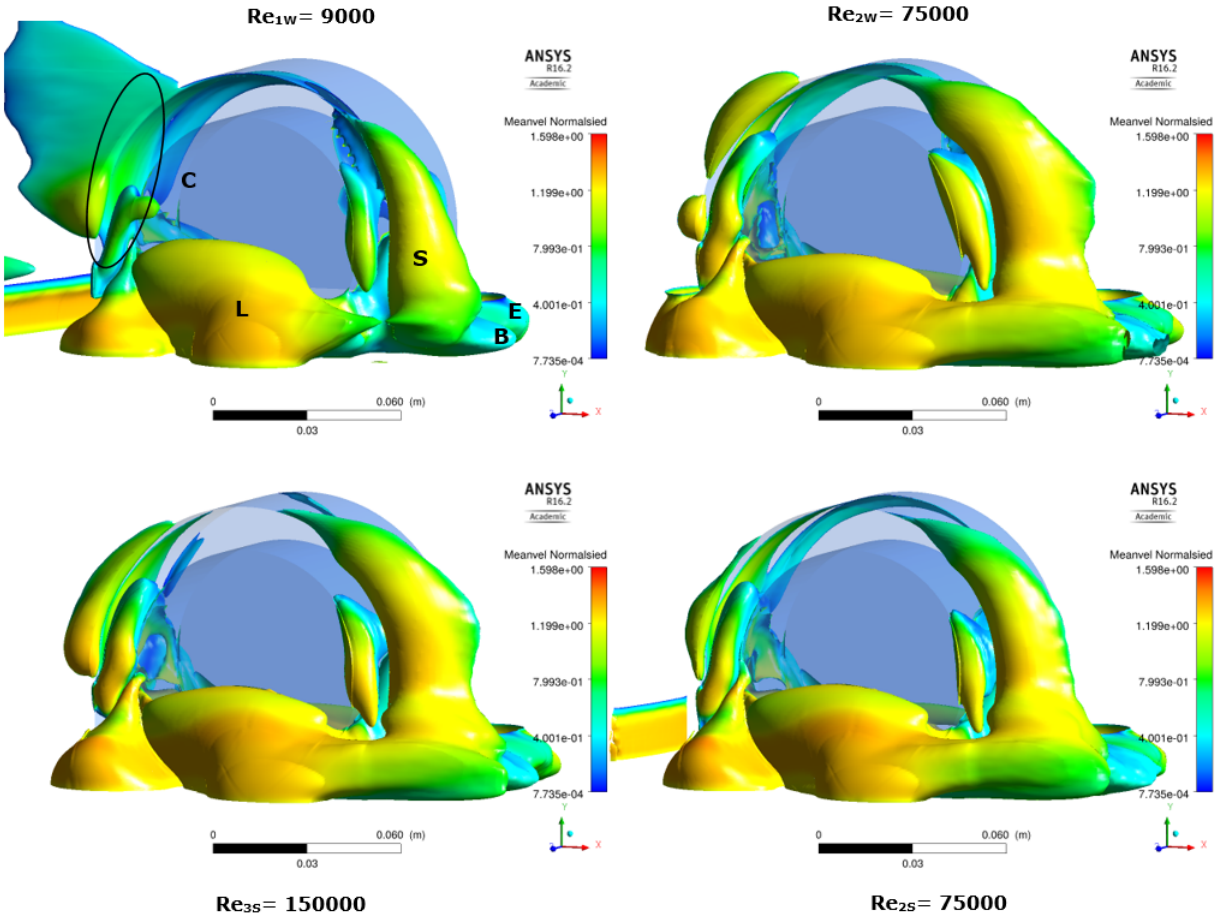


Figure 6.10: Iso-surface of low pressures, colored by the normalised velocity magnitude is compared for all the cases. The similarity between the different Reynolds numbers and even different sub-grid models can be observed. Flow is from left to right.

# Chapter 7

# Results Part III -Effect of Wheelhouse radius

From the conclusions of the previous chapter, it is clear that the behaviour of the flow at a low Reynolds number is qualitatively similar to that of realistic conditions ( i.e. high Reynolds number). Hence, the subsequent simulations comparing the effect of wheelhouse radius (*Run 2* in table 4.3) on the flow were performed at a low Reynolds number (Re = 9000). A comparison of the flow field is made between Case 1 (large wheelhouse radius) and Case 2 (small wheelhouse radius) to identify significant differences between the two configurations. A force comparison is also made between the two configurations, based on which conclusions on the relation between the flow field and drag coefficient are derived. From the derived relations, an alternate design for the wheelhouse is proposed which could potentially lead to a reduction in total drag of the vehicle.

## 7.1 Force Comparison

Comparison of the drag and lift coefficients of different sections of the vehicle, namely the wheel, the body and the wheelhouse, between the two cases is presented in figure 7.1. The basecase is a reference configuration of a vehicle with no wheel or wheelhouse. It should be noted that in Case 1 and Case 2, 'Body' refers to the entire upper body of the vehicle including the wheelhouse. The force coefficients presented here have been normalized using the front exposed surface area of the *half model*.

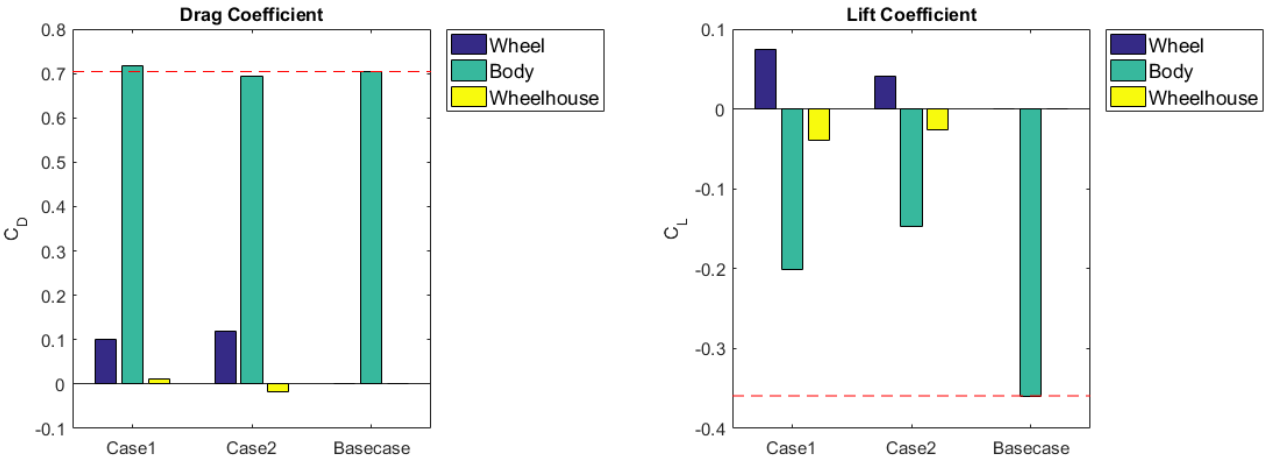


(a) (b)

Figure 7.1: The effect of reduction of wheelhouse radius on the drag and lift coefficients. The basecase is a used as a reference case which is a vehicle with no wheel and wheelhouse.

**Observations**

- The drag coefficient of the wheel is found to increase in Case 2 when compared to Case 1. Comparing the drag coefficient of the body with respect to the reference case (i.e. basecase), the value is found to decrease in Case 2 while it increases in Case 1.
- The lift produced by the wheel is found to be greater in Case 1 than in Case 2. With respect to the basecase, the lift generated by the body is found to increase in both cases but the increase is greater in Case 2.

In the above figures, the total vehicle drag coefficient can be obtained by taking the sum of wheel and body drag coefficients. The increase in total drag coefficient of the vehicle due to addition of wheel and wheelhouse was calculated to be 16% and 15% for Case 1 and Case 2 respectively. The increase in values is lower than the previously estimated value of around 40 % [2] and this can be attributed to the low Reynolds number of the flow considered in the present case.

Comparing the total body drags of Case 1 and Case 2, it was found that the drag coefficient in Case 2 was lower than Case 1 by 1%. While the reduction in drag coefficient is in agreement with results from experiment [8], the magnitude of reduction was found to be underestimated with respect to the experiment. The underestimation of the decrease in drag coefficient between the two cases can also be explained by the low Reynolds number considered here.

## 7.2 Comparison of Flow Topology

### 7.2.1 The C and S vortex

The comparison between the flow in the proximity of the leading and trailing edge of the wheelhouse arch will be considered in this section. Figure 7.2a shows the iso-surface of low pressure ($C_p$ = -0.4), colored by the mean velocity magnitude, in the wheelhouse from which the following observations can be made :

1. In Case 1, with the larger wheelhouse radius, the approaching boundary layer does separate as expected, forming the C vortex (as explained in Chapter 2). The C vortex is, however, not present in Case 2 with the smaller wheelhouse radius.
2. The S vortex, which represents the flow exiting the wheelhouse cavity from the trailing edge is found to be bigger in Case 1 than in Case 2.

Figure 7.2b shows the velocity vectors superimposed over contours of mean velocity magnitude in a plane along a section of the C vortex. The boundary layer approaching along the side of the vehicle body separates at the leading edge of the wheelhouse arch. The separating boundary layer curls up in the gap between the wheel and wheelhouse, in Case 1, which results in the formation of the C vortex. In Case 2, however, the larger outflow from the side opening, as shown by the vectors, prevents the separating boundary layer from rolling up inside the wheelhouse gap. This explains the absence of C vortex in Case 2. The larger outflux from the sides for Case 2 results in the bigger separation bubble on the sides of the wheel as shown in figure 7.2a

*Thus, the reduction of wheelhouse radius leads to an absence of C vortex and the formation of smaller S vortex.*

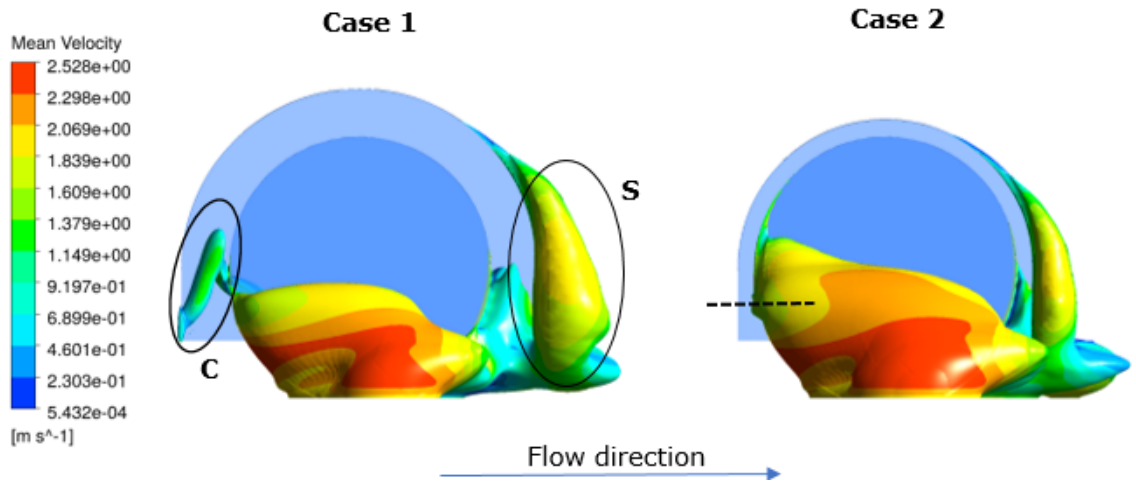


(a)

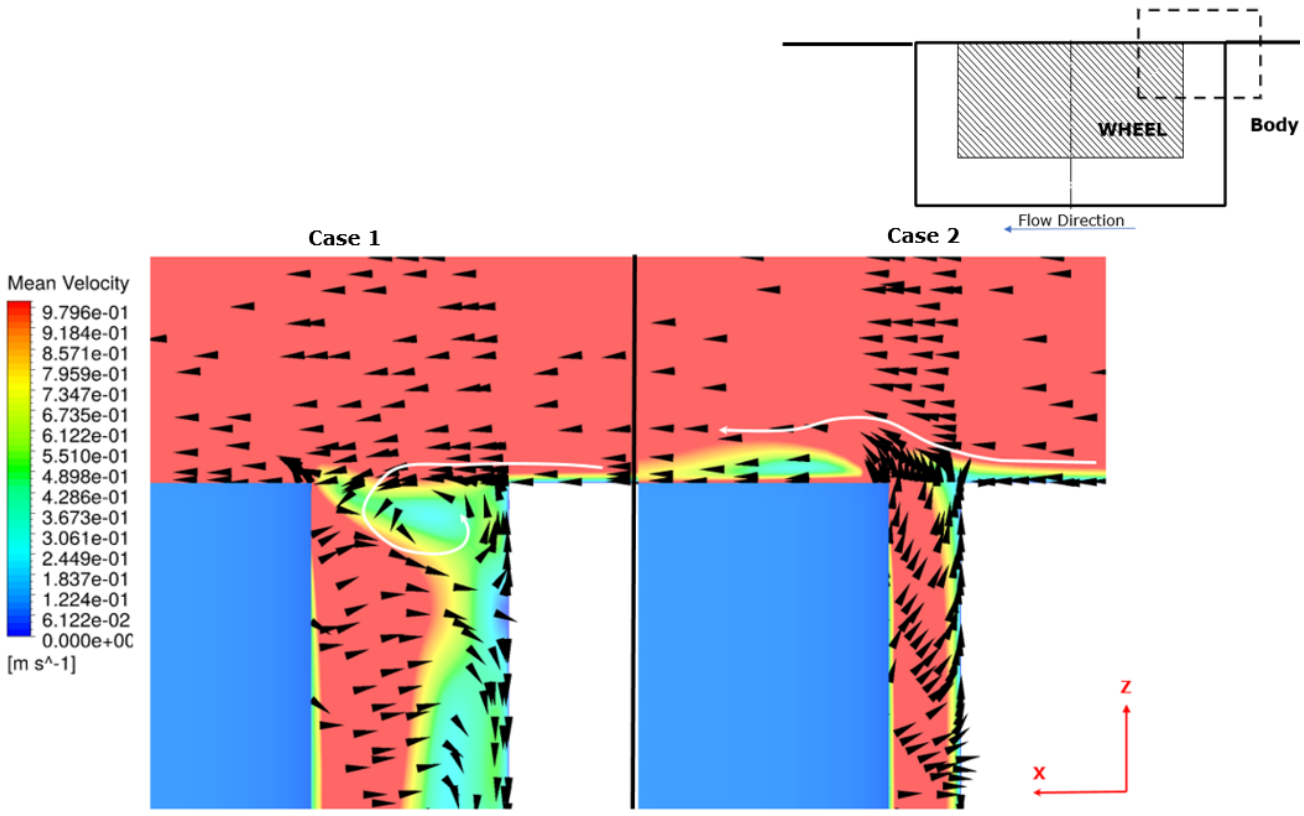


(b)

Figure 7.2: (a) The iso-surface of pressure ($C_p$ = -0.4) colored by mean velocity magnitude is shown to depict the major difference between the two cases. The absence of C vortex, the bigger separation bubble on the side of the wheel and the smaller S vortex in Case 2 is clearly shown here. (b) The behaviour of flow crossing the leading edge of the wheelhouse is depicted in this figure. The white line shows the behaviour of the boundary layer separating from the leading edge of the wheelhouse. View from the top of the plane marked by dashed line in (a)

### 7.2.2 The H vortex

The H vortex, which is formed by flow separation at the sharp corner at the wheelhouse entrance is depicted in figure 7.3b. A difference in the position of vortex core with respect to the road and the size of the vortex between the two cases can be immediately observed. The smaller H vortex in Case 2 is expected due to the smaller wheelhouse radius. To make a direct comparison between the two different sized vortices, the velocity magnitude distribution along a line passing through the core of the vortex is considered in figure 7.4a. The gap between the wheel and wheelhouse has been normalized as follows: A value of zero corresponds to the wheelhouse wall and one represents the surface of the wheel. From the profile of mean velocity magnitude, the following observations can be made:

1. The core of the vortex is closer to the wheelhouse wall in Case 2 than Case 1. The location of the first local minimum (from the wheelhouse wall) of mean velocity magnitude is used to locate the core of the vortex. (refer figure 7.4a).

2. The magnitude of velocity along the H vortex is generally greater in Case 2 than Case 1.

3. The relative size of the H vortex in Case 2 is smaller than that of Case 1. The velocity profile shows that the point of maximum velocity, which is an indication of the size of the vortex, is closer to the wheelhouse wall in Case 2 than that for Case 1.

The higher magnitude of velocity inside the H vortex in Case 2 combined with its smaller size points to a concentration of vorticity in a smaller region. *Thus, the strength of H vortex increases when the radius of the wheelhouse is decreased.*

How does the difference in strength of H vortex affect the force acting on the wheel? The figure 7.4b shows the azimuthal velocity distribution near the surface of the wheel. The region with negative azimuthal velocity is the rotating boundary layer (refer Appendix B) that rotates along with the wheel. Referring to figure 7.4b, the velocity gradient close to the wheel is found to be higher in Case 2 than in Case 1. This results in an increase in the wall shear stress on the wheel surface. Thus, it can be deduced that the effect of strength of the H vortex is reflected in the viscous shear stress acting on the wheel. The shear stress distribution as a function of wheel angular position is presented in figure 7.4c. The region between 100°and 130°shows the maximum increase in wall shear stress, when the wheelhouse radius is reduced.

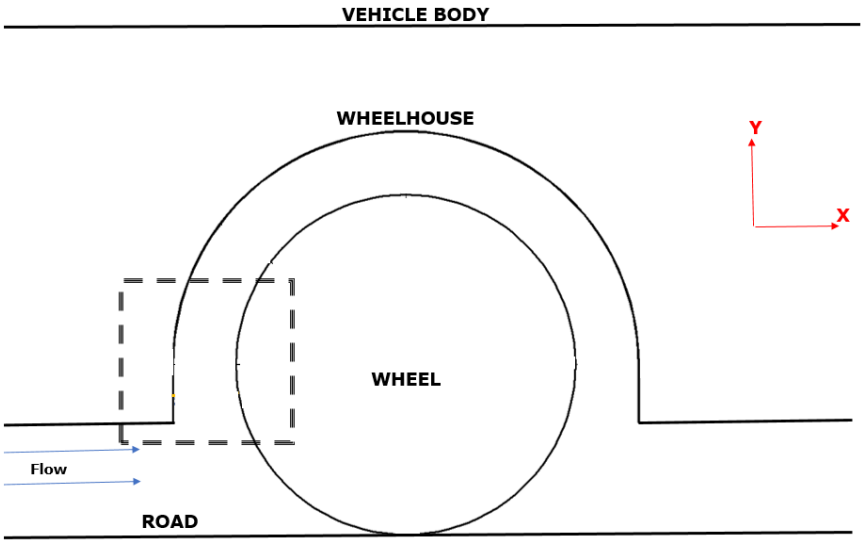


(a)

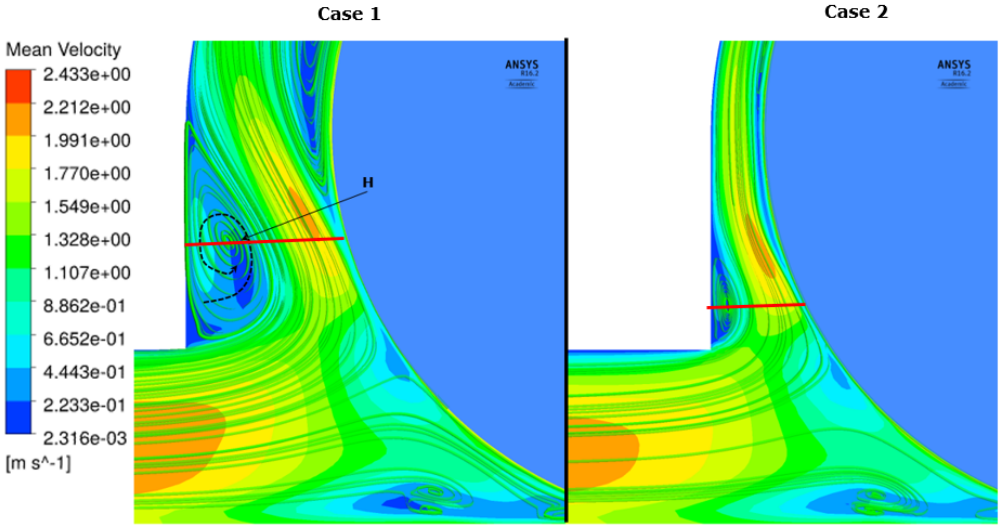


(b)

Figure 7.3: Comparison of the H vortex between Case 1 and Case 2. (a) Schematic depicting the location of the H vortex in the wheel- wheelhouse configuration. (b) The contours of mean velocity magnitude along with the streamlines is plotted in a plane marked by the box in (a). The line shown in the figure passes through the core of the vortex along which the velocity profile in figure 7.4a is plotted.

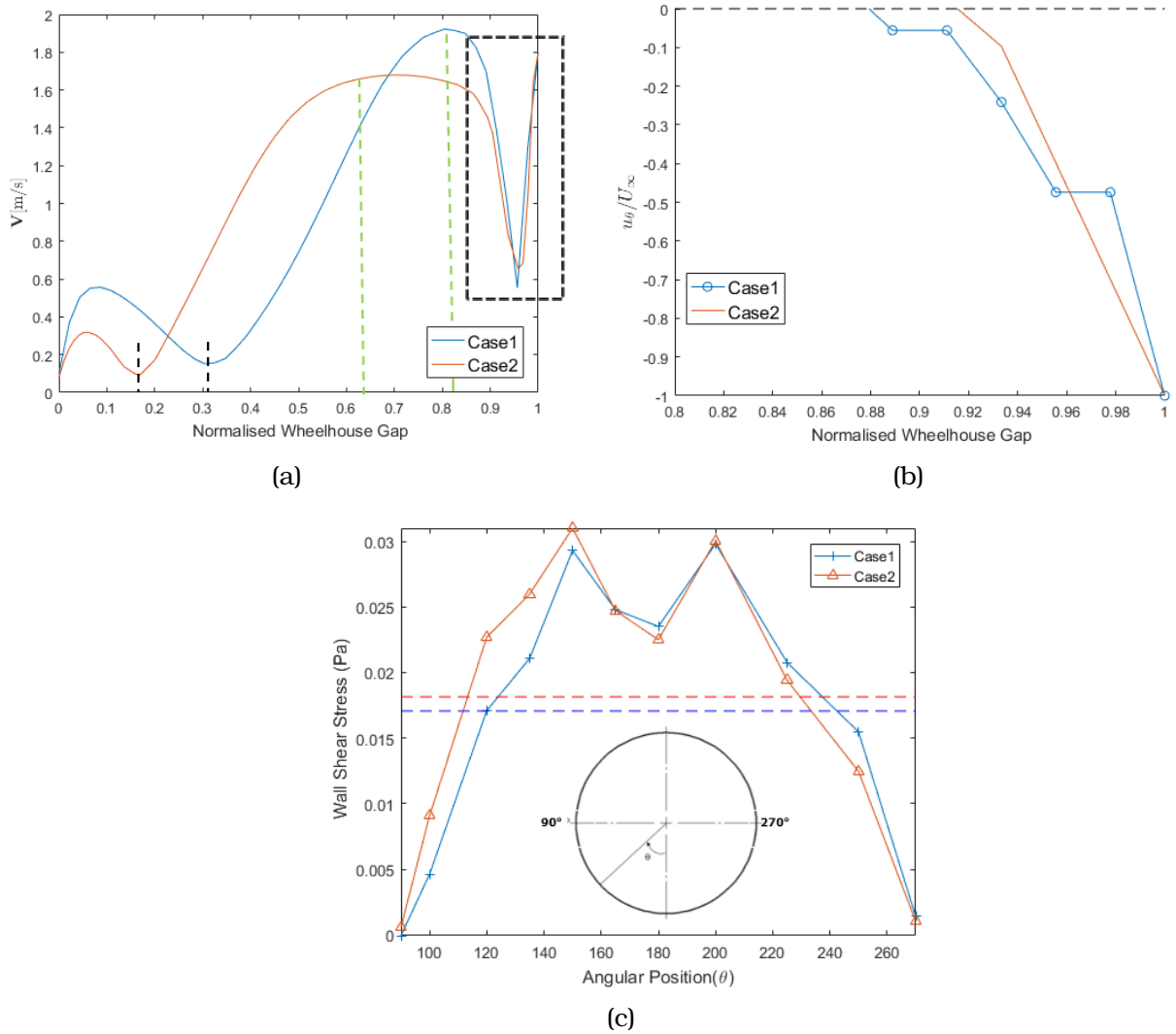


Figure 7.4: (a)The profile of the mean velocity magnitude along the line through the center of the H vortex. The location of the core (black dashed line) and the point of maximum velocity along the vortex (green dashed line) are also shown. (b) The azimuthal velocity profile in the proximity of the wheel surface (the region marked by a box in (a)). The sign convention for the azimuthal velocity is taken positive along the clockwise direction. (c)The streamwise component of wall shear stress as a function of angular position on the wheel is shown here. The dashed line represents the value of the average shear stress acting on the total surface of the wheel between 90°and 270°for the respective cases.

The shear stress values shown in figure 7.4c are plotted by taking the mean of the shear stress values along the span of the wheel - for a given angular position. The dotted line in the above figure represents the mean shear stress acting on the surface of the wheel between 90°and 270°. Based on the mean shear stress, the mean shear force and its corresponding drag coefficient can be calculated. The drag coefficient thus calculated was found be 0.0029 for Case 1 and 0.0031 for Case 2. Based on the calculated values, two inferences can be made :

- The viscous drag force was found to increase by 7 % when the wheelhouse radius is reduced.
- When looking at the percentage of viscous contribution to the total drag force acting on the wheel, it was found that for Case 1, the viscous contribution amounted to 3 % whereas for Case 2 it was calculated to be 2.6 %.

*Thus, it can be concluded, based on the above findings, that the main contributor for the increase in drag of the wheel observed when the wheelhouse radius is reduced, is the pressure force.*

### 7.2.3 The A Vortex

The comparison between the two cases, on the behaviour of the A vortex, is made by releasing streamlines from a line near the bottom entrance of the wheelhouse cavity (refer figure 7.5). The following observations can be made:

1. In Case 1, the A vortex is formed as described in Chapter 2. The extension of the H vortex that travels over the wheel experiences a suction on top of the wheel (refer 7.6b), that results in the flow exiting from the top of the wheelhouse cavity.

2. In Case 2, however, the part of the H vortex that flows to the top, recirculates and merges with the flow along the side of the wheel and eventually exit the cavity as the E vortex. A small part of the flow travels across the wheel to exit the cavity from the sides as the S vortex.

Figure 7.6a is a better representation of the difference between the two cases. The lower wheelhouse radius is found to restrict the amount of flow exiting the wheelhouse cavity from the top. *Thus, the amount of cross flow is greatly affected when the wheelhouse radius is reduced, which leads to a difference in behaviour of the A vortex.*

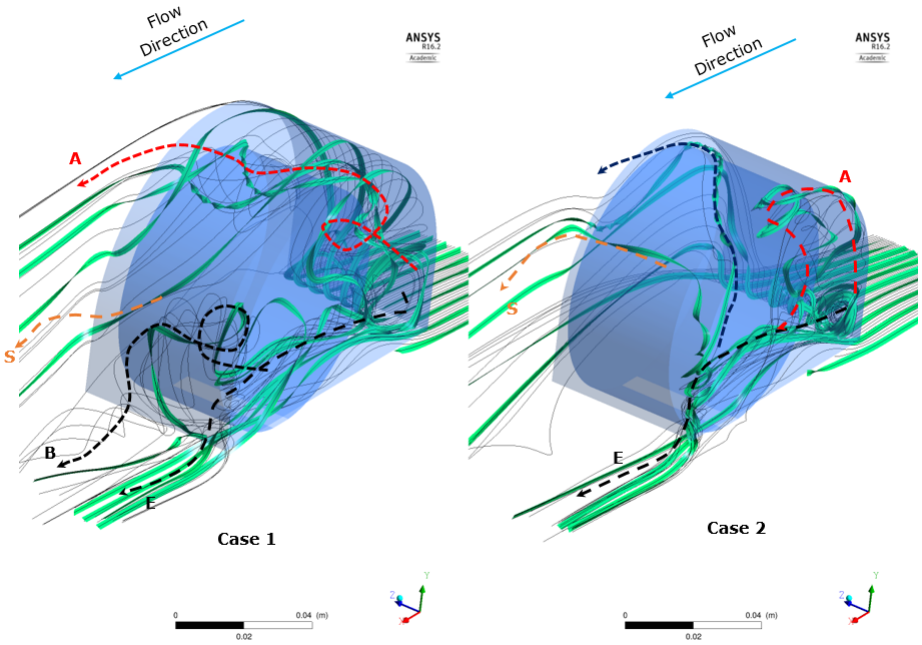


Figure 7.5: The major effect of reducing the wheelhouse radius is in the behaviour of the flow entering the wheelhouse cavity through the bottom opening of the wheelhouse. The recirculation of A vortex into the wheelhouse cavity can be observed.

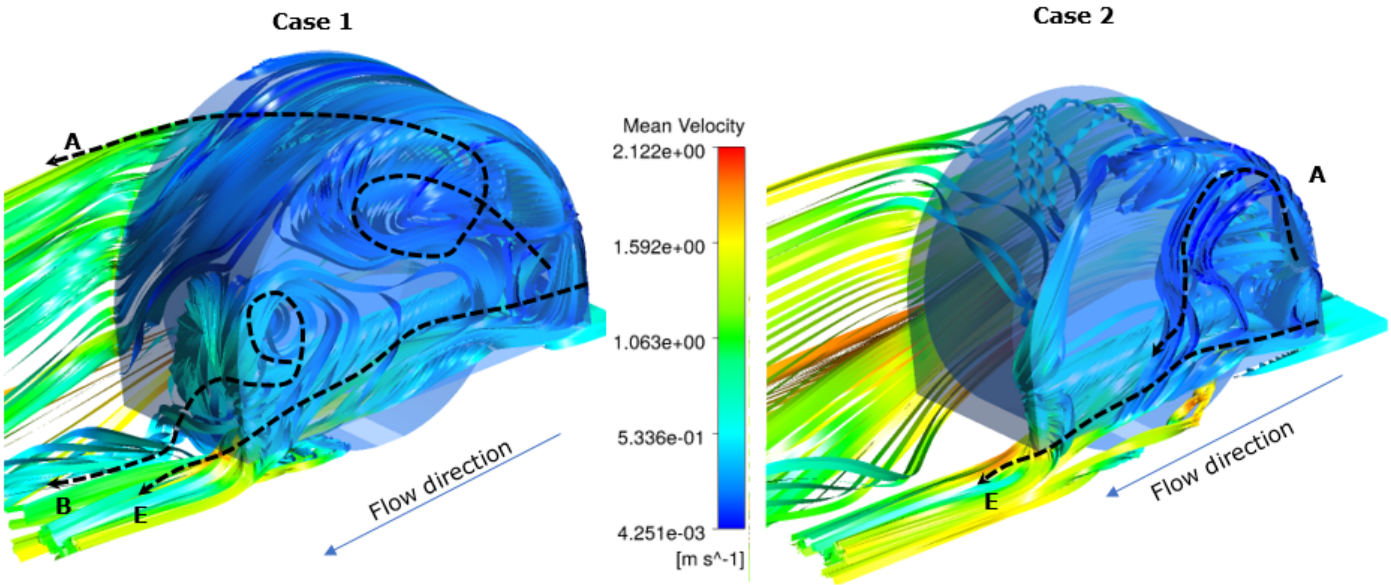


(a)

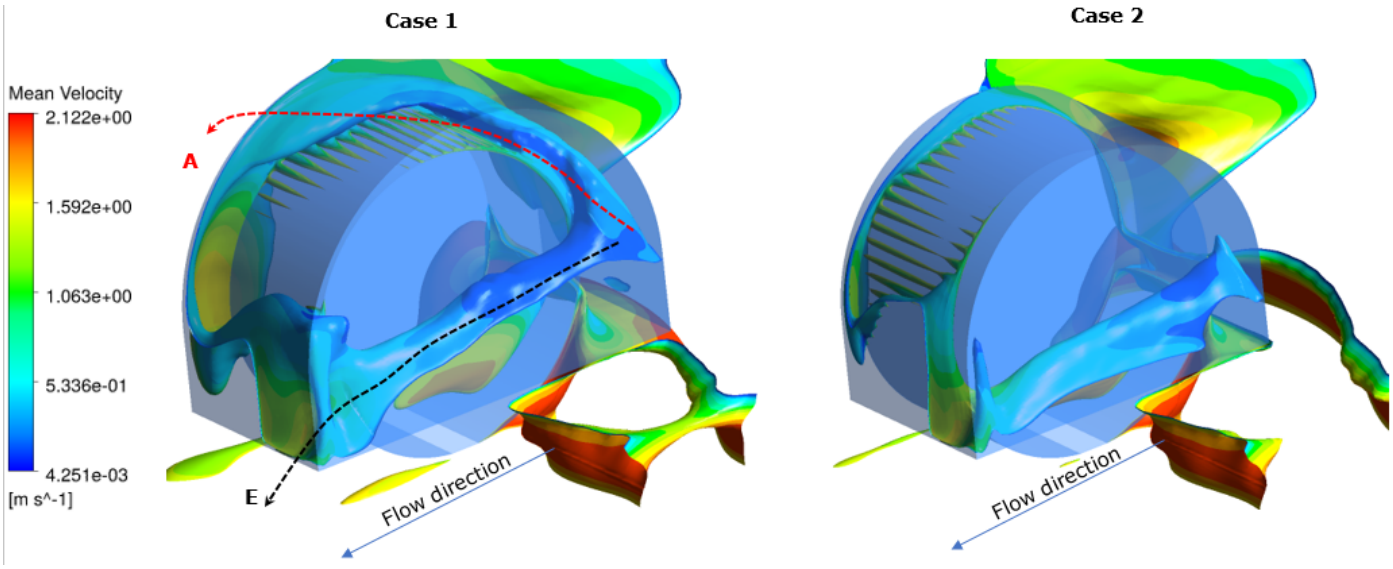


(b)

Figure 7.6: (a)The flow entering the wheelhouse cavity through the H vortex is depicted using a dense streamline pattern. The difference in behaviour of A vortex between Case 1 and Case 2 is shown here. The absence of cross-flow in Case 2 can be observed. (b) The iso-surface of mean pressure coefficient ($C_p$=-0.18), colored by mean velocity magnitude, is shown here. The flow experiences a suction at the top of the wheel in Case 1, which results in a greater proportion of cross flow. The streaks of contours on the wheel surface are artifacts which are found to be present due to the imperfect representation of the curved surface of the wheel.

### 7.2.4 The B vortex

Consider the vectors shown in the figure 7.7, that represents the flow in the wake of the wheel and near the ground. In both cases, a circulation with the same sense of rotation as that of the B vortex can be observed, and hence it can be concluded that the B vortex is indeed present in Case 2. But from figure 7.5, it can be seen that the B vortex is not visible for the Case 2 geometry. The reason for this absence can be explained by the difference in mechanism of formation of the B vortex between the two cases.

⇒ *Case 1*: The flow entering the cavity through the bottom opening, travels along the side of the cavity and encounters the wheelhouse wall. The recirculating flow travels across the trailing edge of the wheel before exiting from the bottom cavity. The flow separation from the wheel edge results in the formation of the B vortex which can thus be considered as a tip vortex (refer 7.8b).

⇒ *Case 2*: The B vortex is formed due to the separation of the flow travelling along the side of the wheel, at the trailing edge of the wheel (refer 7.8b).

The presence of the low pressure zone behind the wheel is found to result in the diagonal separation of flow in Case 1 (represented by red dashed lines in figure 7.8a). The low pressure suction behind the wheel, which is bigger in Case 1 than in Case 2, leads to a loss of momentum of the flow exiting the wheelhouse cavity in Case 1. The loss in momentum of the flow is found to result in a weaker B vortex for the Case 1 geometry as shown in figure 7.9. *In other words, the absence of a suction zone in the trailing edge of the wheel in Case 2 leads to the formation of a stronger B vortex.*

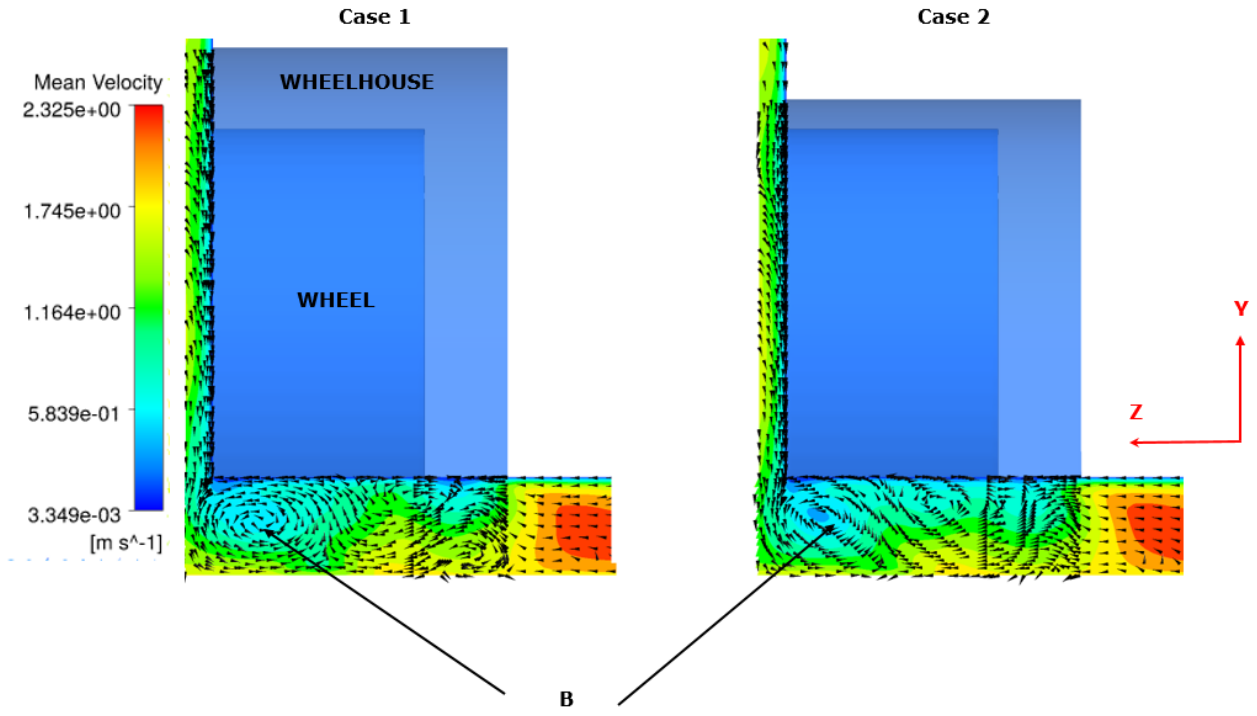


Figure 7.7: The B vortex visualized using surface vectors on a plane 1D behind the wheel, where D is the diameter of the wheel. Flow is out of the plane.

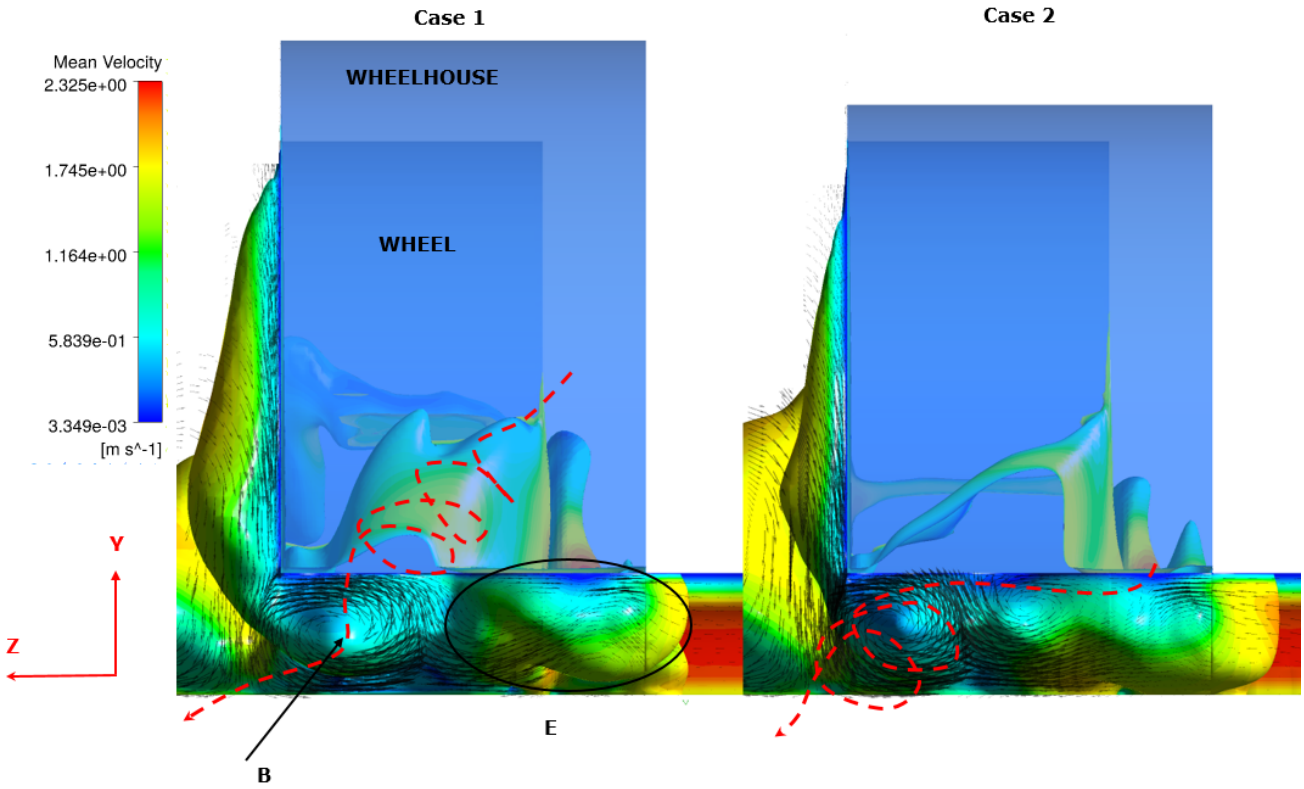


(a)

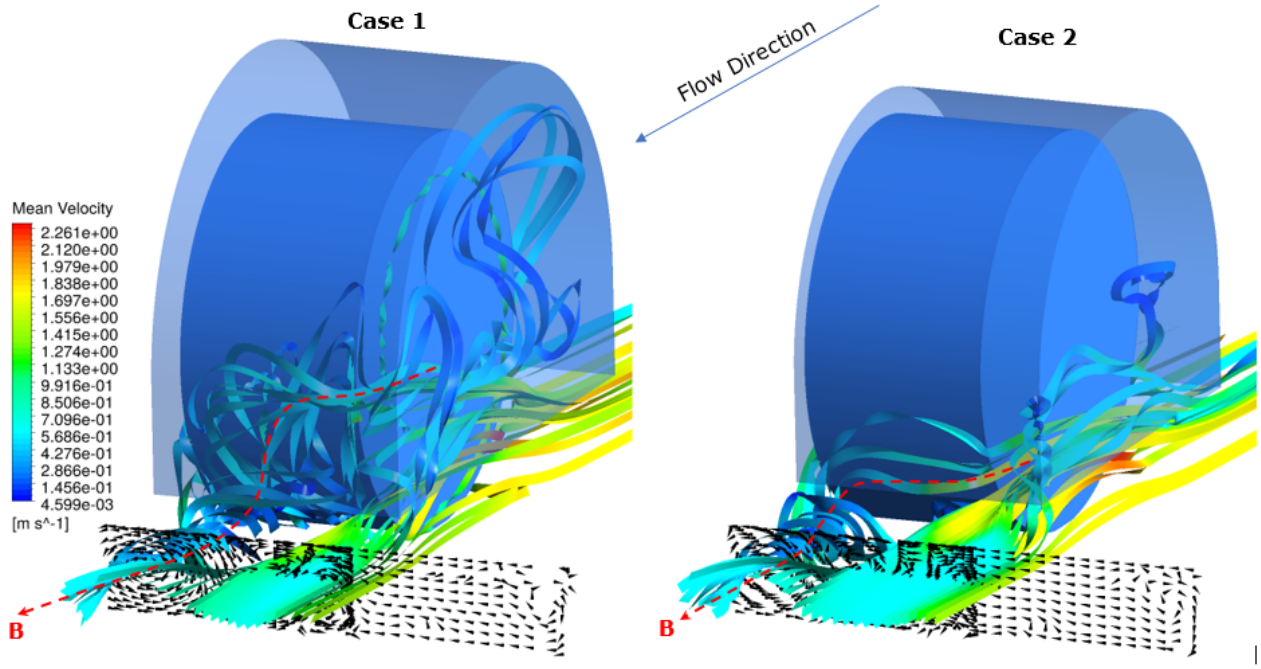


(b)

Figure 7.8: (a) Iso-surface of low pressures colored by mean velocity magnitude, depicting the formation of the B vortex in the two cases. The difference in formation of the B vortex is explained schematically using the dashed lines. Flow is out of the plane. (b) Visualization of B vortex in the two cases using streamribbons. The effect of the low pressure region behind the wheel on the flow in Case 1 is clearly represented here.

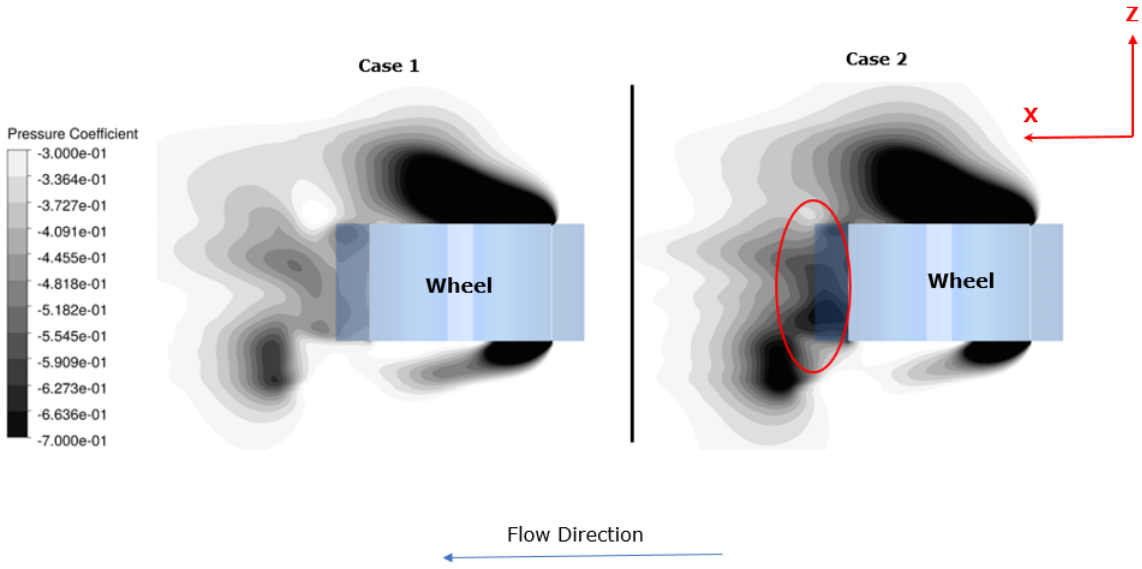


Figure 7.9: Contours of mean pressure coefficient in the plane below the underbody as viewed from the top. The lower magnitude of pressure, indicated by the red circle, indicates a stronger B vortex in Case 2.

To summarize the conclusions from the above comparison,

1. The lower wheelhouse radius eliminated the separation of flow in the leading edge of the wheelhouse arch resulting in the absence of C vortex.

2. The lower wheelhouse radius results in a smaller and stronger H vortex that leads to an increased shear stress on the wheel. The viscous contribution to the total drag was however found to be negligible.

3. A difference in behaviour of the flow entering the wheelhouse cavity through the H vortex was observed between the two cases. The most striking distinction between the two cases was the amount of flow travelling over the wheel. The reduction of wheelhouse radius resulted in an increased pressure over the wheel, thus reducing the amount of cross flow (i.e. flow across the span of the wheel).

4. The B vortex, formed as a consequence of flow exiting the wheelhouse cavity from the bottom, is found to be weaker when the wheelhouse radius is larger (i.e. in Case 1). This is attributed to the greater loss in momentum of the flow in Case 1 where the flow exiting the wheelhouse is affected by a low pressure region behind the wheel.

5. The amount of flow exiting the wheelhouse cavity from the side opening (i.e. the S vortex) is reduced when the radius of the wheelhouse is decreased.

## 7.3 Analysis of Force variations

In section 7.1, a basic comparison of the force coefficients was presented. The present section is aimed at answering the question *" What causes the variation in drag force observed, when the wheelhouse radius is changed?"*

### 7.3.1 Body Drag

Consider the various drag contributions shown in figure 7.1a. It was determined that :

1. The increase in drag of the body in Case 1, with respect to the reference case (vehicle without wheel or wheelhouse) is comparable with the magnitude of the drag coefficient of the wheelhouse.

2. And similarly, the decrease in drag of the body in Case 2, with respect to the reference case is comparable with the value of the negative drag coefficient of the wheelhouse.

The above facts suggests that the inclusion of the wheelhouse cavity and is the main contributor to the change in drag coefficient of the body. Thus, it can be expected that the pressure distribution in the wheelhouse dictates the observed change in drag coefficient of the body.

The sectional drag coefficients of the wheelhouse for the two cases have been calculated and are shown in figure 7.10. On reducing the wheelhouse radius (i.e. Case 2) a drastic reduction in drag coefficient along the outer edge of the wheelhouse ($Z^+_{wh} = 1$) can be observed. At the same time, the value of the drag coefficient along the inner sections is found to be very similar in both the cases. The above observations can be explained by looking at the pressure distribution along these sections.

Figure 7.11 shows the $C_p$ curve along two different sections of the wheelhouse ($Z^+_{wh} = 0.4$ and $Z^+_{wh} = 1$). The decrease in drag coefficient at the outer edge ($Z^+_{wh} = 1$) can be explained as follows: higher pressures in Region I results in an increase in thrust force on the wheelhouse. Similarly, lower pressures in Region II leads to a reduction in drag force on the wheelhouse. The increased thrust in Region I, combined with the decreased drag in Region II leads to an overall decrease in sectional drag coefficient at $Z^+_{wh} = 1$ as shown in figure 7.10. In the inner sections however, the increase in thrust force in Region I is compensated by the increase in drag force in Region II (figure 7.11a). This leads to the similarity in values of sectional drag coefficient along the inner sections.

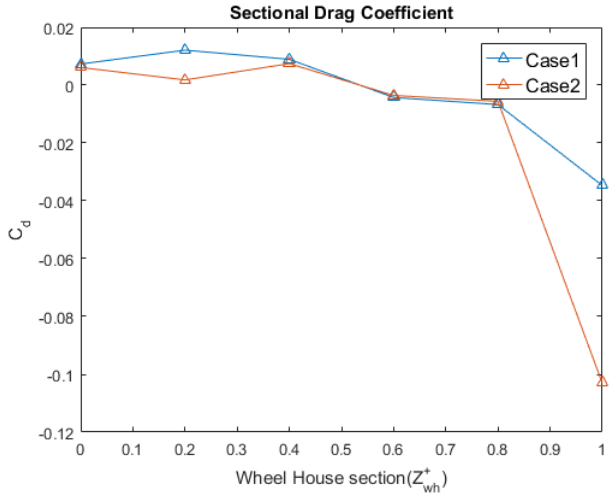


Figure 7.10: The sectional drag coefficients of the wheelhouse compared between the two cases. A drastic reduction in drag coefficient at the outer edge of the wheelhouse can be noted for the Case 2.

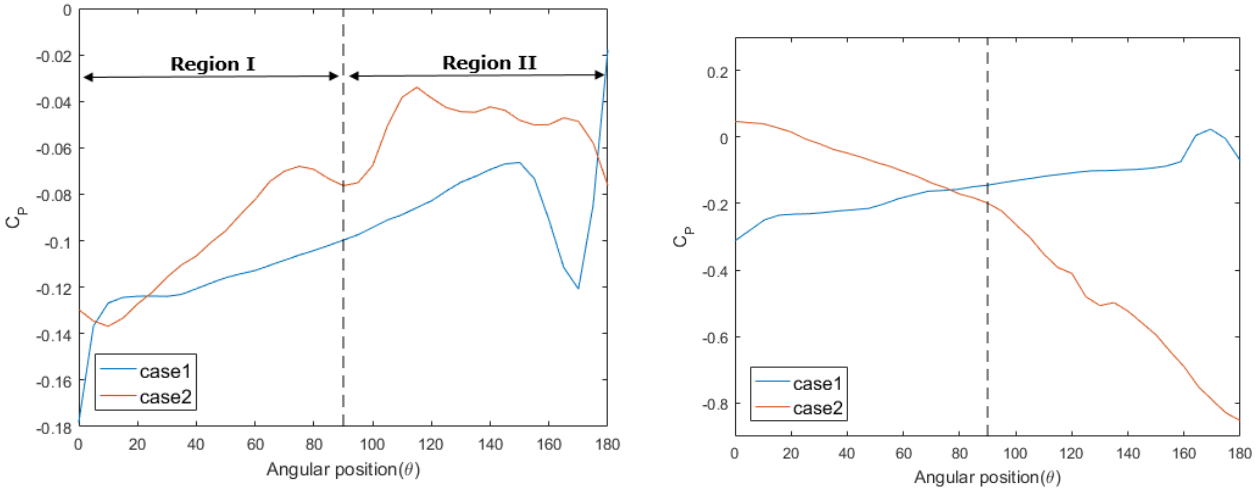


Figure 7.11: (a) The pressure distribution along an inner section of the wheelhouse (b) The pressure distribution along the outer edge ($Z^+_{wh} = 1$) of the wheelhouse. The dashed line is at an angle of 90°and it divides the plot into two regions which is explained in the text.

While the mean drag coefficient of the wheelhouse shown in figure 7.1a shows a big difference between the two cases, the plot shown in 7.10 shows a variation only along the outer edge of the wheelhouse. The reason for the low variation in sectional drag coefficients between the two cases can be explained by looking at the angular definition of the wheelhouse. From figure 7.12, it can be seen that the surface of the wheelhouse below the horizontal line (0°and 180°) was not considered in the calculation of sectional force coefficient. Given that these surfaces, marked as T and T', are perpendicular to the flow, the contribution of these surfaces to the total drag coefficient can be expected to be higher.

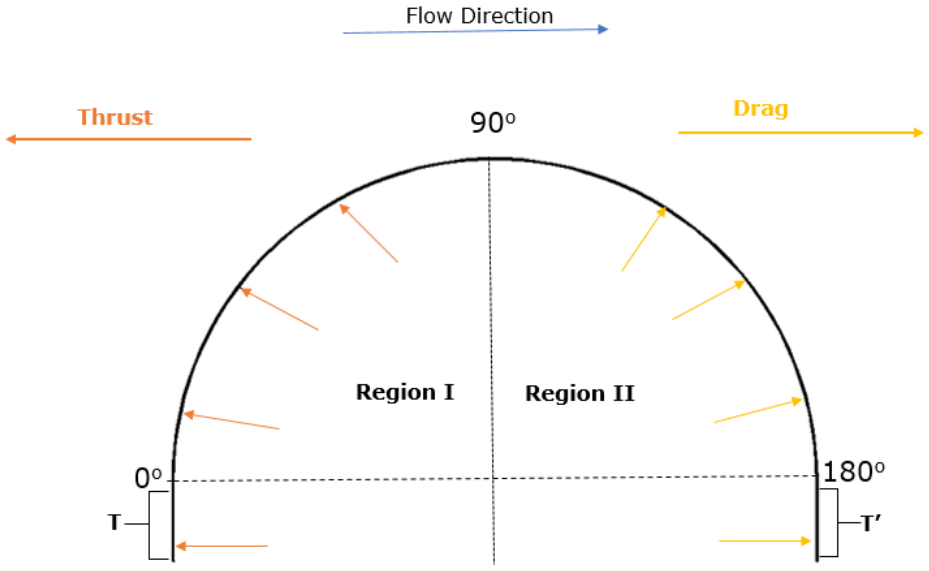


Figure 7.12: Diagram depicting the action of pressure force on the surface of the wheelhouse. The horizontal component of the resulting pressure force, in the respective regions, is also represented.

The contour of mean pressure coefficient on the wheelhouse surface, including the surfaces T and T', is shown in figure 7.13. It can be seen that the pressure on surface T is higher in Case 2 when compared to Case 1 which leads to an increase in thrust force on the wheelhouse. At the same time, the pressure in region T' is lower in Case 2 when compared to Case 1 which leads to the decrease in drag force on the wheelhouse. The combined effect leads to a decrease in the drag coefficient of the wheelhouse and hence the body for the Case 2 geometry

The smaller size of the H vortex in Case 2 (refer section 7.2.2), is found to reduce the area over which the low pressure region is distributed which explains the higher pressures on surface T. Similarly, the stronger B vortex observed in the wake of the wheel near the wheelhouse exit (refer figure 7.8) explains the lower pressure on surface T' in Case 2.

Another observation from the pressure distribution on surface T for the Case 1 geometry, is the acute low pressure near the edge of the wheelhouse (marked by red arrow in figure 7.13). The formation of the C vortex due to the boundary layer separation (section 7.2.1) explains the presence of this low pressure zone on surface T in Case 1.

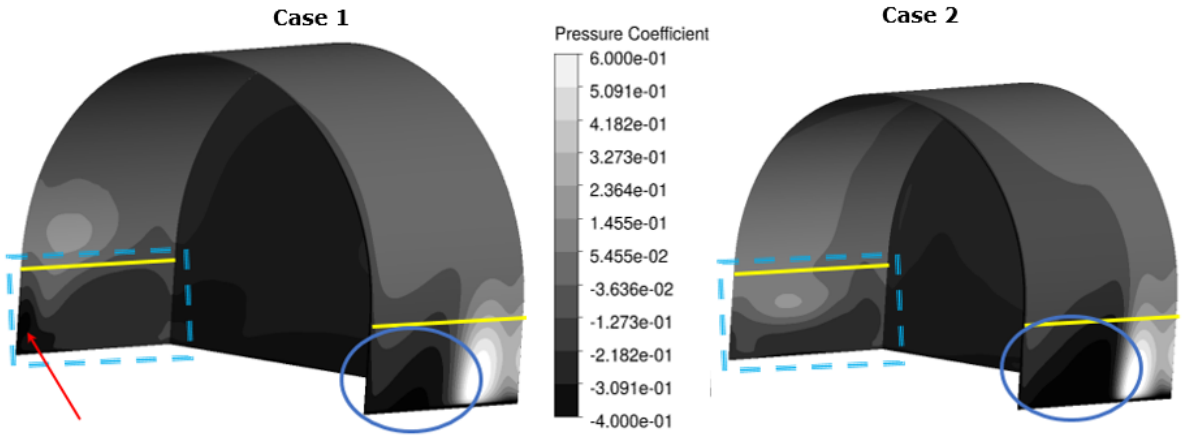


Figure 7.13: The contours of the mean pressure coefficient compared between the two cases. The yellow line corresponds to an angular position of 0°shown in figure 7.12. The higher pressure on surface T (marked by the box) and the lower pressure on surface T' (marked by the circle) for Case 2 can be observed. The red arrow marks the boundary layer separation due to formation of the C vortex in Case 1.

### 7.3.2 Wheel Drag

It is known that the drag coefficient of the wheel is higher in Case 2 than in Case 1 from section 7.1 (refer figure 7.1). Referring back to section 7.2.2, it was also found that the viscous contribution to the total drag of the wheel is negligible. Hence, the increase in drag coefficient of the wheel observed between the two cases must be reflected in the pressure distribution.

Consider figure 7.14a, where the sectional force coefficient of the wheel is compared between the two cases. Contrary to the observation in the previous section about body drag coefficient, the increase in wheel drag coefficient is not a local effect but rather reflected on all the sections of the wheel. The maximum difference was found in the drag coefficient along the inner edge of the wheel ($Z_w^+ = -0.5$). The $C_p$ curves along the wheel inner edge ($Z_w^+ = -0.5$), outer edge ($Z_w^+ = 0.5$) and mid section ($Z_w^+ = 0$) are also presented in the figure 7.14. Based on the pressure distribution on the wheel surface, the following inferences can be made:

1. The major difference between the two cases is found to be in the magnitude of negative pressure on the trailing surface of the wheel, especially near the contact patch (300 - 350°), which can be observed across all the sections.

2. At the mid section of the wheel ($Z_w^+ = 0$), the pressure distribution over the majority of the wheel surface is similar. Differences start to arise from an angle of 300°where the surface pressure in Case 2 starts to reduce when compared to that of Case 1.

3. The drag coefficient at the outer edge ($Z_w^+ = 0.5$) shows minimum variation between Case 1 and Case 2. Despite the lower pressures observed on the trailing surface (300°- 350°) for Case 2, the pressure on the leading surface of the wheel (50°- 100°) is also lower. Thus, the overall effect on the pressure differential across the wheel surface is minimal, leading to the similarity in sectional drag coefficient.

4. On the inner edge ($Z_w^+ = -0.5$), higher pressures on the leading surface of the wheel and lower pressures on trailing surface of the wheel are observed for the Case 2 geometry. This leads to an increase in pressure difference across the the wheel surface leading to the increase in sectional drag coefficient along this section.

Thus, it can be concluded that the major reason for the increase in drag coefficient of the wheel is decrease in pressure in the wake of the wheel. The lower pressures behind the wheel leads to an increase in the pressure force on the wheel caused by the increased pressure differential across the wheel surface resulting in a higher drag coefficient. The lower pressure in the wheel wake for Case 2 is clearly shown in figure 7.15, where the near ground mean pressure coefficient are compared between the two cases. The decrease in pressure at the contact patch can be correlated with a stronger jetting vortex, especially the inner jetting vortex (R1). The lower pressure in the wake of the wheel, in general, can be attributed to the stronger B vortex in the Case 2 geometry.

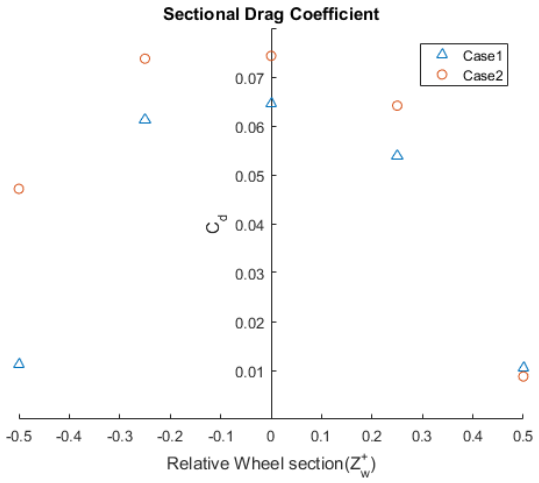


(a)

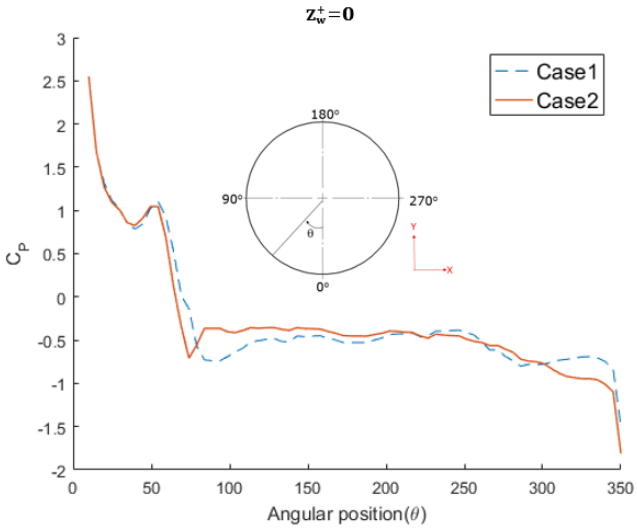


(b)

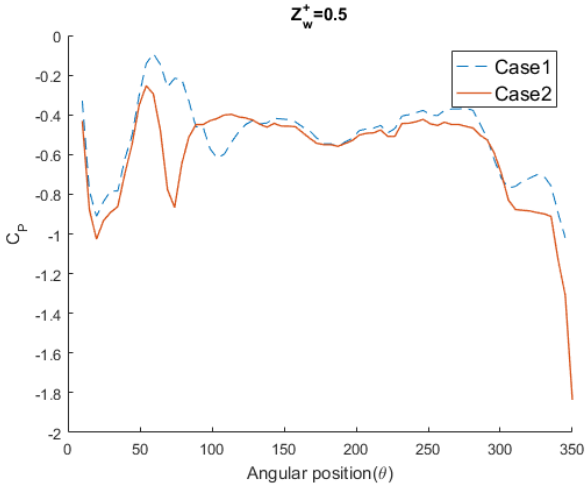


(c)

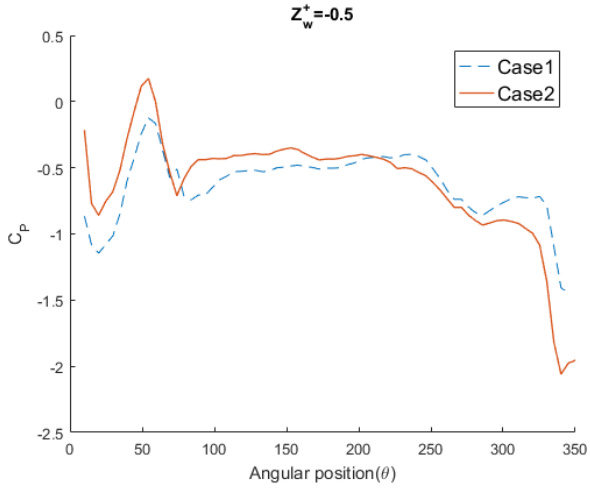


(d)

Figure 7.14: (a) The comparison of the sectional force coefficients of the wheel between two cases. (b),(c) and (d) shows the comparison of the pressure distribution along the wheel surface at the center, outer and inner edge respectively.

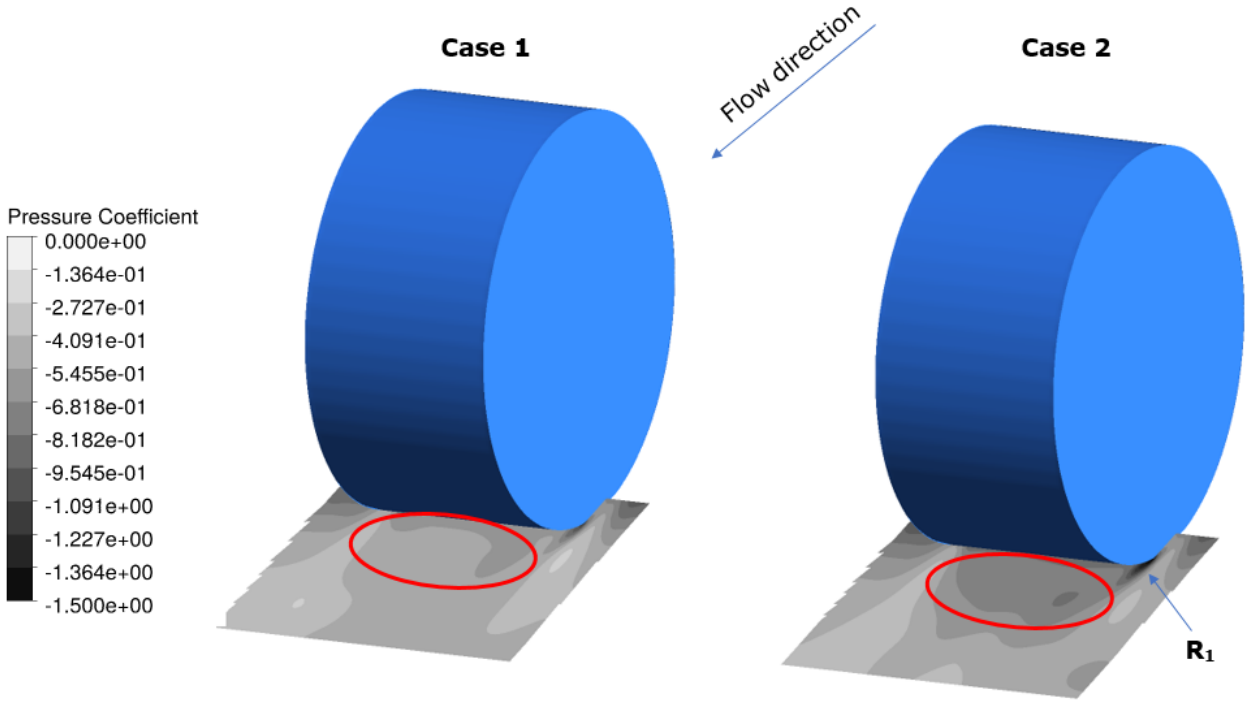


Figure 7.15: The near ground contours of mean pressure coefficient compared between the two cases. The region corresponds to the pressure in the suction side of the contact patch. Flow is from right to left.

## 7.4 Conclusions on the Force Analysis

Based on the analysis of wheel and body forces, it can be concluded that the decrease in wheelhouse radius leads to:

1. A lower pressure behind the wheel. This results in the increased pressure differential across the wheel causing an increase in drag coefficient. The B vortex was found to be responsible for the lower pressures in the wake of the wheel. Additionally, the stronger R1 vortex resulted in a lower pressure near the contact patch, behind the wheel.

2. Higher pressures on the leading surface of wheelhouse (surface T) and lower pressures on the trailing surface of the wheelhouse (surface T') lead to a decrease in drag coefficient of the wheelhouse. The smaller H vortex and to some extent the absence of the C vortex, explains the higher pressures on surface T. The stronger B vortex is found to be responsible for the decrease in pressure on surface T'.

So, it can be seen that 4 vortices - the H, the B vortex, the C and the R1 - play a crucial role in determining the drag coefficient of the wheel and vehicle body, when the geometry of the wheelhouse is changed. Now, it was found that the temporal variation of the drag coefficient of the wheel is highly unsteady. Can the above conclusions be used to explain this unsteady behaviour of the drag coefficient? A brief analysis to answer this question will be performed in the next section for the Case 1 geometry.

## 7.5 Conditional Averaging

Consider the time signal of the drag coefficient of the wheel shown in figure 7.16a. The drag signal was obtained from the solution of Case 1 i.e the case with larger wheelhouse radius. It can be seen that the drag coefficient oscillates by as much as 10% about the mean value.

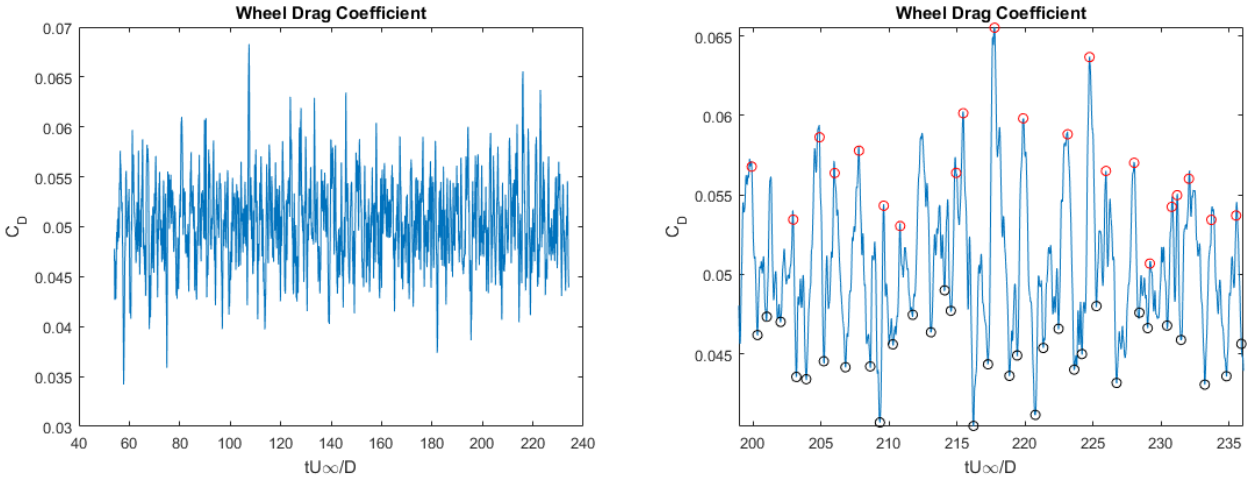


(a) (b)

Figure 7.16: (a) The time history of the drag coefficient of the wheel for the case with larger wheelhouse radius (Case1). (b) A section of the drag signal is shown for which transient data was collected for analysis. The red circles indicate conditions of local maxima while black circles indicate local minima.

The transient data was collected for a duration which corresponds to 35 passes through the wheel. The data was collected after enough time had passed, to ensure that the flow had reached a fully-developed state. Figure 7.16b shows the section of the drag signal for which the transient data was taken. From this, the local maxima (red circles) and local minima (black circles) were identified and the corresponding time step noted. The data sets of the above calculated time steps were grouped together and averaged that resulted in a conditionally averaged flow field corresponding to a " high drag" and a " low drag" condition. Using this conditionally averaged data, the previous force analysis was carried out briefly.

### 7.5.1 Sectional Drag Coefficients

#### Wheel

The distribution of the pressure along the mid-section ($Z_w^+ = 0$) and the sectional drag coefficients of the wheel are shown in figure 7.17. The mean condition represents the values that are averaged over the entire temporal domain, while the high and low conditions are the conditionally averaged data as explained in the previous section.

Based on the sectional force coefficients, it can be seen that a global increase/decrease in drag coefficient, with respect to the mean condition, takes place during the high/low drag conditions. The pressure distribution along the mid section, shown in figure 7.17b, shows that the high drag condition correlates with higher pressures on the leading surface of the wheel and lower pressures on the trailing surface of the wheel. And the opposite effect is observed when the drag coefficient of the wheel decreases (i.e. low drag condition).

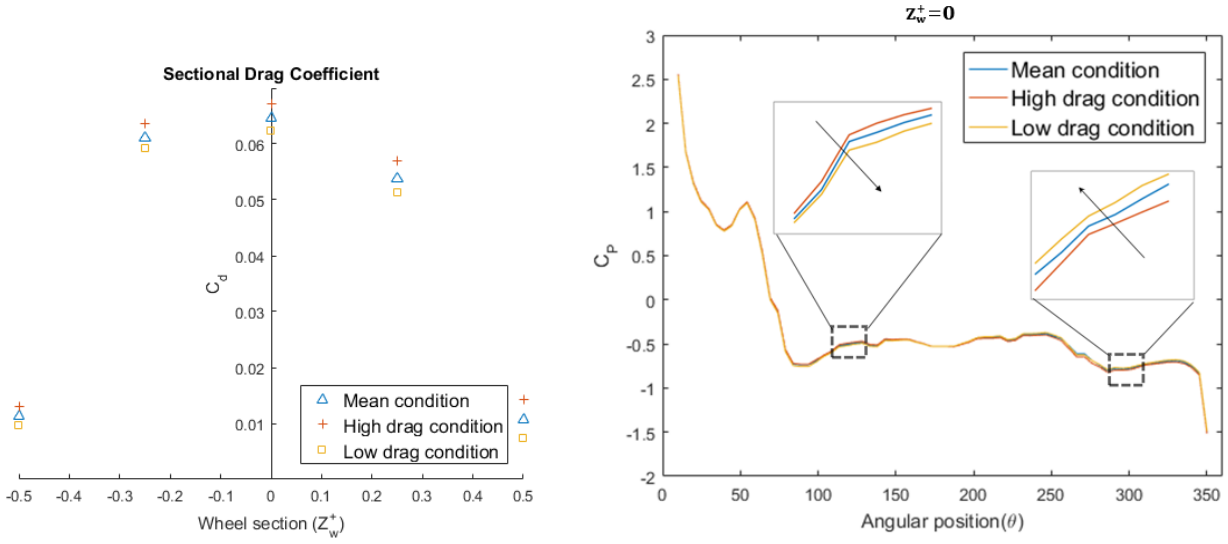


(a) (b)

Figure 7.17: (a) The sectional force coefficients compared between the conditionally averaged data and the mean data. (b) The $C_p$ curves along the centre of the wheel is shown for the data mentioned before. Higher pressures on the leading surface (0°-180°) combined with lower pressures on the trailing surface (180°- 360°) of the wheel results in the "high" drag condition

### Wheelhouse

The pressure distribution along the outer section ($Z_{wh}^+ = 0.8$)[1] and the sectional drag coefficient of the wheelhouse are shown in figure 7.18. It can be seen that :

1. The wheelhouse drag coefficient *reduces* globally in the *high* drag condition, i.e. when the wheel drag is high, with respect to the mean value .
2. At the *low* drag condition, i.e. when wheel drag coefficient is low, only the drag coefficient along on the outer edge is found to *increase* with respect to the mean value.

The local increase in drag coefficient of the wheelhouse at the low drag condition can again be explained by the definition of angular position along the wheelhouse (refer section 7.3.1). Overall it can be observed, from the $C_p$ curve along the outer edge (figure 7.18b), that higher pressures on the leading surface of the wheelhouse (Region I) and lower pressures on the trailing surface of the wheelhouse (Region II) leads to a decrease in the drag coefficient of the wheelhouse.

[1]Conditionally averaged data were not available for the sections $Z_{wh}^+ = 0.2$ and $Z_{wh}^+ = 1$

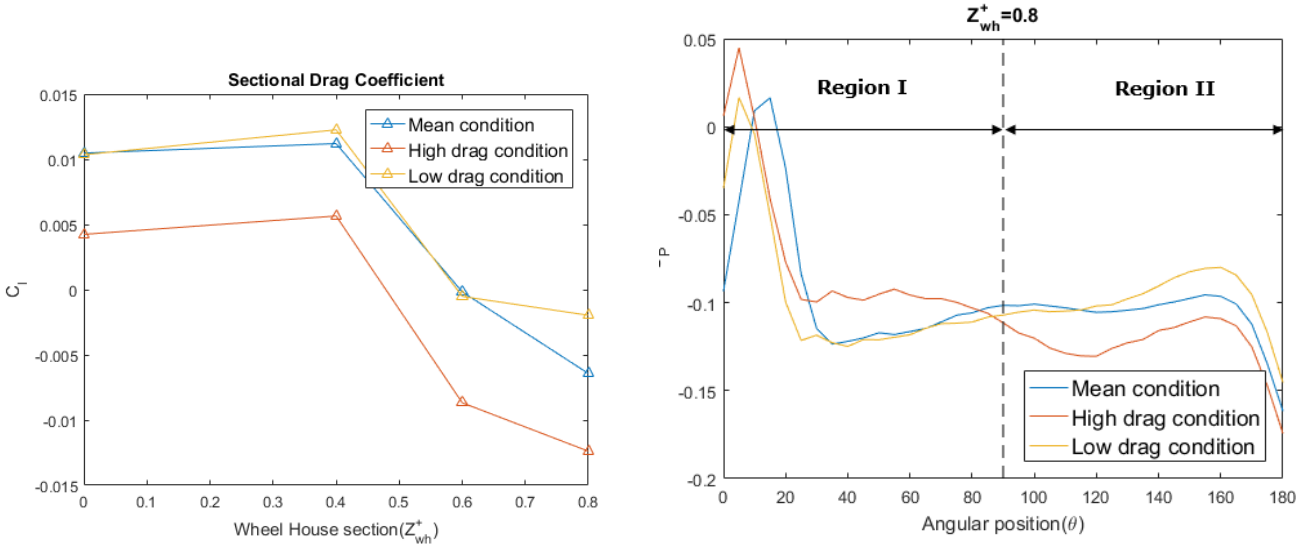


(a) (b)

Figure 7.18: The sectional force coefficients compared between the conditionally averaged data and the mean data. (b) The $C_p$ curves along the outer edge of the wheelhouse is shown for the data mentioned before. The increase in pressure in the leading section (0°-30°) and a lower pressure in the trailing section (150°- 180°) is observed in the "high" drag condition. Note that "high" and "low" drag conditions represented here are with respect to the drag coefficient of the wheel.

### Interpretation of the conditionally averaged results

The following observations pertaining to the comparison of conditionally averaged data are consistent with the observations of the pressure distribution for the Case 2 geometry :

- Higher pressures on the leading surface (Region I) and lower pressures on the trailing surface (Region II) of the wheelhouse is found to be responsible for the decrease in drag coefficient of the wheelhouse (and hence the body).
- Lower pressures in the wake of the wheel is found to be responsible for the increase in drag of the wheel.
- An increase in drag of the wheel simultaneously results in the decrease in drag of the wheelhouse (and hence the body).

The last observation is indeed interesting since it shows a simultaneous effect of a flow structure on both the wheel and wheelhouse. A highly negative correlation coefficient of -0.8 was found when comparing the temporal drag signal of the wheel and wheelhouse (refer figure 7.19). The implication of this correlation is that an increase in drag coefficient of the wheel is always accompanied by a decrease in drag coefficient of the wheelhouse. From section 7.4 and the above listed conclusions, it can be inferred that the low pressure region behind the wheel has an opposite effect on the drag coefficient of the wheel and wheelhouse. Since the B vortex is responsible for the low pressure behind the wheel, it can thus be concluded that the B vortex is responsible for the negative correlation observed between the drag coefficient of the wheel and wheelhouse. The contour of conditionally averaged pressure comparing the high drag and low drag conditions, shown in figure 7.20, confirms the above conclusion.

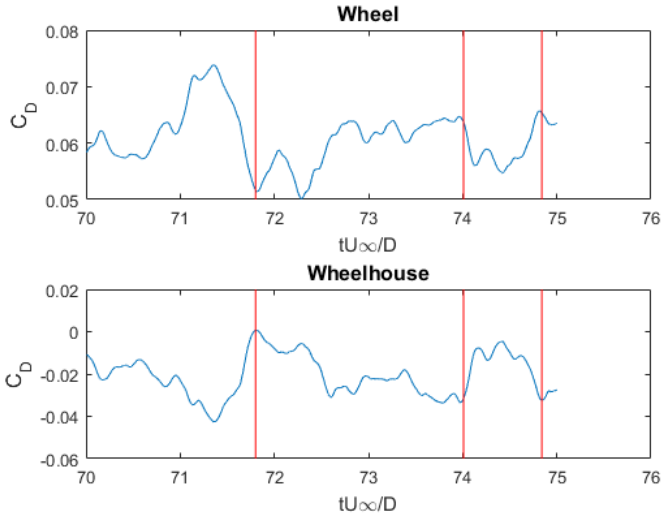


Figure 7.19: Comparison of the temporal drag signal between the wheel and wheelhouse for a short time interval. The negative correlation between the two signals can be observed from the plot i.e. a section of decreasing wheel drag corresponds to a section of increasing body drag and so on.

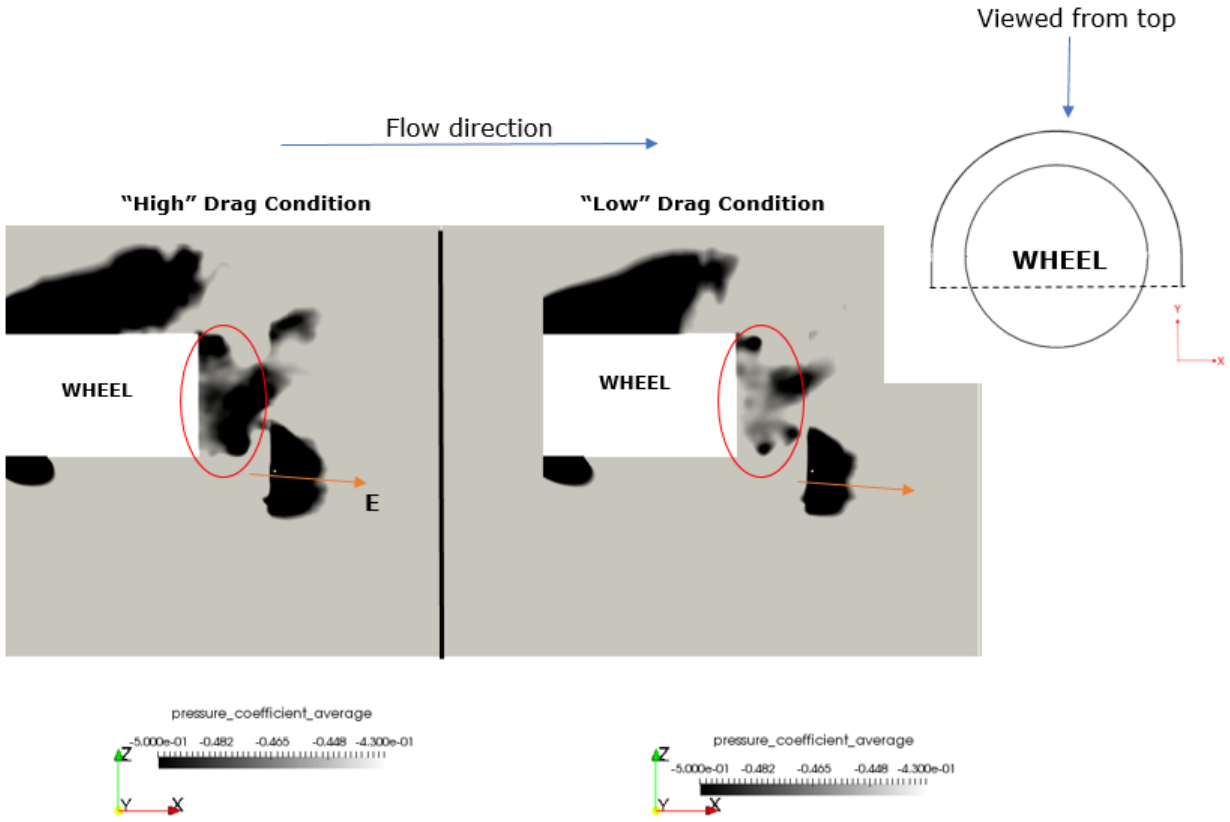


Figure 7.20: The mean pressure contours in the wake of the wheel, comparing the high and low drag conditions (top view). The location of the plane is schematically shown in the image inset. The lower pressure in the wake of the wheel, due to the stronger B vortex, increases the drag coefficient for the wheel with respect to the mean condition (i.e. "high" drag condition), while at the same time, reduces the drag coefficient of the wheelhouse.

## 7.6 Alternate Wheelhouse Geometry

Based on the conclusions of the force analysis performed between the Case 1 and Case 2 geometry presented in section 7.4, and on the conditionally averaged data presented in section 7.5, the following statements can be made, which will be useful in deciding an alternate design for the wheelhouse geometry:

1. Higher pressures on the leading surface of the wheelhouse contributes to a decrease in drag coefficient of the wheelhouse (and hence the body).

2. An increase in pressure behind the wheel leads to a reduction in the drag coefficient of the wheel.

In terms of the flow structures discussed in Chapter 7, the focus of the design change should be on controlling the effects of the H vortex and the B vortex. Given that Case 2 geometry resulted in a smaller H vortex (section 7.2.2), and Case 1 geometry resulted in weaker B vortex (section 7.2.4), the proposed design is a hybrid geometry combining the advantages of both Case 1 and Case 2 geometry as shown in figure 7.21.

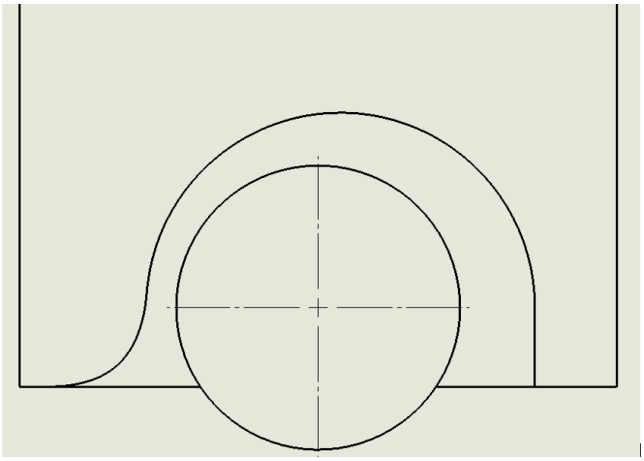

Figure 7.21: The proposed geometry for a wheelhouse than can potentially lead a reduction of the aerodynamic drag force on the vehicle. It is formed by combining the advantages of the larger wheelhouse radius of the Case 1 geometry with the smaller wheelhouse radius of the Case 2 geometry to form a hybrid-wheelhouse. (Flow is from left to right).

While a weaker B vortex would contribute to an increase in drag coefficient of the wheelhouse (the negative correlation - refer figure 7.19), an overall decrease in drag coefficient of the vehicle body is expected. The alternate wheelhouse geometry would combine the low wheel drag coefficient observed in Case 1 with the low body drag coefficient observed in Case 2. Using the values from figure 7.1, the potential reduction in drag coefficient is calculated to be around 3% with respect to the Case 1 geometry for a Reynolds number of 9 x $10^3$. Having established the qualitative similarity of the flow between the low and high Reynolds numbers (Chapter 6), it can be expected that a decrease in drag coefficient will be observed at a higher Reynolds number as well. The above proposed design is a simplified geometry based on the qualitative study performed in the present research. Such a low drag geometry could be used as a starting point in wind tunnel prototypes or parametric studies using RANS calculations to further investigate the flow field.

# Chapter 8

# Conclusions and Recommendations

The goal of the research has been to answer the questions posed in Chapter 3. A brief summary of the outcomes of the present research with respect to these objectives will be discussed in the first section of the chapter. Following this, potential areas of research that can be pursued based on the present work will be discussed.

## 8.1 Conclusions of the Research objective

The description of flow topology in the wheelhouse has been revisited in the present work. While all the previously observed flow structures were identified in the present simulation as well, differences in the behaviour of certain vortices were observed. Having validated the present simulation, both quantitatively and qualitatively, against the results from Particle Image Velocimetry (PIV), the new description of the flow field, consisting of 11 distinct vortex structures, has been presented in Chapter 2.

The first objective of this work was to investigate the dependence of the flow field on the Reynolds number. A comparison between three Reynolds numbers (9 x $10^3$, 75 x $10^3$ and 150 x $10^3$) was made by looking at the pressure distribution on the wheel/wheelhouse surface and the flow field in the wheelhouse region. The absolute values of the pressure did show variations as a function of Reynolds number, especially on the surface of wheelhouse and the edges of the wheel. But the distribution of the pressure was found to be qualitatively similar across all the three Reynolds numbers. The force obtained upon the integration of the pressure along the section of the wheel/wheelhouse giving the so-called the sectional force coefficients, were also calculated and compared, which further supported the statement of qualitative similarity. Following the comparison of the pressure quantities, the behaviour of the flow in the wheelhouse region was compared. The flow was visualized primarily using streamlines (2D and 3D) and iso-surface of low pressures. Based on the flow visualization, a strong similarity in the behaviour of the flow across all the Reynolds number was observed too. In other words, the behaviour of the flow at the lowest Reynolds number considered in the present work, was qualitatively similar to the flow observed at the highest Reynolds number.

The second research objective was focused on determining the effect of reducing the wheelhouse radius on the drag coefficient and the flow field. Because of previous conclusion, the comparison between the two geometries i.e geometries with two different wheelhouse radii, was performed at a Reynolds number of 9 x $10^3$. It was determined that a decrease in wheelhouse radius was accompanied by an increase in the wheel drag coefficient and a decrease in the body drag coefficient. For the first time, a detailed comparison of the flow field between the case of large wheelhouse radius (Case 1) and small wheelhouse radius (Case 2), with a rotating wheel, was also performed.

The third research objective is an extension of the second, in which the differences in the flow field between the Case 1 and Case 2 were correlated with the change in drag coefficient,

observed between the two cases. Four out of the 11 vortices were found to be crucial in determining the drag coefficient of the wheel and wheelhouse. It was found that a smaller wheelhouse radius correlated with lower pressures in the wake of the wheel, which resulted in an increase in drag coefficient of the wheel. Two vortices were found to influence this observation: (1) The B vortex which is formed by the flow separating from the trailing edge of the wheel and (2) the R1 vortex, which is a jetting vortex formed at the point of contact between the wheel and the ground.

At the same time, the drag coefficient of the wheelhouse was found to decrease when higher pressures on the leading surface of the wheelhouse and lower pressures on the trailing surface of the wheelhouse was observed. The increased pressure on the leading surface of the wheelhouse was found to be influenced by the behaviour of the flow separating at the leading edge of the wheelhouse (the C vortex) and the flow separation at the corner of the wheelhouse entrance (the H vortex). The lower pressure on the trailing surface of the wheelhouse can again be explained by the B vortex.

Finally, the temporal variation of the drag signal for the Case 1 geometry was analyzed. Instances where the drag coefficient of the wheel reached a local maxima or local minima were detected and conditionally averaged over. It was found that conclusions on the pressure distribution over the wheel and wheelhouse surface, derived from the comparison between the Case 1 and Case 2 geometry, are applicable to the temporal variation of drag coefficient in the Case 1 geometry as well. Moreover, a negative correlation between the variation of the drag coefficient of wheel and wheelhouse was determined, which was attributed to the presence of the B vortex.

Based on the above conclusions, an alternate design for the geometry of the wheelhouse which could potentially lead to a reduction in the aerodynamic drag of the vehicle was proposed.

## 8.2 Recommendations for future studies

The present work marks only the second instance in which LES was used to solve the problem of flow over a rotating wheel in a wheelhouse. Thus, there are still lot of areas of research that could potentially be explored of which a few are presented in this section.

The present research investigated the flow with a focus on improving the drag coefficient of the vehicle. A similar analysis on the study of the variation of the lift coefficient could be performed. With different categories of motorsport like NASCAR, World Endurance Series etc. using cars with shrouded wheels, such a study on effect of wheelhouse geometry on the lift coefficient could provide an entirely new dimension in understanding and improving the downforce of the vehicle. The present study already showed the inherent unsteadiness of the flow and the ability of a well-performed LES to capture it. Hence performing a study with a sole focus on the lift coefficient, using LES, would provide better insights into the flow dynamics.

A general overview of the behaviour of the flow was given in the present work, based on which four distinct structures were found to be significant in affecting the variation of the drag coefficient (Section 7.3). It would thus make sense to perform a study on the same flow, focusing on the above determined vortex structures to quantitatively determine the effect of these vortices on the drag coefficient. The results can be used to further refine or completely redefine the alternate design presented in section 7.6. The alternate design was based on an educated guess and further alterations to the design of the wheelhouse geometry can be obtained by performing a parametric study based on the wheelhouse geometry using the computationally cheap RANS calculations.

It is worth noting that the present work was performed on a simplified geometry with various assumptions (refer section 4.1). To extend the results from such a study to the real world scenario, independent studies focusing on both the quantitative and the qualitative aspects of the flow to find the significance of the assumptions listed in the present work could be done. For example, independent studies modelling the wheel with an accurate profile, including the cross flow through the wheel hub, to name a few, can be performed to find the respective effects on the flow field. The results can thus provide insights into the validity of the assumptions presented in this work.

# Bibliography


[1] Wolf-Heinrich Hucho. *Aerodynamics of road vehicles: from fluid mechanics to vehicle engineering*. SAE, 1998.

[2] Tamas Regert and Tamas Lajos. Description of flow field in the wheelhouses of cars. *International Journal of Heat and Fluid Flow*, 28(4):616–629, 2007.

[3] Xin Zhang, Willem Toet, and Jonathan Zerihan. Ground effect aerodynamics of race cars. *Applied Mechanics Reviews*, 59(1):33–49, 2006.

[4] Joseph Katz. Aerodynamics of race cars. *Annu. Rev. Fluid Mech.*, 38:27–63, 2006.

[5] S Krajnovič, Sasan Sarmast, and Branislav Basara. Numerical investigation of the flow around a simplified wheel in a wheelhouse. *Journal of Fluids Engineering*, 133(11):111001, 2011.

[6] Roger L Simpson. Junction flows. *Annual Review of Fluid Mechanics*, 33(1):415–443, 2001.

[7] Fackrell J.E and J.K. Harvey. The flow field and pressure distribution of an isolated road wheel. In *Adv. Road Vehicle Aerodyn.,155-164*.

[8] John Fabijanic. An experimental investigation of wheel-well flows. Report 0148-7191, SAE Technical Paper, 1996.

[9] Antonello Cogotti. Aerodynamic characteristics of car wheels. *Int. J. Vehicle design-impact aerodynamics on vehicle design, 1983,*, pages 173–196, 1983.

[10] Lee Axon. The aerodynamic characteristics of automobile wheels-cfd prediction and wind tunnel experiment. 1999. `http://dspace.lib.cranfield.ac.uk/handle/1826/3296`.

[11] Attila Schwarczkopf, Tamás Régert, and Tamás Lajos. Investigation of simple possibilities for reduction of drag due to the wheels of road vehicles. In *Proc. of 4th European Automotive Simulation Conference*, 2009.

[12] Satya P Mavuri and Simon Watkins. The influence of wheelhousing shape on vehicle aerodynamic performance. *International Journal of Vehicle Design*, 57(2-3):275–291, 2011.

[13] Alexander Wäschle. The influence of rotating wheels on vehicle aerodynamics - numerical and experimental investigations. In *SAE Technical Paper*. SAE International, 04 2007.

[14] David Söderblom, Per Elofsson, Linus Hjelm, and Lennart Lofdahl. Experimental and numerical investigation of wheel housing aerodynamics on heavy trucks. *SAE International Journal of Commercial Vehicles*, 5(2012-01-0106):29–41, 2012.

[15] Jinhee Jeong and Fazle Hussain. On the identification of a vortex. *Journal of fluid mechanics*, 285:69–94, 1995.

[16] Julian CR Hunt, Alan A Wray, and Parviz Moin. Eddies, streams, and convergence zones in turbulent flows. 1988.

[17] Yves Dubief and Franck Delcayre. On coherent-vortex identification in turbulence. *Journal of turbulence*, 1(1):011–011, 2000.

[18] Adrian F Skea, Peter Ronald Bullen, and Jun Qiao. Cfd simulations and experimental measurements of the flow over a rotating wheel in a wheel arch. Technical report, SAE Technical Paper, 2000.

[19] Alistair J Saddington, RD Knowles, and K Knowles. Laser doppler anemometry measurements in the near-wake of an isolated formula one wheel. *Experiments in fluids*, 42(5):671–681, 2007.

[20] Martinus Anthoon Van den Berg. *Aerodynamic interaction of an inverted wing with a rotating wheel*. Thesis, 2007. http://eprints.soton.ac.uk/id/eprint/49927.

[21] Emin Issakhanian, Chris J Elkins, Kin Pong Lo, and John K Eaton. An experimental study of the flow around a formula one racing car tire. *Journal of Fluids Engineering*, 132(7):071103, 2010.

[22] András Gulyás, Ágnes Bodor, Tamas Regert, and Imre M Jánosi. Piv measurement of the flow past a generic car body with wheels at les applicable reynolds number. *International Journal of Heat and Fluid Flow*, 43:220–232, 2013.

[23] James McManus and Xin Zhang. A computational study of the flow around an isolated wheel in contact with the ground. *Journal of Fluids Engineering*, 128(3):520, 2006.

[24] John Axerio-Cilies, Emin Issakhanian, Juan Jimenez, and Gianluca Iaccarino. An aerodynamic investigation of an isolated stationary formula 1 wheel assembly. *Journal of Fluids Engineering*, 134(2):021101, 2012.

[25] Emma Croner, Hervé Bézard, Christophe Sicot, and Guillaume Mothay. Aerodynamic characterization of the wake of an isolated rolling wheel. *International Journal of Heat and Fluid Flow*, 43:233–243, 2013.

[26] Sergio Pirozzoli, Paolo Orlandi, and Matteo Bernardini. The fluid dynamics of rolling wheels at low reynolds number. *Journal of Fluid Mechanics*, 706:496–533, 2012.

[27] Sammy Diasinos, Tracie J. Barber, and Graham Doig. The effects of simplifications on isolated wheel aerodynamics. *Journal of Wind Engineering and Industrial Aerodynamics*, 146:90–101, 2015.

[28] Sai Krishna Ramani. *Experimental Investigation on Wheelhouse flow field using PIV*. Thesis, 2017. http://repository.tudelft.nl/ (Ongoing).

[29] S.B. Pope. *Turbulent Flows*. Cambridge University Press, 2000.

[30] Boersma Bendiks.J Westerweel Jerry Niewstadt, Frans T.M. *Turbulence: An introduction theory and applications of turbulent flows*. Springer, 2016.

[31] P. Sagaut. *Large Eddy Simulation for Incompressible Flows: An Introduction*. Springer, 2006.

[32] Fluent 6.3 users' guide. https://www.sharcnet.ca/Software/Fluent6/html/ug/main_pre.htm.

[33] F. Nicoud and F. Ducros. Subgrid-scale stress modelling based on the square of the velocity gradient tensor. *Flow, Turbulence and Combustion*, 62(3):183–200, 1999.

[34] David Karman. *Examination of high Reynolds number flow around a spinning cylinder with different turbulence models*. Thesis, 2016. https://repository.tudelft.nl/islandora/object/uuid:9ea7f2f9-0737-4d85-b564-078c2139b422.

# Appendix A

# Turbulence Modelling

This section is devoted to give a brief explanation about Turbulence modelling and the role they play in solution to the Navier-Stokes (NS) equations. The various levels of approximation commonly used to solve the NS equations on a numerical grid will be briefly dealt with in this chapter. The content in this chapter is based on the books by Pope[29], Nieuwstadt et al [30], Sagaut[31] and also the FLUENT manual[32].

## A.1 Introduction

The present problem comes under the category of in-compressible flows and hence the basic equation of motion governing this flow is given by the Navier-Stokes equation which includes the continuity equation,

$$\frac{\partial u_i}{\partial x_i} = 0 \tag{A.1}$$

and the three momentum equations (one for each component)

$$\frac{\partial u_i}{\partial t} + u_j \frac{\partial u_i}{\partial x_j} = -\frac{1}{\rho}\frac{\partial p}{\partial x_i} + \nu \frac{\mathrm{d}^2 u_i}{\mathrm{d}x_j^2} \tag{A.2}$$

In Computational Fluid Dynamics, the above equations are numerically solved to obtain the solution to a flow problem. The existence of the solution to the Navier Stokes equation is still an open millennium problem in mathematics and the main reason for the absence of an analytic solution is attributed to the non-linear term present in the momentum equation. The physical meaning of this non-linear term is the dynamic coupling that exists between the different scales (refer figure A.1) which means that these scales cannot be isolated and solved independently. The options left with are to solve the dynamics of all the scales present in the flow, or to introduce approximations to the NS equation that will model these interactions.

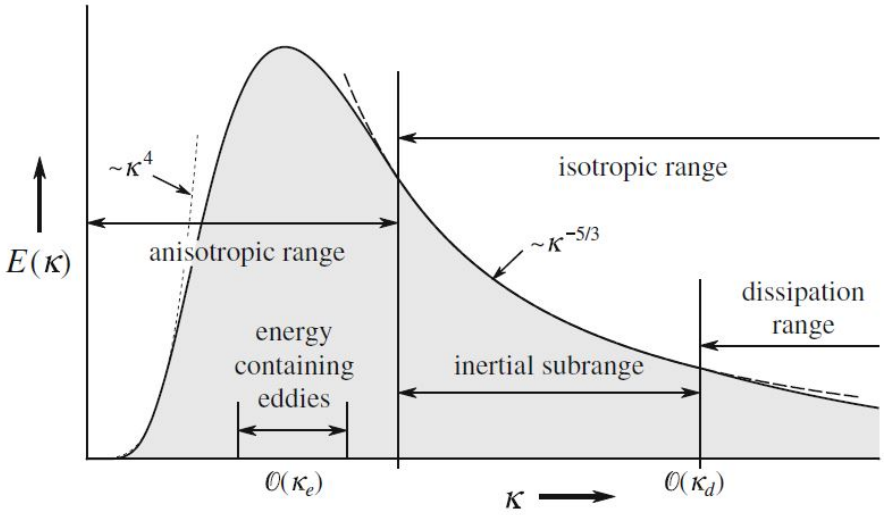


Figure A.1: The spatial energy spectrum showing the energy cascade process across the scales present in the flow. Image has been taken from [30].

## A.2 Direct Numerical Simulation

As we have already seen, CFD uses numerical techniques to solve the NS equations. To capture the entire spectrum of the flow field, the discretisation in space and time ($\Delta$x and $\Delta$t) must be smaller than the smallest scales in the flow. To determine the smallest scales in the flow, we use the kolmogorov scales for length and time. From [30], we find that the ratio between the largest and smallest length scales can be written as

$$\frac{L}{\eta} = O(Re_L^{3/4}) \tag{A.3}$$

$$\frac{T}{\tau} = O(Re_L^{1/2}) \tag{A.4}$$

where $L$ and T represent the length and time scales of the most energetic eddies and $\eta$ and $\tau$ represent the komogorov length and time scales respectively. To estimate the number of grid points needed to perform a DNS on the flow over a wheel, consider the highest Reynolds number used in the present work

$$Re_D = \frac{UD}{\nu} = 1.5\text{x}10^5 \tag{A.5}$$

where Reynolds number is based on the wheel diameter (D) and a free stream velocity (U) of 30 m/s. To estimate kolmogorv scales as shown in equations A.3 and A.4, the turbulent Reynolds number needs to be calculated. Using $U_L$ = U/10 and $L$ = D/2, which is a rough estimate of the most energetic scales in the flow, the turbulent Reynolds number can be calcuated to be:

$$Re_L = \frac{U_L L}{\nu} = 7500 \tag{A.6}$$

Equation A.3 is a measure of the resolution needed in each direction of the domain, which scales with $Re_L^{3/4}$ which means for a three dimensional domain, the required spatial resolution scales with $Re_L^{9/4}$. And while A.4 shows that ratio of characteristic time scales vary

as O($Re_L^{1/2}$), the necessity to use Courant number[1] criterion leads to a linear dependence of time step with mesh size. So for a volume $L^3$, to calculate the evolution of solution until the characteristic time of large scales, the NS equations needs to be solved O($Re^3$) times. To give an indication, studies on channel flow have been performed on a mesh of 4096 x 4096 x 4096 using DNS (as mentioned in [30]). The present computational domain is more complicated than an empty channel, with the presence of a rotating bluff body and thus it can be expected that the number of grid points estimated from the equations A.3 and A.4 is less than the actual requirement.

Thus, while DNS is the most accurate method for solving NS equations, the computational requirements it demands for a high Reynolds number means that there is a need to look for alternative methods of modelling the dynamics of all scales and this is where turbulence modelling comes into picture.

## A.3 Levels of Approximation

- The most common method of approximating the turbulent scales involves averaging the NS equations. In this method, termed Reynolds Averaged Navier Stokes (RANS), the solution **u** is split into its mean ⟨u⟩and fluctuating part $u^{'}$.

$$u(x,t) = \langle u(x,t) \rangle + u^{'}(x,t) \tag{A.7}$$

  The above statistical operation when applied to the NS equations introduces the Reynolds stress terms $\overline{u_i u_j}$ which are unknowns and require a new expression to solve the problem. This *closure problem* is solved by using Boussinesq closure hypothesis. Detailed explanations regarding RANS equation formulations can be found in [29] [30].

  The statistical nature of the RANS equations implies that a fine description of all the scales is not obtained. This method, however, is widely used in industries where the mean flow features and the overall behaviour of the flow under consideration is given importance rather than the fundamental physics governing the flow.

- While the method described above is statistically steady, the unsteadiness of the flow can also be incorporated in the Reynolds' averaging to form the Unsteady RANS, which is also called Very Large Eddy Simulation (VLES). Here the velocity field is decomposed into its time average, the conditional average and the fluctuating part.

$$u(x,t) = \langle u(x) \rangle + \langle u(x,t) \rangle_c + u^{'}(x,t) \tag{A.8}$$

  The conditional average is interpreted as the contribution of coherent modes to the solution, and when a low frequency mode exists that drives the solution, the conditional averaging is basically a phase average over these low frequency peaks. Thus, the solution described by the mathematical model is the sum of the averages $u(x)+\langle u(x,t) \rangle_c$ while the random or fluctuating part $u^{'}(x,t)$ is represented by a turbulence model. URANS in which only the largest eddies are resolved, can be seen as an intermediate step towards the development of Large Eddy Simulation.

- Finally we come to Large Eddy Simulations, where the NS equation is passed through a spatial filter. This filter determines the scales that will be resolved mathematically and the scales whose dynamics need to be modelled. The mathematically resolved scales are termed *Resolved Scales* while the modelled scales are termed *subgrid scales or residual*

[1] Courant number is a stability criterion relating the mesh size with time step. refer section A.6

*scales*. The numerical solution $u_n$ is thus represented as the resolved part and the subgrid part

$$u_n(x,t) = u_{resolved} + u_{subgrid} \tag{A.9}$$

Now, the actual solution $u_a$ and the numerical solution will not be exactly equal due to the approximations including various errors like discretisation error and resolution error. Thus, for an ideal LES,

$$|u_a - u_n| \longrightarrow 0 \tag{A.10}$$

There are two major ways of ensuring that the equation A.10 is satisfied. *Explicit LES* is one approach where the subgrid contributions are modelled as an external forcing term and form separate sets of equations similar to closure problem. The Smagorinsky and WALE model, which will be discussed in the next section, are examples of this category. The other approach is the *implicit LES*, which does not use an external governing equation like the Smagorinsky model. Going back to the errors mentioned before, the main contributors are the numerical errors , which arise due to the numerical scheme used and the resolution errors which arise from the fact that certain scales are selectively filtered out of the equation. In the implicit approach, the numerical scheme is chosen so that it counters the error due to scale approximation, and thus satisfying equation A.10

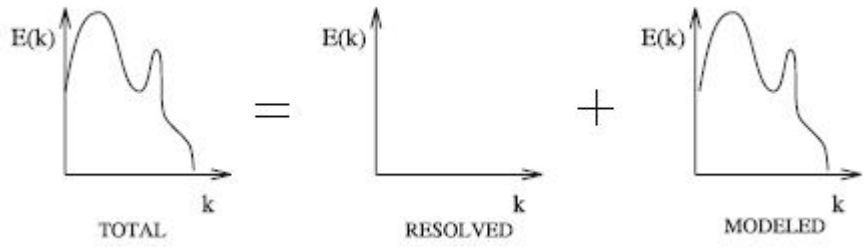


(a) RANS

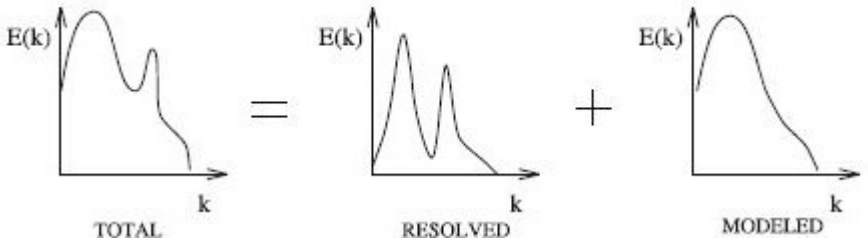


(b) URANS

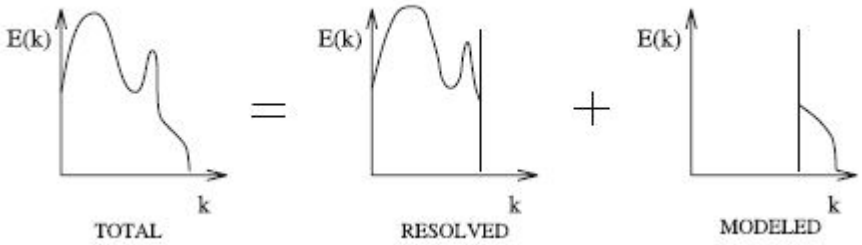


(c) LES

Figure A.2: Different levels of approximation. Each of the spectrum plot gives a description of how the total energy is modelled using numerical methods. It can be seen that (a) the total turbulent kinetic energy is modelled using a turbulence closure model in RANS , (b) Only the dominant frequency modes are resolved while the rest of the scales are modelled in URANS (c) the majority of energy is resolved in LES with the smallest scales modelled using a subgrid model. Image taken from [31]

## A.4 The Smagorinsky Model

The Smagorinsky model is a linear viscosity model based on balance of energy production in large scales and the energy dissipation in the smallest scales. The derivation, as explained in Pope[29], is as follows. Firstly, the constitutive relation is used to relate the residual stress ($\tau$) with the resolved strain rate.

$$\tau = -2\nu\bar{S_{ij}} \tag{A.11}$$

where, $\nu$ is the residual eddy viscosity or, as called in FLUENT, the sub-grid viscosity. Using the mixing-length hypothesis, the eddy viscosity is modelled as:

$$\nu = {l_s}^2|\bar{S_{ij}}| \tag{A.12}$$

$$= (C_s\Delta)^2|\bar{S_{ij}}| \tag{A.13}$$

where $l_s$ is the Smagorinsky length, $C_s$ is the Smagorinsky constant and $\Delta$ is the sub-grid filter length. The value of Smagorinsky constant is calculated by assuming the filter is in the inertial sub-range and equating the production of energy to the dissipation of energy. The value derived by Lilly for homogenous isotropic turbulence was 0.17 but when implementing

the model using FLUENT, the manual [32] reports better agreement of results using a value of 0.1. Moreover in FLUENT, the mixing length is calculated as the min($kd, C_s\Delta$) where, k is the kolmogorov constant,d is the wall distance, $C_s$ is the Smagorinsky constant and $\Delta$ is the subgrid filter length.

While the implementation of the Smagorinsky model is simple, the strong inter dependence of Smagorinsky constant and the filter length reduces the confidence of using this method. The Smagorisnky model predicts a non zero value of turbulent viscosity as soon as there is a velocity gradient, such as near a wall, where ideally all the fluctuations are dampened out giving $\nu_t = 0$. This problem was overcome by using of exponential damping functions but this again had problems. The damping function was an *ad hoc* estimation suitable only for simple geometries. So alternate models have been proposed such as the WALE model

## A.5 WALE model

Nicoud and Ducros [33] proposed the WALE model due to the limitations of the Smagorinsky model as specified above. Looking back at equation (A.10), we see that the velocity, in the mixing length hypothesis, is scaled with the local strain rate tensor. The implied meaning here is that the parameter responsible for energy transfer from large to subgrid scales is the local strain rate. This however was found to contradict DNS results which suggested that energy is concentrated in streams and is dissipated by eddies and convergence zones. Based on this result, Nicoud et al observed that while local strain rate is a good estimate to model the energy dissipation, it does not account for the energy concentration which are mainly due to vorticity. Thus, the new model was proposed to take into account both the rotational rate as well as the irrotational strain rate into account. Details on the formulation of the WALE model can be found in [33].

To summarize the advantages of using this method, the conclusions, as mentioned in the original work is presented below:

- The new model based on local strain as well as rotational rate offer a better method to detect all turbulent structures relevant for the kinetic energy dissipation.
- The eddy-viscosity goes naturally to zero near the wall. Thus, a need for dynamic adjustment or wall damping is absent.

In FLUENT [32] the mixing length is calculated as the min($kd, C_w\Delta$) where, k is the kolmogorov constant,d is the wall distance, $C_w$ is the WALE constant with a value of 0.35 in FLUENT, and $\Delta$ is the subgrid filter length.

## A.6 Implementation in FLUENT

**Near Wall Treatment**

In LES, the near wall treatment can be approached in two ways:

- Near Wall Resolution (NWR) - where boundary layer is completely resolved. Such a level of refinement can lead to resolving more than 80% of turbulent energy on the whole wall region.
- Near Wall Modelling (NWM) - where a coarse mesh is used and wall functions are used to resolve the flow close inside the boundary layer.

In FLUENT, the standard wall functions use a linear relation between $u^+$ (velocity normalized by frictional velocity) and $y^+$ (normalized distance from the wall) in the viscous sublayer,

the log -law is is applied if the first cell does not fall within the viscous sublayer . In the present simulation, the near wall resolution was high enough to ensure that the $y^+$ never exceeded a value of one ( five at the highest Reynolds number) in the finest region and thus the standard wall functions were used. Detailed description of the wall functions can be found in the FLUENT manual [32].

**Courant Number**

The Courant number is a measure of the information transfer over a computational grid in a given time step. The Courant–Friedrichs–Lewy (CFL) condition defines the maximum allowable time step for the time integration scheme in a given computational grid. The Courant number can be defined as follows:

$$C = \frac{u\Delta t}{\Delta x} \tag{A.14}$$

where C is the Courant number, u is the velocity magnitude, $\Delta t$ is the numerical time step and $\Delta x$ is the size of the mesh. For explicit time integration schemes, the value of Courant number is usually close to one. Physically, the Courant number represents ratio of the distance travelled by the flow in one time step and the size of the mesh. Thus, to properly capture the dynamics of the flow, it is thus necessary that the time taken for the flow to the adjacent grid point is more than the discrete time step used in the numerical method(i.e. C$<$ 1).

# Appendix B

# Separation Point

While the point of separation of the boundary layer that has formed over a stationary wall can be defined as the point where the wall shear stress becomes zero, the same cannot be said for a boundary layer over a rotating wheel. The moving wall, eliminates the boundary layer close to the surface and hence, it has been found that the flow separates from a point, away from the surface of the wheel [7].

Consider the flow over a rotating wheel, such that the point of contact between the wheel and ground has a zero relative velocity. The no slip boundary condition, imparts a velocity to the flow in proximity, that is equal to the velocity of the wall. This results in the formation of a thin region of fluid layer, rotating along with the wheel surface. This region is termed as a Rotating Boundary Layer (RBL) [34]. The outer edge of the RBL, thus acts as the outer surface of the wheel, where the flow is found to separate.

While shear stress cannot be used as a criterion for determining the location of separation point, the flow still experiences an adverse pressure gradient which is reflected in the Cp curve along the surface of the wheel. The separation point can thus be determined from the region of adverse pressure gradient on the surface of the wheel [20]. The point along the surface where an adverse pressure gradient is followed by a region of constant pressure is the point where the flow has completely separated (figure B.1). But how can the separation point be determined if the pressure distribution along the wheel is not available?

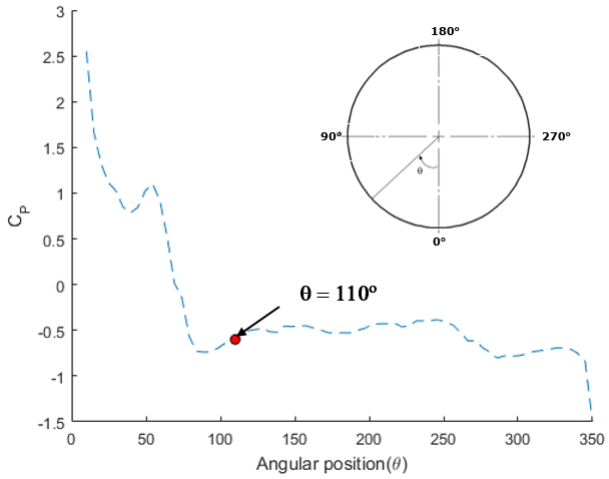


Figure B.1: The pressure distribution on the surface of the wheel along the centre line. The pressure peak at an angle of 0 °corresponds to the high pressure explained in section 2.2. The separation point is also marked in the figure based on the definition provided in this section.

The azimuthal velocity profiles along lines perpendicular to the surface of the wheel at different angular positions can also be used to identify the separation point. This is done by identifying the thickness of the RBL. The thickness of the RBL can be defined as the point of inflection of velocity along the above mentioned lines. The separation of flow results in the formation of a low pressure bubble, which imparts a radially outward force on the RBL. This leads to an increase in thickness of the RBL and thus, the separation point can be estimated by identifying the angular location where the increase an thickness of RBL is observed.

Applying the above criterion to the present simulations, the following results were observed. Figure B.2a shows the velocity profile along a line perpendicular to the surface of the wheel, at an angular position of 90°(refer figure B.1 for definition of angular notation). The horizontal axis shows the tangential velocity, normalized by the free stream velocity and the vertical axis shows the normalized wheelhouse gap: A value of zero represents the surface of the wheel and one represents the wheelhouse wall.

By determining the point of inflection of velocity along the lines perpendicular to the wheel surface, the locus of all points forming the RBL can be determined (figure B.2b). The present method of determining the separation point, using thickness of RBL, is in good agreement with the values obtained from the Cp curve (B.1). This method of determining the point of separation is found to be a novel technique not found in the literature. The main advantage this technique is its ability to detect the separation point using velocity field which is easier to obtain using, say Particle Image Velocimetry(PIV)[22] [28], than the pressure distribution on the surface of a rotating wheel.

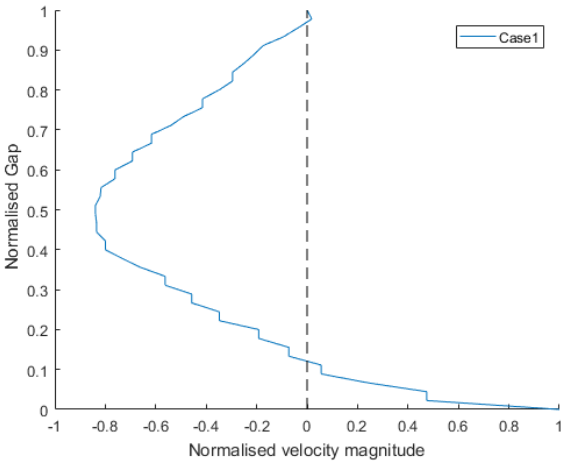


(a)

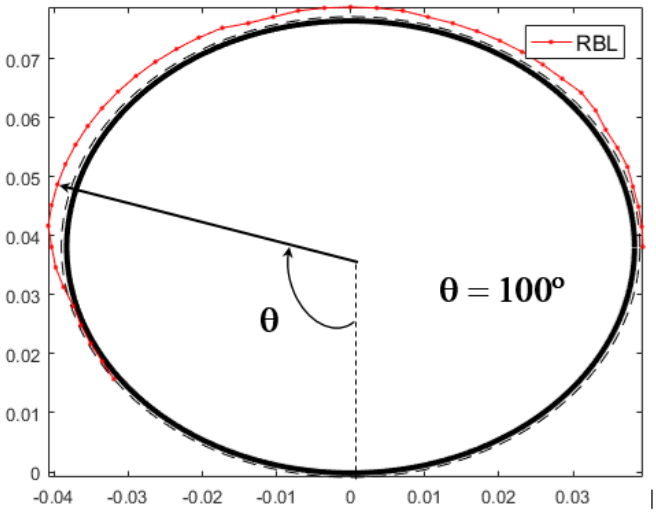


(b)

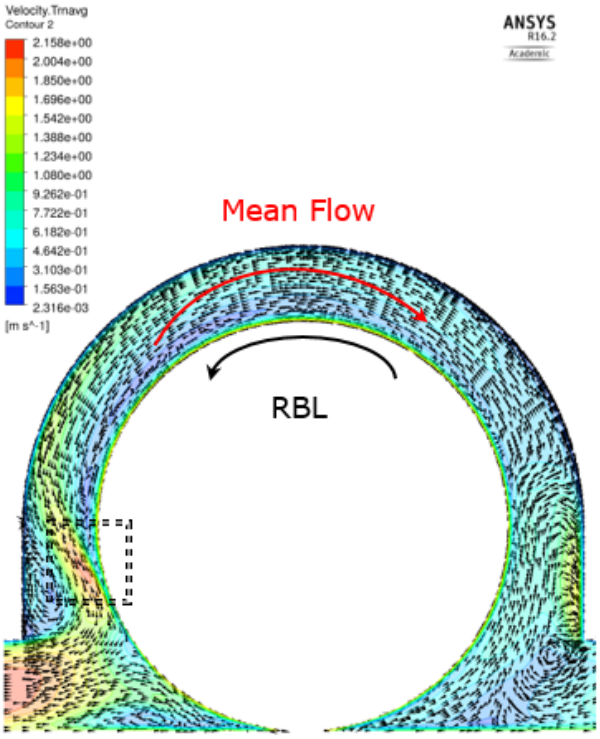


(c)

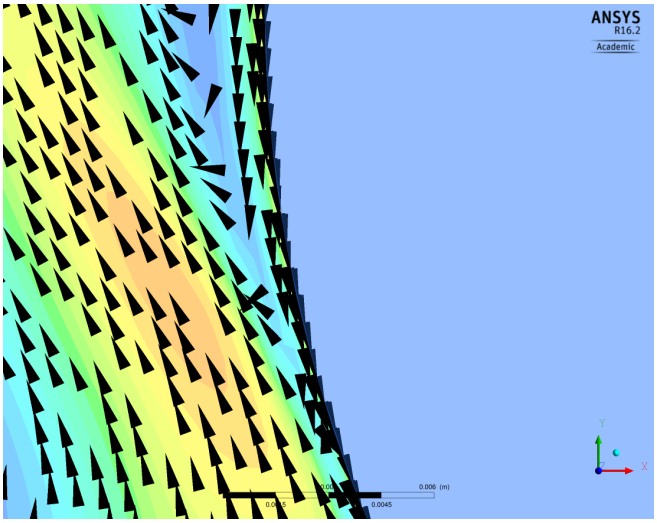


(d)

Figure B.2: (a) Azimuthal velocity as a function of the radial distance away from the wheel. The normalized quantities are shown in the figure. (b) The profile of the RBL along the surface of the wheel. The section of wheel inside the wheelhouse cavity is shown in this figure. The black dotted line is the thickness of RBL based on the value found upstream of the separation point. (c) Vector plot of the flow over the wheel in a wheelhouse at the mid-plane. (d) A close up of the region marked by square depicting the RBL near the separation point. Flow is from left to right.

# Appendix C

# Symmetry BC Validation

In the list of assumptions presented in Chapter 4, the flow field was assumed to be symmetric with respect to the x-y plane. This leads to a reduction of the numerical domain and hence the size of the numerical grid by 50 %. But since a highly unsteady solution method (LES) is used, the lack of symmetry in the instantaneous flow field may affect the mean flow field. To investigate the effect of using the symmetric boundary condition, a comparison between a full and half model of the vehicle body is presented in this chapter. The basecase model, which is the vehicle configuration with no wheel or wheelhouse is used to validate the symmetry boundary condition.

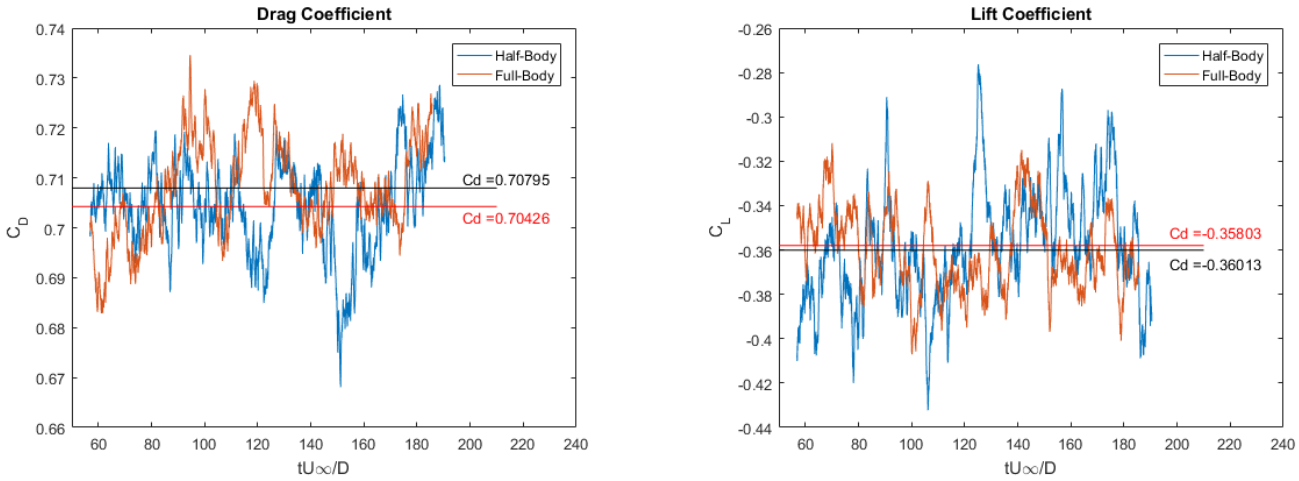


(a) (b)

Figure C.1: Comparison of drag of lift coefficients of the two models. While the symmetry plane did not affect the mean values of drag and lift, with a deviation between values of 0.5 % in both cases, the nature of force variations are indeed different. This could be due to the way vortices are shed from the rear of the body; the half model sheds two vortices at a given period due to the symmetry plane whereas the full model sheds the vortices alternatively.

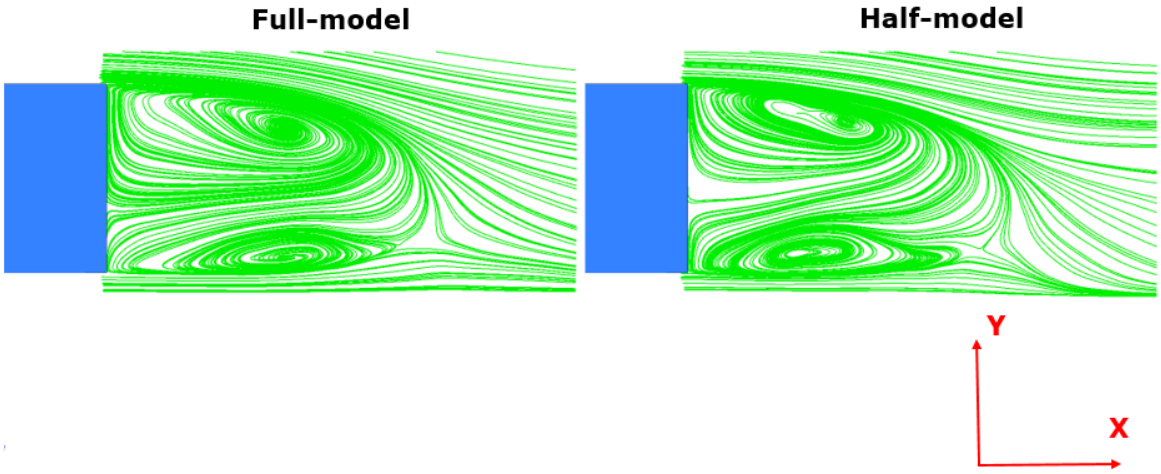


Figure C.2: Surface streamlines at a plane in the wake of the body, near the symmetry plane. The slip boundary condition on the symmetry plane resulted in some deviation of the results from the expected which is why a plane 5 mm away from the symmetry plane was chosen for comparison.

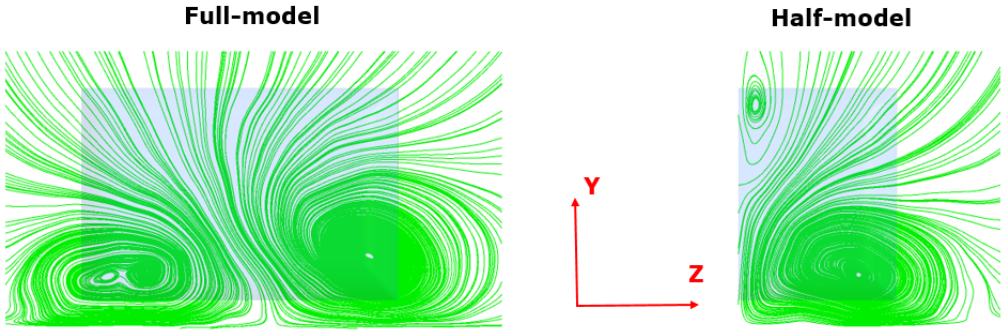


Figure C.3: The vortices visualized in the far wake of the body. The plane chosen is 3.5 H away from the rear of the body. While it is interesting to see that the vortex pair observed in full body is not completely symmetrical, the half model is found to be capable of reproducing a similar vortex structure in the same plane.

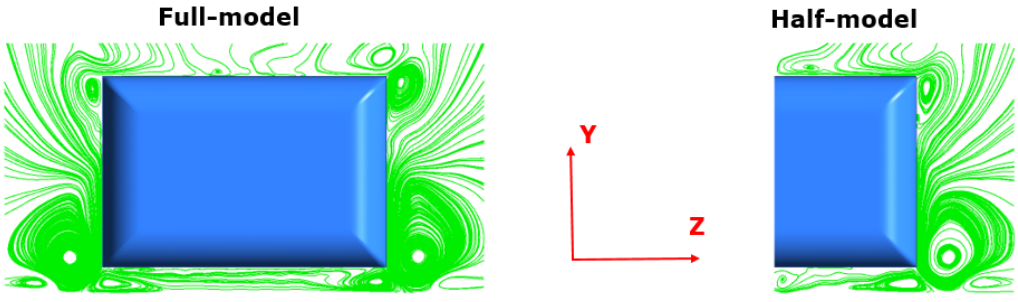


Figure C.4: The vortices visualized in the midplane of the body.The vortex cores visualized here are caused due to the recirculation effect occurring at the sharp edges of the body. Given the minimum interaction of flow between the two edges, it is natural to observe a symmetric distribution of flow in this plane.

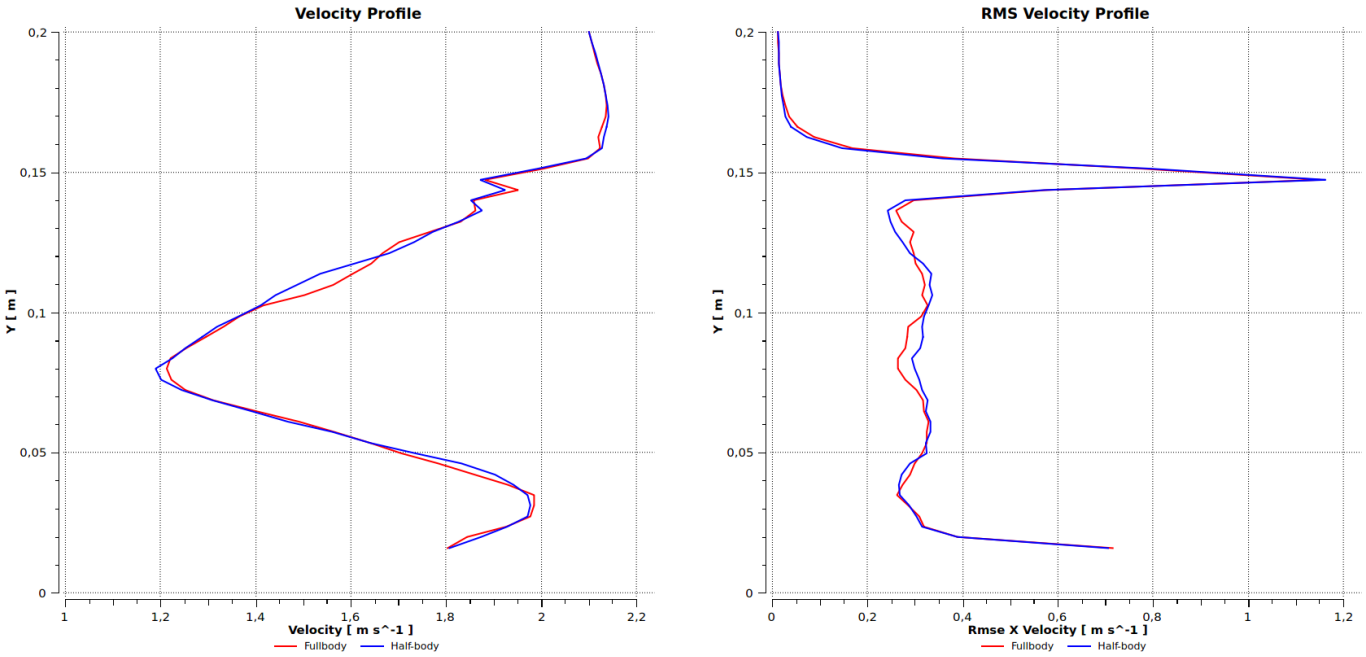


(a)




(b)

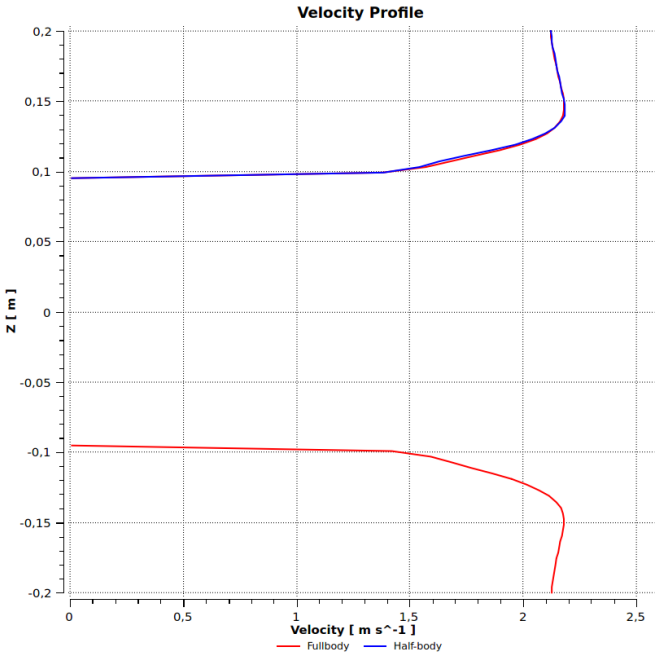


(c)

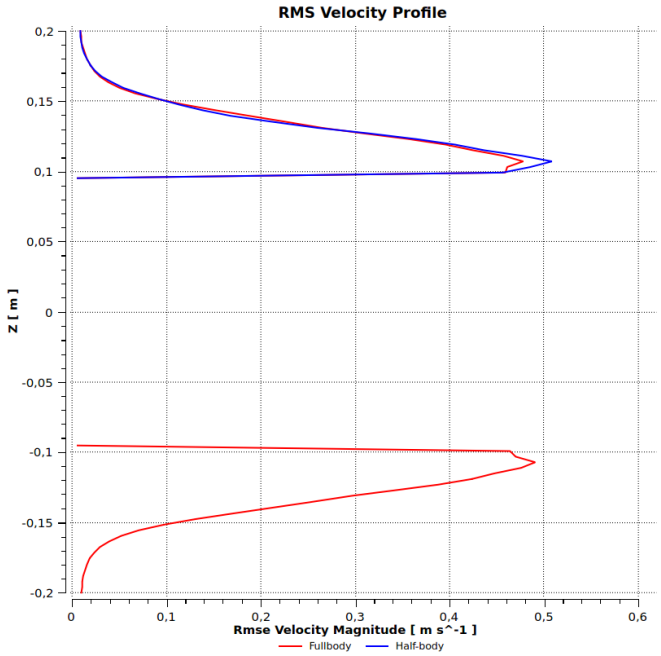


(d)

Figure C.5: Comparison of mean and rms velocity profile (a) and (b) show the respective profiles along a line parallel to the side face and in the +Y direction. (c) and (d) are plots along a line perpendicular to the side face and in the Z direction. The symmetric curves drawn from Z = -0.1 correspond to the other edge of the vehicle in full-body configuration. The lines are coincident with the mid plane of the body.

# Appendix D

# LES vs URANS

While the well-modelled Large Eddy Simulation is highly accurate, results of which were discussed in detail in the present work, the computational requirements posed by such a simulation is not feasible in an industrial environment. The present simulation, with around 11 million grid points, which was run in parallel on 28 cores required approximately 25 days of CPU time to run to completion. Thus, it makes more sense to solve the Reynolds Averaged Navier-Stokes (RANS) equation to obtain the flow field. In this chapter, a comparison between the solution from LES and Unsteady RANS (URANS) performed on the present geometry is presented. The results of URANS were obtained for Reynolds number of 9000 ($Re_{1W}$) using the realizable k-$\epsilon$ model with standard wall treatment. Second order upwind for the convective terms and second order Euler for time was used for discretization.

## D.1 Comparison of Drag and Lift Coefficients

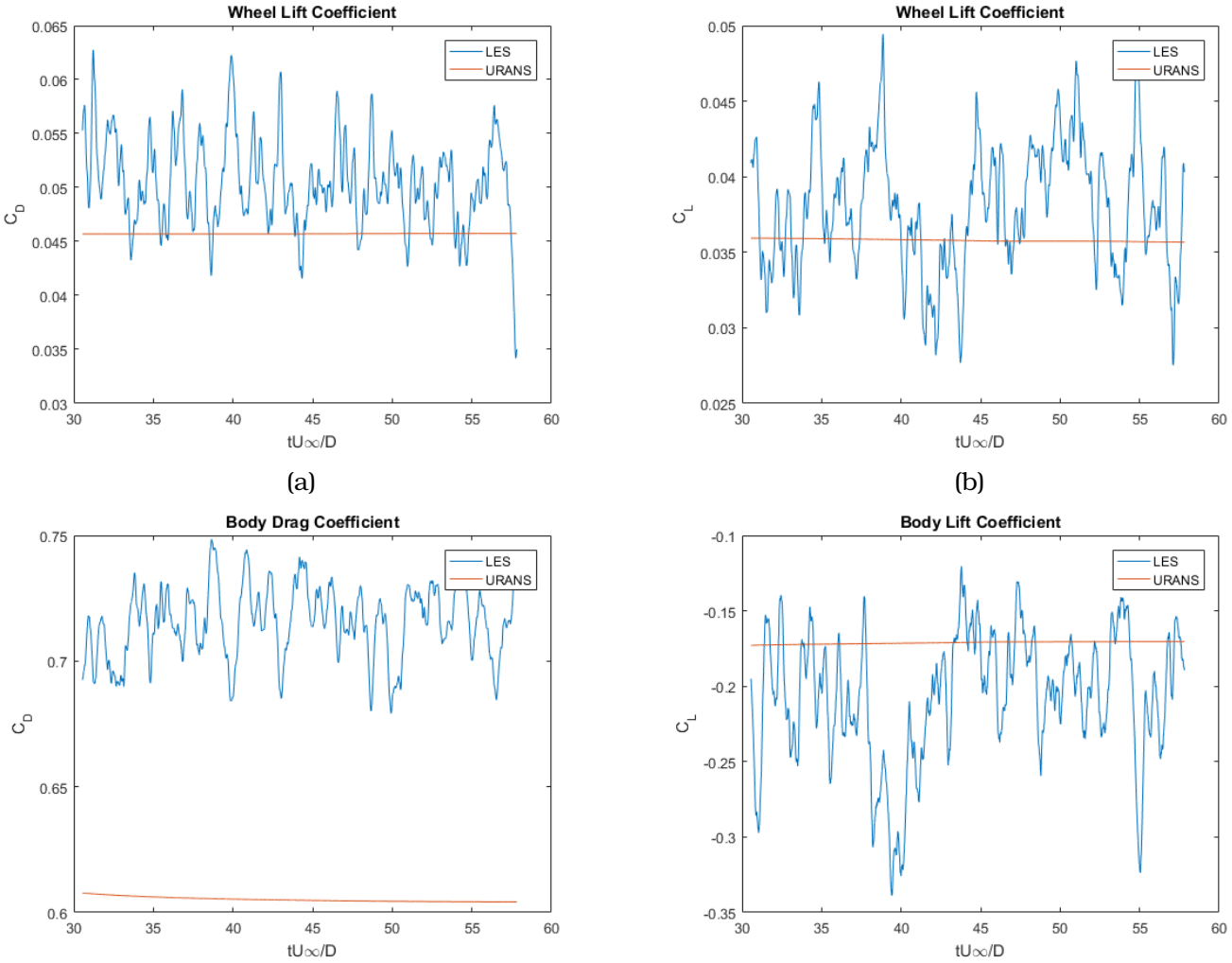


Figure D.1: Comparison of force coefficients between LES and URANS is presented. The unsteadiness of the flow and inability of URANS to capture the same is clearly shown. Recalling the results from Chapter 6, the mean lift coefficient of the wheel was found to be higher than the one estimated from the experiment. A similar increase in the lift coefficient with respect to the experiment was observed with URANS results as well.

## D.2 Comparison of Pressure Distribution

### Wheel

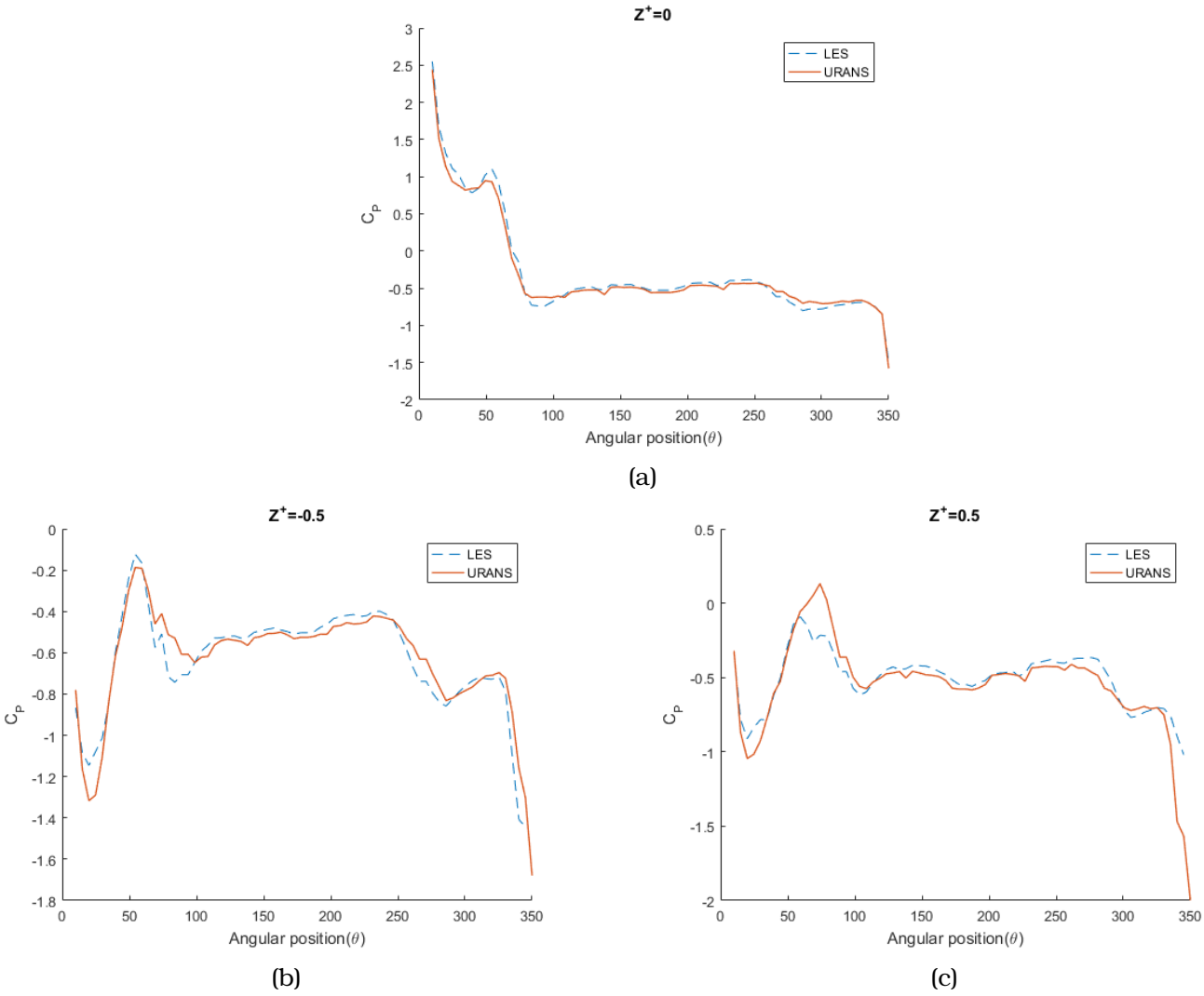


Figure D.2: Comparison of the distribution of the mean pressure on the surface of the wheel between LES and URANS.

### Wheelhouse

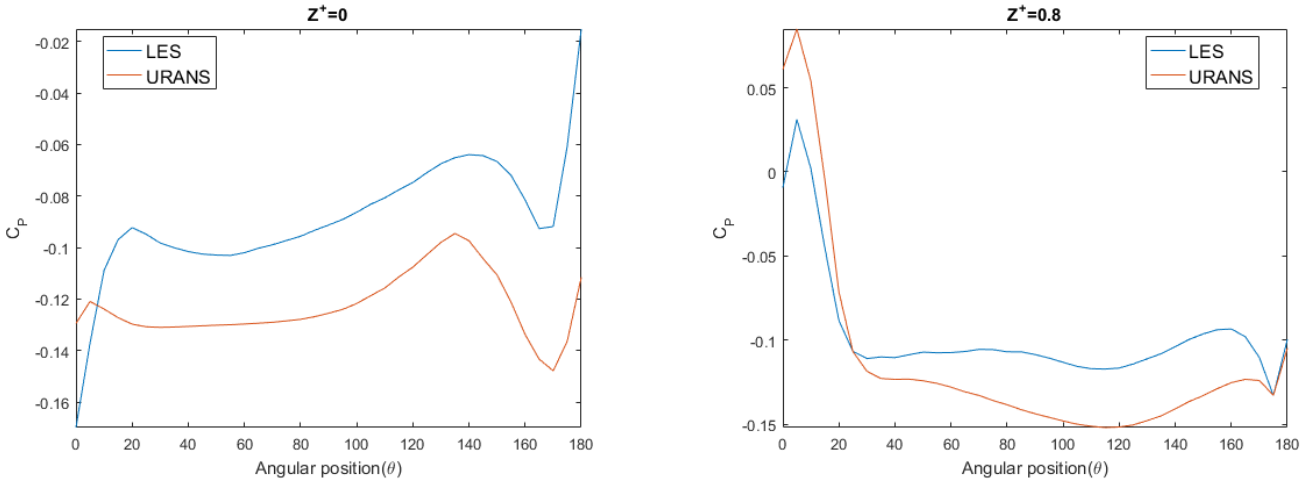


(a) (b)

Figure D.3: Comparison of the distribution of the mean pressure on the surface of the wheelhouse between LES and URANS. The difference in values between LES and URANS points to the effect of unsteadiness of the flow inside the wheelhouse cavity.

## D.3 Conclusion

A brief comparison between the solution from URANS and LES was performed in this chapter. Based on the temporal signal of drag coefficient presented in the figure D.1 , the highly level of unsteadiness of the flow, and the inability of URANS to capture the same can be visualized. The mean value of the drag coefficient obtained from the URANS simulation, is however comparable with that from the LES. A comparison of pressure distribution on the wheel and wheelhouse surface was also made. The differences in the mean pressure distribution on the surface of the wheelhouse points to the influence of unsteadiness of the flow on the wheelhouse (figure D.3). The unsteady behaviour of the flow was, however, found to be less influential on the pressure distribution over the surface of the wheel as shown in figure D.2.

# Appendix E

# DNS vs LES

The comparison of the subgrid quantities with the total resolved stress pointed to an LES that is well performed. Since the contribution from the subgrid model is low (under 20%), a Direct Numeric Simulation (DNS) was used to solve the flow problem under consideration. The lowest Reynolds number considered in this work i.e. Re = 9 x $10^3$ was used to obtain the solution on an otherwise unchanged numerical grid. A basic comparison of the integral and flow quantities is presented in this chapter.

## E.1 Comparison of Drag and Lift Coefficients

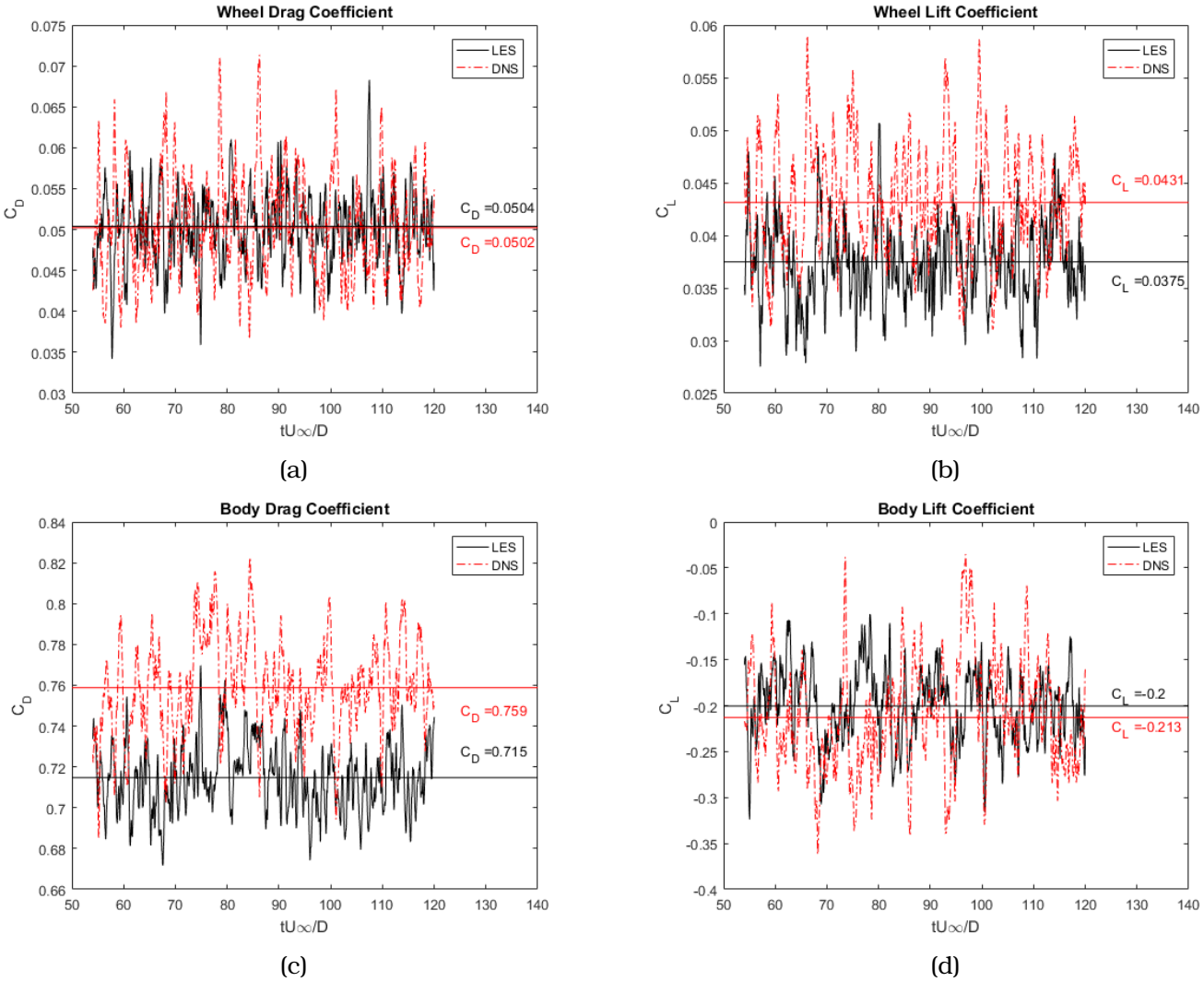


Figure E.1: Comparison of force coefficients between LES and DNS is presented . The drag coefficient of the wheel and the lift coefficient of the body shows good agreement between DNS and LES. However, the effect of the subgrid viscosity model on the lift coefficient of wheel and the drag coefficient of the body can be observed

## E.2 Comparison of Mean and RMS Velocity Profile

### E.2.1 Wheel Upstream

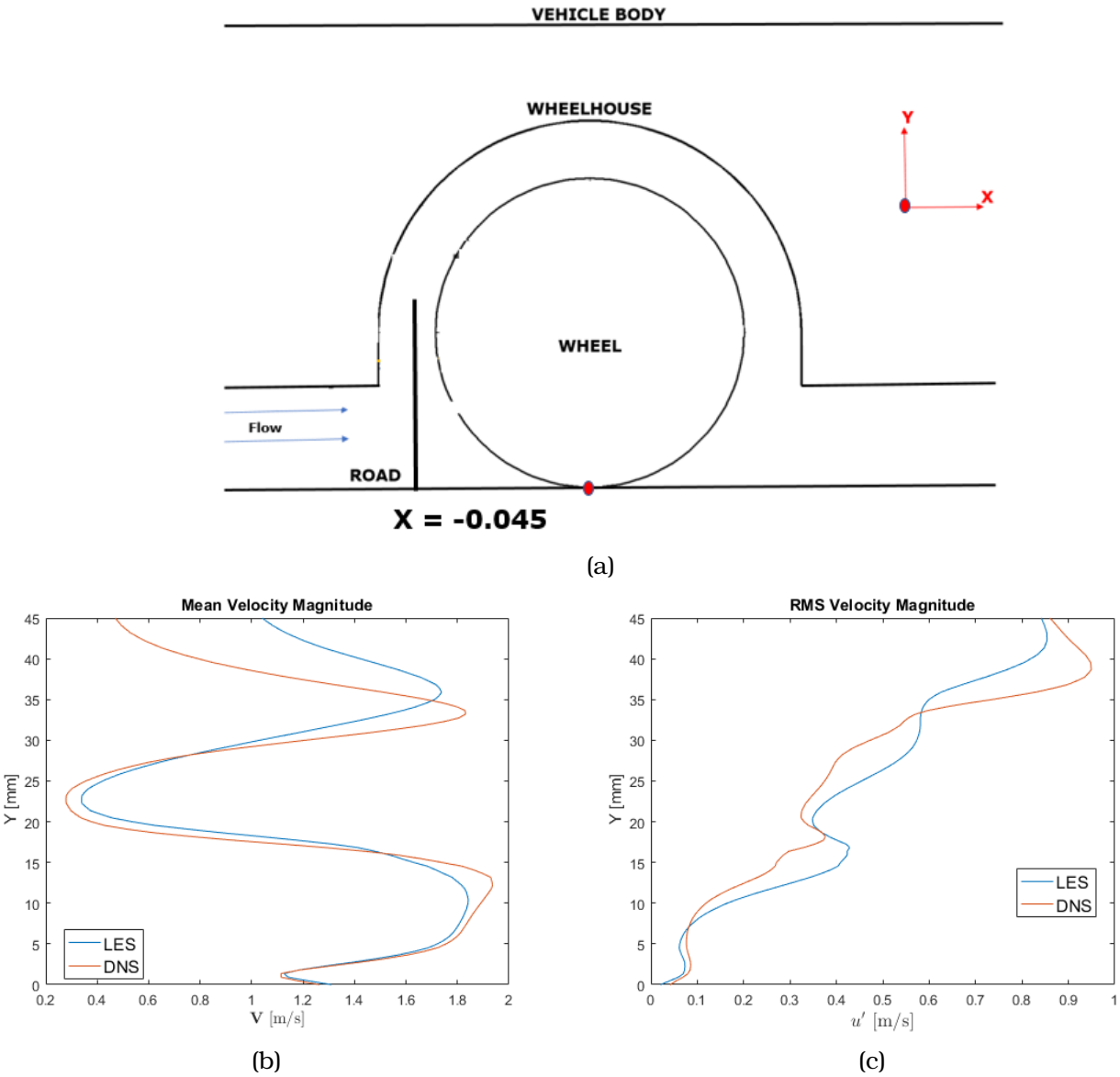


(a)

(b)

(c)

Figure E.2: Comparison of the (b) Mean and (c) Root mean squared velocity profiles along a line upstream of the wheel. The location of the line along which the quantities are plotted is schematically shown in (a). The red circle in (a) marks the location X = 0.

### E.2.2 Body Wake

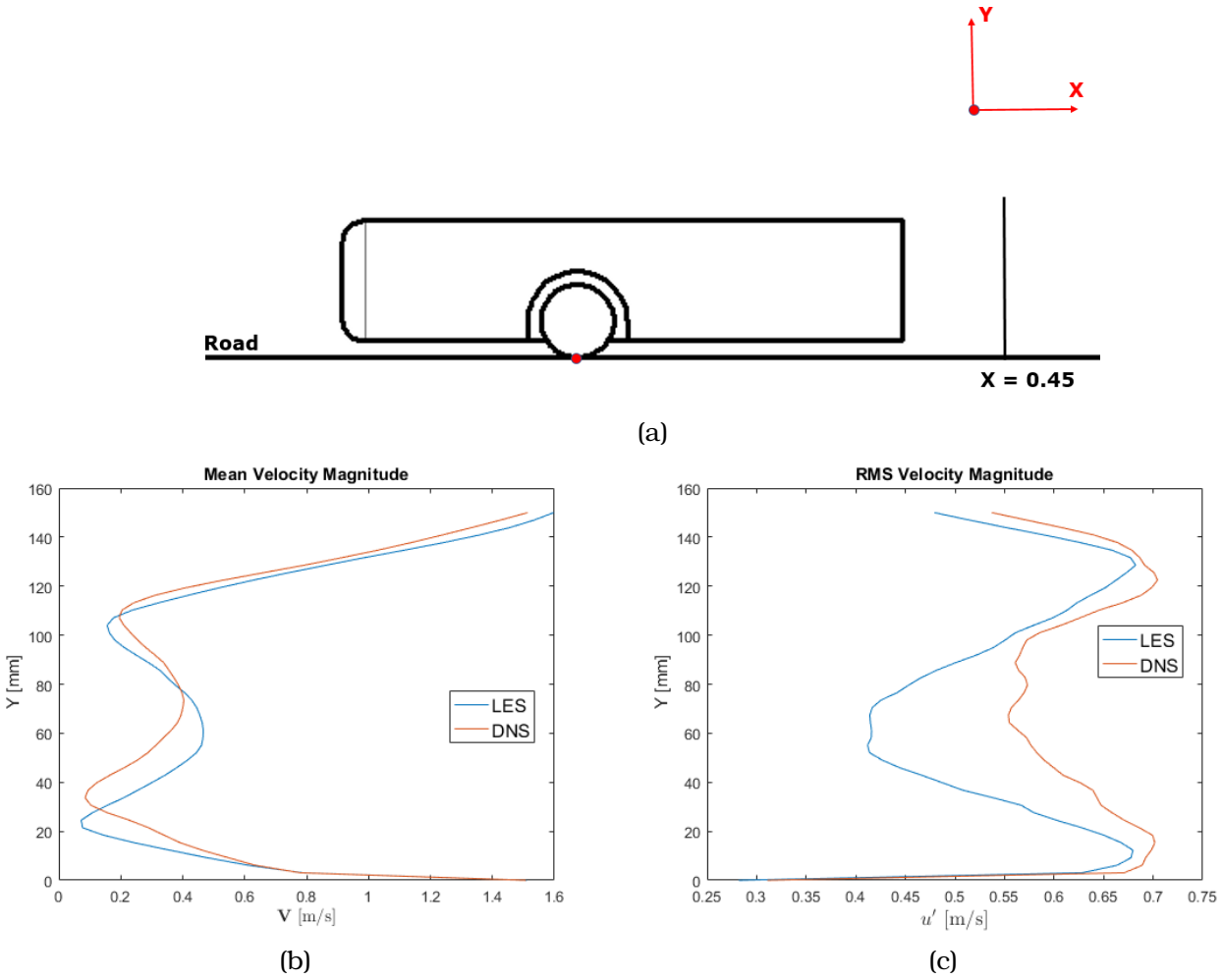


(a)

(b)

(c)

Figure E.3: Comparison of the (b) Mean and (c) Root mean squared velocity profiles along a line in the wake of the body. The location of the line along which the quantities are plotted is schematically shown in (a). The red circle in (a) marks the location X = 0. While the mean velocity profiles show a good agreement, the RMS velocity shows a considerable variation between LES and DNS. The refinement of mesh in this region is considerably lower than that found in the wheelhouse region.

## E.3 Comparison of the temporal signal

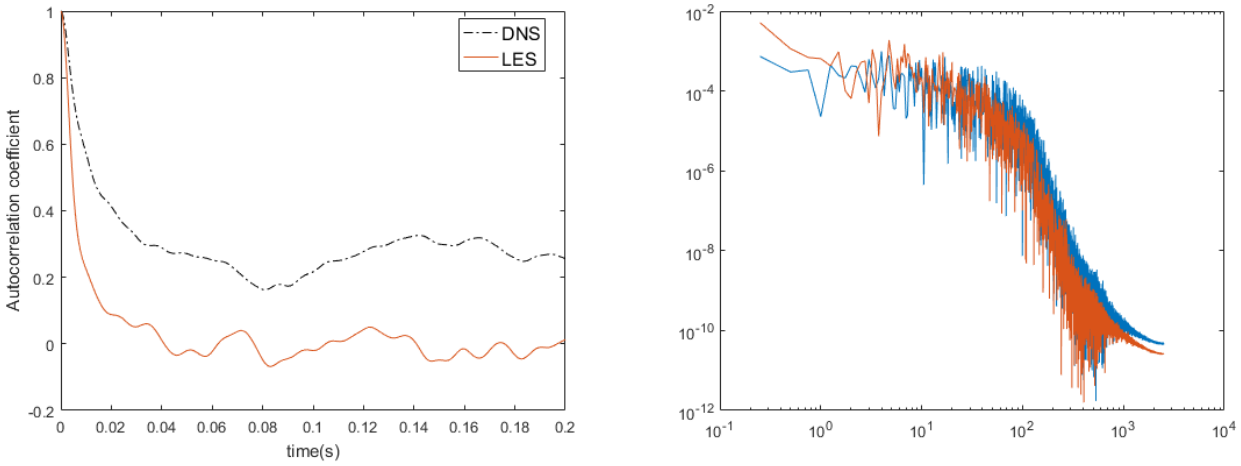


(a) (b)

Figure E.4: (a) Comparison of the integral time scale. The autocorrealtion coefficient as a function of the time lag (s) for the streamwise component of velocity is compared between DNS and LES. (b) The comparison of the spectrum of streamwise fluctuation of velocity (u') is shown.

## E.4 Conclusion

The results from the DNS are in good agreement with the results from LES in the region where the flow is finely resolved i.e. inside the wheelhouse. While the mean velocity magnitude in the wake of the body showed a good agreement, the DNS predicted a higher RMS velocity pointing to the influence of subgrid viscosity model in this region (a relatively coarse mesh) (refer figure E.2 and figure E.3). Finally, the time scale of the most energetic structures found inside the wheelhouse showed a considerable difference between DNS and LES (refer figure E.4a) while the power spectrum density of the velocity fluctuations at the same location are in good agreement (refer E.4b). Thus, while the influence of subgrid viscosity model is low, the absence of the subgrid viscosity (i.e. DNS) did lead to an observable difference in the temporal statistics of the flow field. The mean flow field, however, was found to be uninfluenced by the subgrid viscosity model.

# Appendix F

# Subgrid Viscosity model Comparison

The list of all simulations performed as part of *Run 1* was mentioned in Chapter 4. A combination of both the Smagorinsky and WALE model was used which was discussed in Chapter 6. The Smagorinsky model had to be used in the present research because of an unphysical effect that was observed when the WALE model was used. The drag and lift coefficient of the body showed a rise in value for a short duration of time. The above observation with drag coefficient is shown in figure F.1. Thus, the present chapter is focused on presenting a basic comparison of the solutions obtained using the two subgrid models. All the subsequent results shown in this chapter are for a Reynolds number of 75 x $10^3$ based on the wheel diameter.

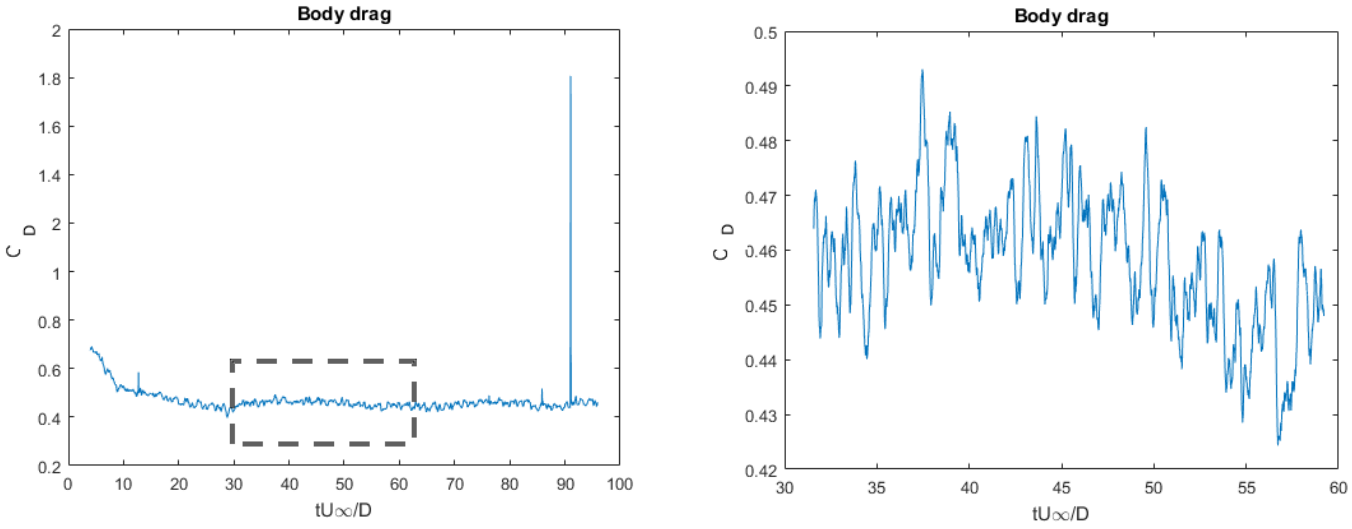


(a) (b)

Figure F.1: The effect of using WALE model on the drag coefficient of the body. It can be observed from (b) that the temporal variation of drag coefficient shows expected behaviour in the entire time domain, apart from the drastic rise in values over the short duration shown in (a).

## F.1 Comparison of Drag coefficient

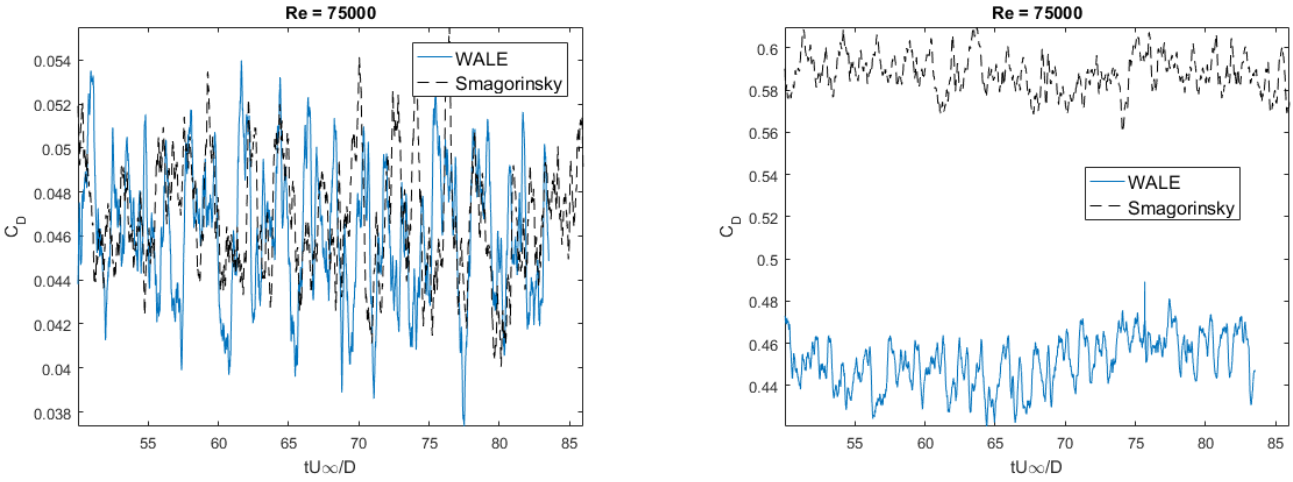


(a) (b)

Figure F.2: The comparison of temporal signal of (a) wheel and (b) body drag coefficient. While the variation of drag coefficient of the wheel shows a good agreement between the two models, the significant difference is observed between the drag coefficients of the body. This could be due to the different level of mesh refinements which was explained in chapter 4.

## F.2 Comparison of contours Mean and RMS velocity magnitude

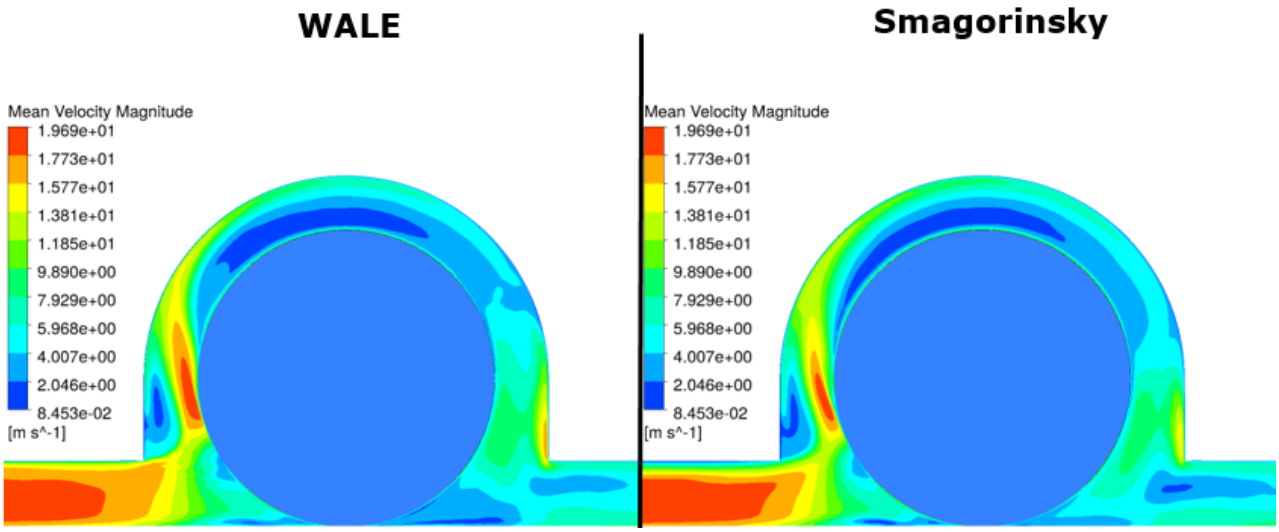


Figure F.3: The comparison of mean velocity magnitude in the wheelhouse gap between the Smagorinsky and WALE. It should be noted that Re= 75000 corresponds to a free stream velocity of 15 m/s. A good level of agreement can be observed between the two subgrid models.

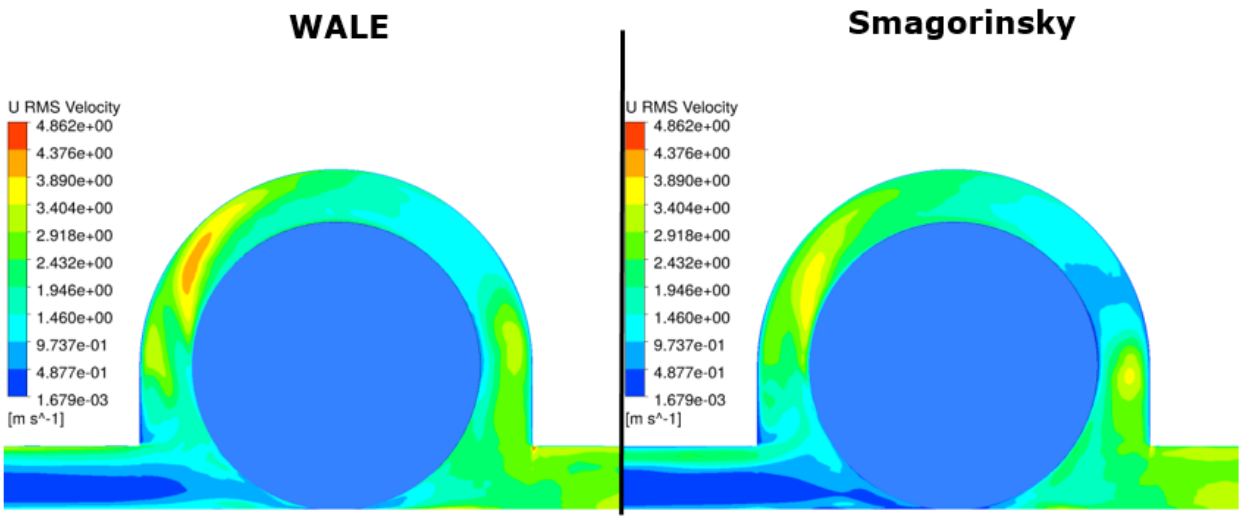


Figure F.4: The comparison of streamwise component of RMS velocity magnitude in the wheelhouse gap between the Smagorinsky and WALE. The WALE model shows a higher value of RMS velocity near the leading edge of the wheel while the same region shows a smaller value when using the more diffusive Smagorinsky model.

## F.3 Comparison of Resolved and Subgrid stress

As explained in Appendix A, the scales in the flow field can be divided into the resolved part and the sub grid, when performing an LES. If more than 80 % of the turbulent stresses are mathematically resolved, it shows that the numerical grid used for the simulation is able to resolve the large scales with high accuracy[29].

The resolved part of the turbulent shear stress ($\overline{U'V'}$) can be calculated as follows:

$$\overline{U'V'}_{resolved} = \langle u'v' \rangle \tag{F.1}$$

where u' and v' are fluctuations of velocity and $\langle\rangle$ represents average over time. The resolved stresses are obtained from FLUENT. The subgrid contribution to the turbulent shear stress can be calculated using boussinesq hypothesis as explained in Appendix A as follows:

$$\overline{U'V'}_{subgrid} = -\nu_t(\frac{du}{dy} + \frac{dv}{dx}) \tag{F.2}$$

where $\nu_t$ is the subgrid viscosity and term within the bracket represents the gradient of velocity. The transient data collected (refer section 7.5) was used to calculate the time average of the subgrid stress. Based on the above calculation, the total turbulent shear stress can be calculated, which is then compared with the resolved turbulent shear stress as shown in figure F.5 and figure F.6

## F.4 Conclusion

The aim of the present comparison was to give an insight into the influence of the subgrid model on the solution to the flow problem under consideration. A very good agreement between the Smagorinsky and WALE model could be observed, when comparing various flow quantities like the mean and RMS velocity and the turbulent shear stress (refer figure F.3, figure F.4 and figure F.5). The comparison did show a significant variation in the mean value of drag coefficient of the body as shown in figure F.2b. The present analysis did not reveal the conclusive reason for either the dependence of the drag coefficient on the subgrid model, or the unphysical behaviour of the body drag coefficient observed with the WALE model. Studying the pressure distribution on the surface of the vehicle body could provide an answer to the open questions mentioned above.

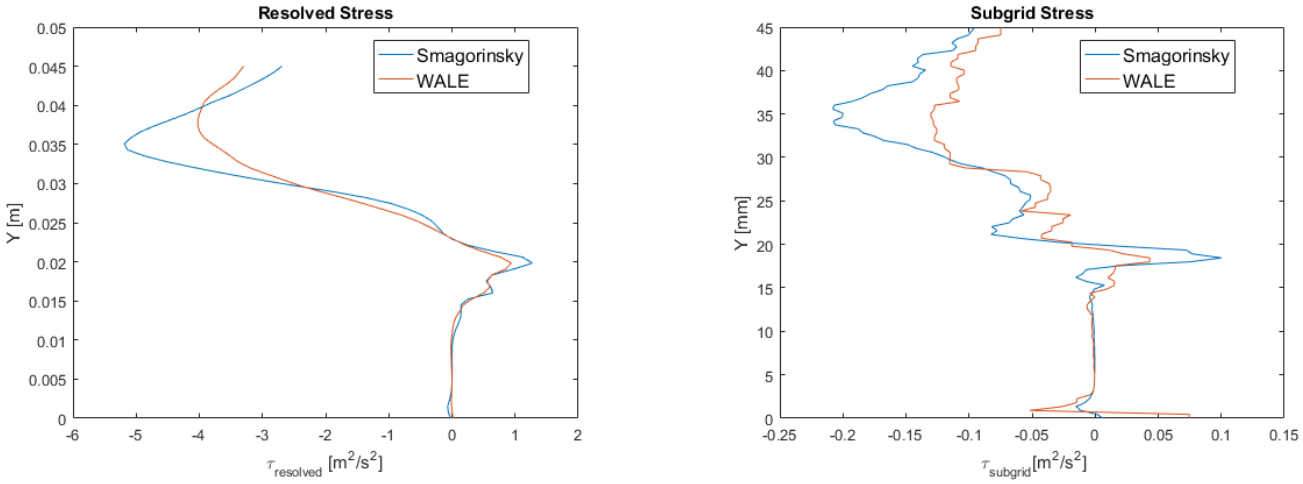


(a) (b)

Figure F.5: The comparison of the (a) Resolved and (b) subgrid stresses along a line in the fine mesh region (i.e. inside the wheelhouse) is compared. The non-zero value of the subgrid contribution near the ground (Y = 0) for the Smagorinsky model is observed.

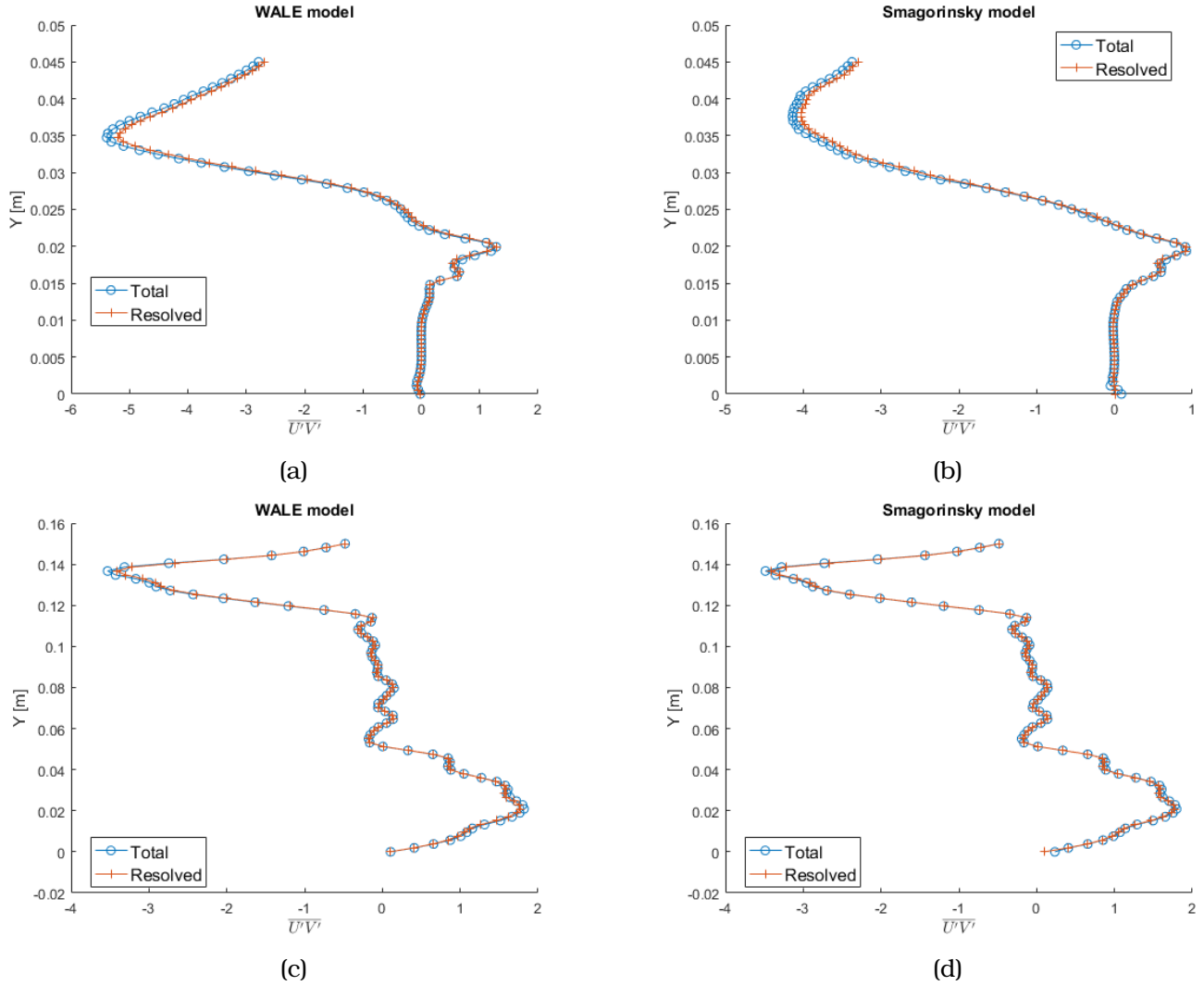


Figure F.6: The comparison of the total turbulent stress with the resolved stress for WALE model and Smagorinsky model. The plots (a) and (b) are along a line inside the wheelhouse i.e. the region with finest mesh. The plots (c) and (d) are along a line in the wake of the body. The UV stresses are considered here. It can be seen that the subgrid contribution to the total stress is very low (less than 10 %) irrespective of the subgrid model.